UNIVERSITY OF SOUTHAMPTON

FACULTY OF PHYSICAL AND APPLIED SCIENCES

SCHOOL OF PHYSICS AND ASTRONOMY

Material Parameter Extraction in Terahertz Time Domain Spectroscopy

Aaron Lester Chung

Submitted for the degree of Doctor of Philosophy

September 2012

UNIVERSITY OF SOUTHAMPTON

ABSTRACT

Faculty of Physical and Applied Sciences

School of Physics and Astronomy

Doctor of Philosophy

Material Parameter Extraction in Terahertz Time Domain Spectroscopy

by Aaron Lester Chung

In terahertz time domain spectroscopy (THz-TDS) material parameter extraction is necessary for determining the complex refractive index of materials in the THz region. The process of material parameter extraction requires the fitting of a theoretical model for the propagation the THz pulse through the material to experimentally acquired THz time domain data, where by the complex refractive index of the theoretical model is varied until it fits the experimental data. It requires close agreement between a model of the THz electric field propagation and experimental THz data for accurate extraction of the complex refractive index.

In this thesis I report on the methods of material parameter extraction with the goal of accurately determining the complex refractive index of materials within the THz region. I also investigate a series of optimisation techniques from understanding the behaviour of the extracted complex refractive index for different model assumptions and initial parameters. The inclusion of the material parameter extraction optimisation techniques allows for material parameter extraction methods which are similar to the state of the art in the field.

Material placed at the THz focus are commonly investigated using the plane wave assumption for material parameter extraction. I demonstrate an extraction method which models a converging beam, this improves the accuracy of the extracted complex refractive indices for materials placed in focused THz-time domain spectrometers. Furthermore, I have developed an elegant method to determine the angular beam profile of the focussed THz beam by using the converging beam extraction method.

Finally I report on the THz-TDS performance of photoconductive THz generation and detection from a high peak power vertical external cavity surface emitting laser (VECSEL). VECSELs are optically pumped semiconductor disk lasers (SDL) which are inherently compact, have multi-GHz repetition rates and could lead to a cost effective THz spectrometer system.

Declaration of Authorship

I, Aaron Lester Chung, declare that the thesis entitled Material Parameter Extraction in Terahertz Time Domain Spectroscopy and the work presented in it are my own. I confirm that:

- this work was done wholly or mainly while in candidature for a research degree at this University;
- where any part of this thesis has previously been submitted for a degree or any other qualification at this University or any other institution, this has been clearly stated;
- where I have quoted from the work of others, the source is always given. With the exception of such quotations, this thesis is entirely my own work;
- I have acknowledged all main sources of help;
- where the thesis is based on work done by myself jointly with others, I have made clear exactly what was done by others and what I have contributed myself;
- parts of this work have been published as listed on the following page.

Signed:

Date: 27/09/2012

Acknowledgements

I would like to acknowledge the many people who have helped and supported me during my PhD. I would like to thank my supervisor, Dr. Vasilis Apostolopoulos, for guiding me throughout my PhD. He was always there to help me during the difficult parts of my research and encouraged me to be bold and daring. I would also like to thank Professor Anne Tropper for her supervision and excellent advice. I am indebted to Dr. Geoff Daniell, who contributed enormously to the theoretical grounding of the material parameter extraction methods and construction of the extraction algorithms used throughout this thesis. I thank him for the countless discussions we had on computer programming and material parameter extraction. I would like to acknowledge Dr. Axel Zeitler for contributing THz-time domain scans which have been invaluable to the works demonstrated in this thesis.

I would also like to thank members of the VECSEL-THz group which I worked with through out the years. I would like to thank Dr. Zakaria Mihoubi, Dr. Stephen Elsmere, Dr. Adrian Quarterman and in particular Dr. Keith Wilcox for the many insightful discussions on laser physics. I would also like to thank Mark Barnes, Duncan McBryde, Dr. Hani Kbashi, Robin Head, Olly Morris and Andrew Turnbull.

I would also like to acknowledge the mechanical and electronics workshop, and support staff who over the years helped maintain and update the labs. In particular I would like to thank Damon Grimsey, Gareth Savage and Gary Taylor who helped contribute to many components of the THz time domain spectrometers. I am also grateful to all the researchers of the Quantum Light and Matter group for sharing their knowledge and research in the various seminars and colloquiums.

Finally, I would like to thank my friends and family for the love, help and support during my PhD.

Contents

List of Figures

List of Tables

Chapter 1

Introduction

The motivation for the work present in this thesis is to develop and understand the method of material parameter extraction in order to accurately determine the complex refractive index of materials in the THz range. This requires material parameter extraction methods and analysis techniques which improve the fitting of the theoretical model for the propagation of the THz pulse through the material to the experimental data recorded by the THz spectrometer. The foundations of such material parameter extraction methods and analysis techniques are discussed throughout the thesis.

This introduction continues with a brief description of THz spectroscopy and application. The THz time domain spectrometer is essential in my analysis acquiring the time dependent electric field of the THz pulse that is required for the characterisation of materials using material parameter extraction, therefore I also describe the principles of THz-TDS and the common techniques for THz pulse generation and detection that are used by THz time domain spectrometers. I also mention other THz generation and detection methods and discuss material parameter extraction. Finally, I outline the contents of the thesis.

1.1 Terahertz spectroscopy and applications

Terahertz (THz) radiation is situated between the far infrared and microwave band in the electromagnetic spectrum as shown in fig. 1.1. The THz region includes wavelengths that range from 1 mm to 30 μm or correspondingly has frequencies of 300 GHz to 10 THz and energies of

1 meV to 40 meV. There exist many vibrational and rotational modes of molecules within the THz region which has enabled the detection and study of various chemical species, this alone has made the THz region relevant to a wide breadth of scientific fields such as submillimeter astronomy [1, 2], atmospheric studies [3, 4] and molecular spectroscopy [5, 6].

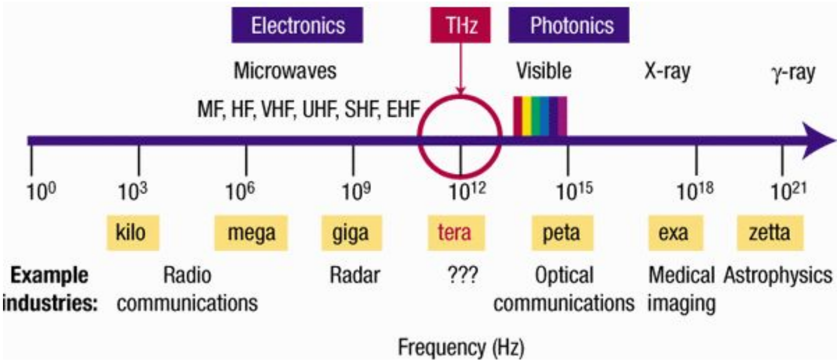

Figure 1.1: The electromagnetic spectrum showing the position of the THz region that sits between the microwave and far infrared regions. Taken from [7].

The THz region is the meeting point where the operational frequencies of electronic and photonic devices converge, this has made it technologically difficult to access the entire THz region. Electronic devices are limited by carrier mobility and lifetimes that operate at THz frequencies, whereas for photonic devices, the bandgap or transition energies are generally too large or too close to thermal energies at room temperature to operate in the THz region. These technological constraints have lead to a so-called THz gap which signified a lack of sources and detectors, however due to the continual development of THz technologies [8, 9, 10] it is becoming increasingly smaller.

A significant milestone for broadband THz generation and detection was the demonstration [11] of freely propagating THz pulses using photoconductive antenna (PCA) by D. H. Auston et. al. in 1984 which led to the method of THz time domain spectroscopy (THz-TDS) [12]. THz-TDS is a coherent and synchronous method for generating and detecting broadband THz radiation, akin to a pump-probe setup. The combination of spectroscopic and time resolved phase information of broadband THz radiation can be measured in THz-TDS, this has resulted in a major application which is the characterisation of materials [7]. In THz-TDS PCA have been used to generate and detect bandwidths up to 20 THz [13], using non-linear methods of

THz generation PCA have been demonstrated with the capability of detecting THz bandwidths from 0.1 to 100 THz [14].

The fundamental time scales of carrier motions within the photoconductive semiconductors used for PCA enable the generation of THz radiation, likewise THz radiation is also sensitive to conducting carriers that move on similar time scales. The flexibility offered by the optical pump-THz probe configuration known as Time-Resolved Terahertz Spectroscopy (TRTS) [15, 16, 17] has made THz-TDS particularly useful for measuring carrier dynamics within semiconductors because of the sensitivity of THz radiation to the motion of carriers on fundamental time scales and the combination of spectroscopic and time resolved phase information that can be measured. As a consequence THz-TDS has been used to measure carrier dynamics within bulk semiconductors [18, 19], ultrathin layers of semiconductors [20] quantum wells [21], quantum dots [22] and nanoparticles [23]. THz-TDS has also been used to investigate protein folding in biological systems [24], electron spin response of anti-ferromagnetic metals [25] and inter-molecular vibrations [6].

THz imaging [26] was also realised due to freely propagating THz pulses, this has enabled time of flight THz imaging which can internally resolve material interfaces [27]. THz pulsed imaging has the capacity for simultaneous THz imaging and spectroscopy which is useful for chemical recognition [28]. THz pulsed imaging also has applications in the pharmaceutical industry for analysing the quality of tablet coatings [29] and in medicine to study skin cancer and skin disorders [30]. THz radiation is non-ionising, opaque to metals, penetrates clothing and hence there are many security applications [31] such as the detection of concealed weapons, explosives and drugs. There are now many small commercial THz companies such as MenloSystems, Gigaoptics, Zomega, Picometrix and TeraView which specialise in THz technologies and applications.

1.2 Principles of THz-TDS operation

In THz-TDS a THz time domain spectrometer generates broadband THz radiation in the form of a THz pulse, it also measures the time dependent electric field of the THz pulse. If the THz pulse is incident on a material then that material will modify the time dependent electric field of the THz pulse according to its optical constants in the THz region. Material parameter extraction is a method of determining the optical constants of the material from its modification to the THz electric field recorded by a THz time domain spectrometer.

In a THz time domain spectrometer an ultrafast laser is used in a pump-probe scheme to generate and detect the THz radiation, a typical THz-TDS setup is shown in fig. 1.2. The pulse train is split into a pump and probe beam, the pump beam is incident on the emitter and the probe beam gates the receiver. This synchronises the receiver with the emitter, ensuring that the receiver is only active when there is THz radiation being generated which improves the signal to noise ratio (SNR) of the system by reducing the detected noise. Furthermore, the detected noise is also reduced by using a lock-in amplifier to measure the signal from the receiver. The emitter is modulated with the lock-in frequency of the lock-in amplifier, it can be modulated either electronically using a signal generator or by optically chopping the pump beam.

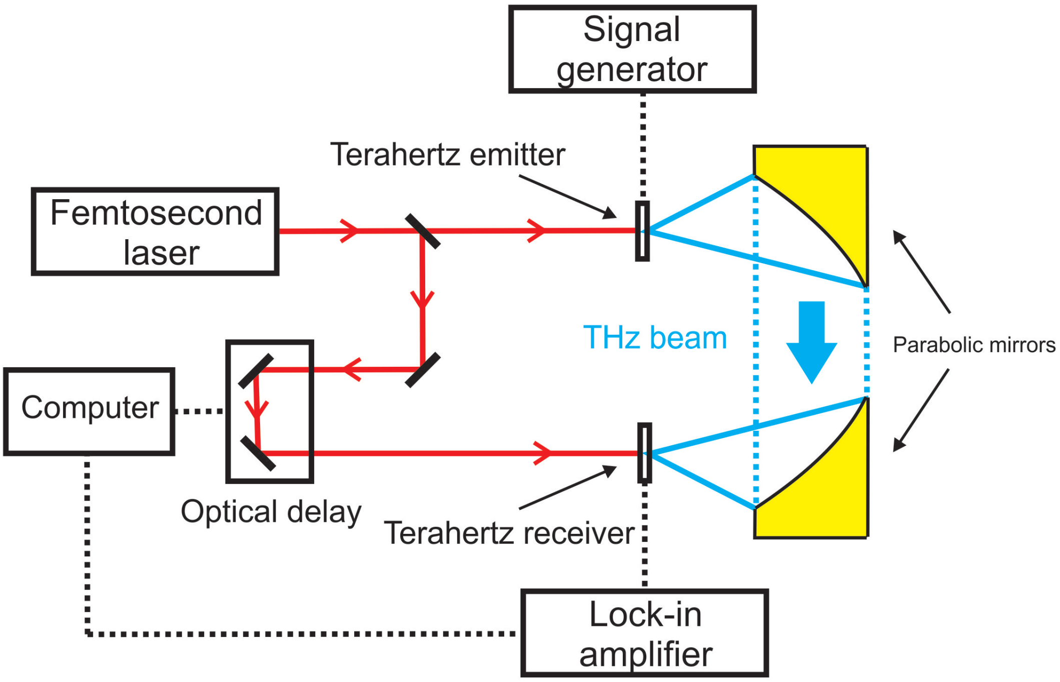

Figure 1.2: Schematic for a typical two parabolic mirror THz time domain spectrometer. The THz emitter is electronically modulated at the lock-in frequency by the signal generator to improve signal detection.

A parabolic mirror is used to collimate the divergent THz beam that radiates from the emitter and then a second parabolic mirror is used to focus the collimated THz beam onto the receiver. Different focusing optics and configurations can be used to guide the THz beam depending on the intended application, for example a focus could be required for THz imaging or small sample areas. The radiated THz pulse from the emitter is a single cycle pulse that lasts for a few picoseconds whereas the receiver is only active for a few hundred femtoseconds, only a fraction of the time dependent THz electric can be measured by the receiver at any one time. The delay stage is used to gate the receiver at different time intervals which allows for the time dependent THz electric field to be measured. Samples placed within the THz beam will experience a spectrum of probing energies in the THz region and will modify the detected THz pulse which can be used to study the sample.

1.2.1 THz pulse generation

The common methods of THz generation and detection in THz-TDS use photoconductive or non-linear effects. Photoconductive THz generation is achieved by transient currents within PCA, photoconductive detection is essentially the same mechanism but in reverse. Non-linear THz generation is achieved using optical rectification [32, 33] of a non-linear crystal and for detection a non-linear crystal can be used to electro-optically sample the THz pulse via the Pockel's effect. The photoconductive and non-linear methods can be used in conjunction with each other and the combinations which produce the greatest THz bandwidths has received much attention within the field of THz-TDS [34, 35, 36].

Photoconductive

A schematic of a PCA is shown in fig. 1.3, it consists of a photoconductive semiconductor with a gold structure deposited on the top to form the antenna. The semiconductor is excited by an optical pulse which is focused between the antenna gap to produce carriers. The carriers are accelerated by an electric field which is provided by a bias voltage. The production and acceleration of the carriers within the semiconductor creates a rising photocurrent which decays after some time due to the recombination of the electrons with the holes. The rise and fall of the photocurrent produces a time varying electric dipole which radiates a THz pulse.

The peak emission wavelength of the THz pulse is hundreds of microns, this is many times greater than the gap between the antenna electrodes which are typically just a few microns. When

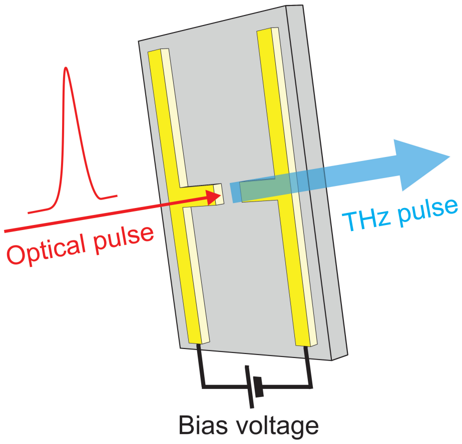

Figure 1.3: Schematic of a photoconductive dipole antenna. A bias is placed across the electrodes to accelerate the carriers to generate a photocurrent.

the emission wavelength is many times greater than the effective antenna length the Hertzian dipole approximation can be used. The electric field radiated from a Hertzian dipole antenna [37] at time t is,

$$E(r,t) = \frac{l_e}{4\pi\epsilon_0 c^2 r}\frac{\partial J(t)}{\partial t}\sin\theta \propto \frac{\partial J(t)}{\partial t}, \tag{1.1}$$

where $J(t)$ is the photocurrent in the dipole, l_e is the effective length of the dipole, ϵ_0 is the dielectric constant of a vacuum, c is the speed of light and θ is the angle from the direction of the dipole. The electric field of the THz pulse is proportional to the rate of change of the photocurrent.

The evolution of the THz electric field with respect to the optical pulse and photocurrent are shown in fig. 1.4. The profile of the THz pulse is generated within the rise of the photocurrent and the photocurrent is generated during the envelope of the optical pulse. The decay of the photocurrent is responsible for the negative dip after the THz pulse. The photocurrent density $j(t)$ is dependent on the optical intensity of the laser pulse $I(t)$ convoluted with the carrier density $n(t)$, charge q and velocity $\nu(t)$ which is described [38] by,

$$j(t) \propto I(t) \otimes [n(t)q\nu(t)]. \tag{1.2}$$

The duration of the THz pulse is limited by the ability of the semiconductor to respond to

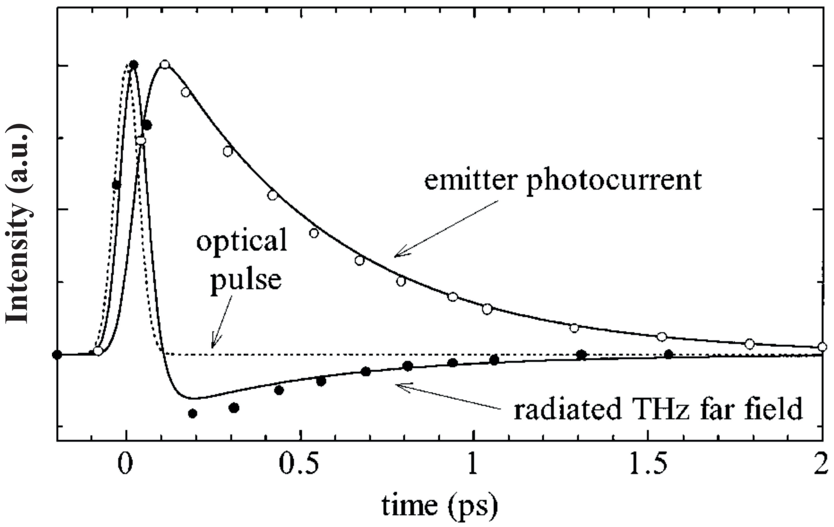

Figure 1.4: Calculated photocurrent in the emitter and amplitude of the radiated field versus time. The temporal shape of the laser pulse is drawn as a dotted line. Modified from [38]

the optical pulse and generate the photocurrent which are dependent on the photoconductive semiconductor properties.

The purpose of the photoconductive semiconductor is to act as an ultrafast switch, this requires the semiconductor to have high carrier mobility, short carrier lifetime and high dark resistance. Photoconductive semiconductors [39] such as low temperature (LT) grown GaAs and LT-InGaAs are used to generate THz radiation. These semiconductors are grown using molecular beam epitaxy (MBE), typical growth temperatures for standard GaAs and InGaAs is approximately 500° C to 600° C whereas the LT growths are grown at approximately 200° C to 300° C. The LT growth of GaAs increases the number of point defects within the crystalline structure which act as trapping sites that reduce carrier recombination times, the concentration of defects gives rise to semi-insulating properties [40] and subpicosecond carrier life times. GaAs has carrier life times of the order of a nanosecond [41] whereas the carrier life times for LT-GaAs and LT-InGaAs have been measured as low as 150 fs [42] and 500 fs [43] respectively. The number of defects within the LT semiconductor also decreases the carrier mobility and hence photoconductivity of the PCA. The reduction in photoconductivity limits the minimum carrier life times that can be achieved from increasing the number of defects before the THz performance of the PCA is compromised.

The bias voltage that is placed across the antenna electrodes to accelerate the carriers is dependent on the minimum gap size between the antenna electrodes. An electric field of a few MV/m is used for THz generation, so for a 10 μm gap this requires a bias voltage of 10 - 20 V. Photocurrents can be increased by increasing the bias voltage to produce greater acceleration of the carriers or by using more incident pump power to generate more carriers, however there is a threshold of maximum electric field and incident pump power which can be applied before electromigration within the semiconductor reduces the photoconductivity and causes permanent damage to the antenna.

Typically the carriers in the PCA are generated with excitation energies that are above the semiconductor band gap, this requires an ultrafast laser with a wavelength 800 nm for the bandgap of LT-GaAs which has traditionally been the bulky and expensive Titanium Sapphire laser. However the defect states [44] within LT-GaAs also enable below band gap excitation which has been demonstrated for both THz generation and detection [45, 46]. Research into below bandgap THz generation and detection is important because it allows the use of 1 μm laser technologies such as solid state and fiber lasers which are generally cheaper and more compact pump lasers than the Titanium Sapphire laser. An example of a 1 μm pump laser is the modelocked vertical external cavity surface emitting lasers (ML-VECSEL) which are compact, have multi-GHz repetition rates and could lead to a cost effective THz spectrometer system. A 1 μm VECSEL pumped THz spectrometer is demonstrated in chapter 5 and the THz performance is compared with a 800 nm Titanium Sapphire and 1035 nm Ytterbium glass solid state pump laser.

Photo-Dember

The photo-Dember effect [48, 49] is another method used for THz generation which also utilises ultrafast carrier transport within photoconductive semiconductors. A typical photo-Dember antenna (PDA) is shown in fig. 1.5, it consists of a gold strip deposited on the surface of LT-GaAs. The incident pump beam is focused onto the LT-GaAs near the edge of the gold strip to produce electron-hole pairs. Electrons and holes generated diffuse collinear to the semiconductor surface on the picosecond time scale which is dependent on the spatial carrier concentration gradient and their respective mobilities. The carrier diffusion produces dipoles that radiates THz radiation. The presence of the gold strip suppresses some components of the dipole due to

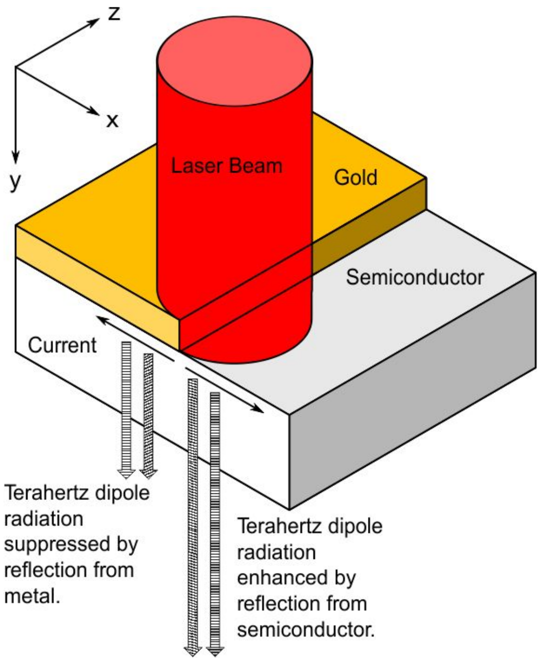

Figure 1.5: Schematic of a photodember antenna showing the generation of THz dipole radiation. Modified from [47].

reflections from the gold. This enhances the remaining dipoles and in effect enhances the THz emission. If the gold strip is not present the dipole does not cancel, but radiates in quadrupole configuration which has no theoretical emission in the direction of the detector. However, due to strong focusing geometries provided by the silicon lens and the parabolic, the quadrupole radiation can be detected although it is very weak.

Unlike PCA, the PDA does not require a bias voltage for THz generation, therefore it cannot be electrically short circuited which increases antenna life times. The properties of the THz radiation from the photo-Dember effect is dependent on the diffusion properties of the semiconductor. The mechanisms of photo-Dember THz generation is currently being researched [47, 50] by the THz group at the University of Southampton.

Non-linear

Pulsed THz radiation can also be generated using optical rectification which requires a material with a second order non-linear susceptibility such as zinc telluride (ZnTe). A second order non-linear polarisation P_2 induced by an two external optical electric fields $E_1 = E_0 \cos \omega_1 t$ and

$E_2 = E_0 \cos \omega_2 t$ can be described using [51],

$$P_2 = \chi_2 E_1 E_2 = \chi_2 \frac{E_0^2}{2} (\cos(\omega_1 - \omega_2)t + \cos(\omega_1 + \omega_2)t), \tag{1.3}$$

where χ_2 is the second order electric susceptibility of the material. The term $\omega_1 - \omega_2$ which corresponds to the generation of an electric field with the difference frequency is responsible for the THz generation. An ultrafast laser pulse that propagates through the non-linear crystal generates THz radiation from the mixing of the frequencies present within the spectral bandwidth of the laser pulse. The frequencies present must be phase matched for optimum THz generation, this can only occur over some finite length known as the coherence length. The coherence length limits the maximum crystal thickness that that can be used to generate a high signal with sufficient THz bandwidth. Thinner crystals generate more THz bandwidth due to better phase matching, however suffer from low signal because of the smaller interaction length. Furthermore, optical phonon resonances [52] can also occur at THz frequencies within the non-linear crystal which also reduce the signal.

1.2.2 THz pulse detection

Photoconductive

A PCA can also be used to measure the THz electric field, in principle photoconductive detection is the reverse of photoconductive generation. The probe beam is used to generate carriers within the PCA but no bias field is needed as the incident THz electric field is used to accelerate the carriers. The accelerated carriers produce a photocurrent which is proportional to the THz electric field and can be measured from the antenna electrodes by using a lock-in amplifier.

The receiver is only active as long as there is a photocurrent which is dependent on the carrier life time of the semiconductor, typically this is a few hundred femtoseconds. The receiver measures only a snapshot of the THz electric field that is incident on the receiver at that time, to construct the THz waveform many measurements of the THz pulse are taken at different times by using the delay stage which is shown in fig. 1.2. The time dependent photocurrent generated by the THz pulse as a function of the delay τ between the pump and probe pulse is given by the convolution of the THz electric field with the time dependent conductivity of the receiver [53],

$$i(t) = \frac{1}{T} \int_0^T E_{THz}(\tau) \sigma(t - \tau) dt, \tag{1.4}$$

where T is the laser repetition rate, E_{THz} is the incident THz electric field and σ is the receiver conductivity. The shorter the carrier generation and recombination time of the PCA the faster the detector response and less convoluted the measured THz electric field will be, this will result in a larger detected THz bandwidth.

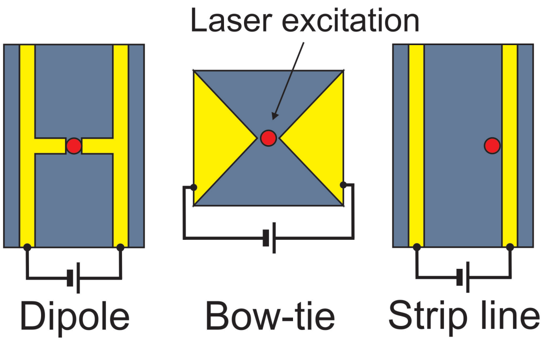

Figure 1.6: Schematic showing the dipole, bow-tie and strip-line photoconductive antenna with their typical laser excitation positions indicated by the red circle.

The antenna geometry can also determine the generated and detected THz bandwidth and signal, fig. 1.6 shows the schematic for a dipole, bow-tie and strip line antenna geometries. The laser excitation for both the dipole and bow-tie antenna is positioned in the middle of the electrode gap except the strip line which is near the anode, this is due to the trap-enhanced field [54] effect which enhances the optical injection of carriers near the anode, improving the efficiency of THz generation. These structures were compared with each other by Tani et. al. [55] which found that the bow-tie antenna was the least susceptible to saturation and produces the strongest signal with a large amount of low frequency components. The dipole antenna is the most susceptible to saturation which limits the emission power, the saturation is due to the electric field generated by the carriers which screens the bias field. The strip-line antenna generates the largest bandwidth but the power is relatively weak. Antenna geometries can be designed to enhance the THz emission, such as fractal [56, 57], spiral [58] and other complex geometries.

Non-linear

Electro-optic sampling [36, 59] of the THz pulse can be performed with a non-linear crystal such as ZnTe or GaSe using the Pockels effect. The Pockels effect is where an external electric field causes a linear change to the crystal birefringence. To measure the THz electric field the generated THz pulse and probe beam are made to propagate collinear to each other through the non-linear crystal. The THz electric field changes the crystal birefringence which changes the polarisation of the probe beam, by measuring the change in polarisation the THz electric field can be determined.

1.3 Other THz generation and detection methods

Terahertz quantum cascade lasers (QCL) [60] are a source of narrow band THz radiation which offer excellent spectral control, however designing THz QCLs is challenging due to waveguide loss from the free carrier absorption and to operate with direct THz transitions they require cryogenic cooling [61]. THz generation using intracavity difference-frequency generation of room temperature dual frequency mid-infrared QCLs has also been demonstrated [62]. THz radiation can be produced from free electron lasers (FEL) [63], synchrotrons [64] and gyrotrons [65]. Advanced Gunn diodes which can operate with multi-mW power in the THz region are also being developed [66] for single frequency imaging.

Field effect transistors (FET) have been demonstrated for terahertz detection [67], for example InP high-electron-mobility transistors (HEMT) have been used for terahertz imaging [68] and recently a THz detector based on a antenna-coupled graphene field-effect transistor was demonstrated [69]. THz radiation has also been generated and detected using high-T_c superconducting (HTS) Josephson junctions [70, 71]. Antennas have been integrated with hot electron bolometers for THz detection [72], pyroelectric cameras [73] and CMOS detectors [74] have also been used for THz imaging. Real-time imaging has been demonstrated using microbolometer cameras [75].

Fourier transform infrared (FTIR) spectroscopy [76] is a standard technique in infrared spectroscopy which can be extended into the THz region by using THz based sources and detectors mentioned above.

1.4 Material parameter extraction

In terahertz time domain spectroscopy (THz-TDS) broadband THz radiation which forms a THz pulse is generated and detected by a THz time domain spectrometer, should the THz pulse be incident on a material then the optical constants in the THz region for that material will modify the detected THz pulse. Both the amplitude and phase of the THz electric field is measured by a THz time domain spectrometer, this allows for the direct calculation of the real and imaginary components of the optical constants for a material to be determined over the THz bandwidth. The method of determining the optical constants is called material parameter extraction [77] and is the process of fitting a theoretical model of the THz pulse propagating through the material to the experimental data recorded by the THz spectrometer.

The accessibility of both the amplitude and phase of the THz electric field in THz-TDS should not be understated, it is extremely useful for material parameter extraction because it allows for both the real and imaginary components of the optical constants to be determined directly from the experimental data. In contrary, spectroscopic methods which measure only the power spectrum allow for only a single component of the optical constants to be determined. When only a single component of the optical constants is known then indirect and hence more complex methods such as the use of the Kramers-Kronig (K-K) relations are required to determine both components.

Material parameter extraction is a critical tool for the analysis of samples investigated using THz-TDS, the determination of the complex refractive index is essential in understanding material dispersion and absorption in the THz region. Material parameter extraction has been applied to a number of dielectrics [78] and semiconductors [79] to determine their complex refractive index, it has also been used to determine carrier concentrations [80] in thin metal films, molecular properties of liquid crystals [81] and dielectric properties of polar liquids [82].

The principle method of material parameter extraction that is used throughout the literature is the Fresnel model [77, 83, 84, 85] which models the propagation of the THz electric field through the sample using the well-known Fresnel transmission and reflection coefficients [86]. The Fresnel model is flexible in that it is relatively easy to construct a model for a different number of sample types whether it is a multilayered [87], optically thick or ultrathin [88, 89] sample. The closer the agreement between the theoretical model of the THz electric field propagating through the sample and the experimental data the more accurate [90, 91] the extracted complex refractive index.

The accuracy of the model is limited to the assumptions built into the model, for example the Fresnel model is only valid for samples that are homogeneous and planar because it neglects scattering loss. Scattering loss can occur when structure dimensions equivalent to THz wavelength are present within the sample, this is a characteristic of composite materials. In such cases models that include scattering loss based on effective medium theory [92, 93] or the K-K relations [94] are more suitable.

1.5 Outline of Thesis

The work present in this thesis aims to develop and understand the method of material parameter extraction in order to accurately determine the complex refractive index of materials using the Fresnel model. In chapter 2, I demonstrate a material parameter extraction method which models the THz electric field using the Fresnel coefficients under the assumption that the THz beam is a plane wave. The extraction method forms the basis of most work presented here, I discuss in detail the construction of the theoretical model of the THz electric field and the fitting procedure required to fit the theoretical model to the experimental data acquired from THz time domain scans. I also discuss phase unwrapping which is essential to determine the correct complex refractive index.

Optimising the model used in material parameter extraction is a difficult endeavour because the results are dependent on the assumptions of the model and initial parameters, in chapter 3 I will test the influence of initial parameters and assumptions of the model on the extracted complex refractive index. Understanding the behaviour of the extracted complex refractive index based on model assumptions and initial parameters can be used to determine the agreement between the model and experimental data. The assumed sample thickness, the number of reflections and noise of the model are all investigated. A noise suppression technique is demonstrated which can be used to increase the useful spectral bandwidth of an extraction and reveal spectral features that were difficult to detect beforehand. The imperfections between model and experimental data are investigated analytically to determine how these deficiencies can change the complex refractive index.

A common assumption made is that the THz beam in a plane wave even for results obtained at the focus of a THz beam. In chapter 4 I demonstrate a converging beam extraction method to investigate the effect of a converging beam on the complex refractive index. Furthermore, I use the converging beam extraction method to determine the angular beam profile of the focussed THz beam. Finally in chapter 5 I demonstrate a THz-TDS spectrometer being pumped using a

999 nm optically pumped modelocked vertical external cavity surface emitting laser (VECSEL), I then compare the THz-TDS spectrometer performance of the same THz spectrometer being pumped with a 800 nm Titanium Sapphire laser and a 1035 nm Ytterbium glass solid state laser.

Chapter 2

Principles of material parameter extraction

2.1 Introduction

Material parameter extraction is the analysis used to determine the complex refractive index of materials from their THz time domain scans which enables the characterisation and study of materials in the THz region. Determining the complex refractive index of a material is conceptually an inverse electromagnetic problem because the complex refractive index cannot be calculated directly from experimental THz time domain scans. The process of material parameter extraction requires the fitting of a theoretical model for the THz electric field to the THz-TDS data, where by the complex refractive index of the theoretical model is varied until it fits the experimental data. It requires close agreement between a model of the THz electric field propagation and experimental THz data for accurate extraction of the optical constants.

The principle extraction method which is used throughout this thesis is the Fresnel model which was demonstrated explicitly for the first time by L. Duvillaret et. al. [77] and has been used to investigate a number of different sample types, such as, multilayered [87], optically thick and ultrathin [88, 89]. The basis of this method is using Fresnel transmission and reflection coefficients to model the propagation of the THz pulse and constructing a theoretical transfer function of the sample. In order to determine the complex refractive index the theoretical transfer function is fitted to the experimental transfer function which is determined by the experimental data. The process of material parameter extraction can be summarised into three main steps which are listed below,

1. Calculate the experimental transfer function using the sample and reference scan.
2. Create a model of the THz propagation through the sample to produce a theoretical transfer function.
3. Fit the theoretical transfer function to the experimental transfer function to determine the complex refractive index.

In this chapter I explain these steps so that the reader can gain an understanding of the process of material parameter extraction and demonstrate an extraction algorithm which is the basis of all parameter extractions shown within this thesis. The extraction algorithm and any component of the algorithm was written and developed in the programming language Python. The Fresnel model which is presented, is for a single layered homogeneous material and assumes that the THz electric field is a plane wave, propagates at normal incidence to the sample and experiences no scattering loss. The Newton-Raphson method is used to fit the model to the experimental data, phase unwrapping which is integral to the material parameter extraction is also discussed. I will finish this introduction on the principles of material parameter extraction by discussing the THz time domain scans for the 567 μm fused silica sample used throughout this chapter.

2.1.1 THz time domain scans of fused silica

In THz-TDS time dependent measurements of both the amplitude and phase of the THz electric field are recorded. Should a material be present in the THz beam path the THz electric field will be modified due to the dielectric properties of the material. Fig. 2.1 shows two time dependent measurements of the THz electric field. The reference scan in black is a time domain scan for the electric field of a THz pulse passing through a nitrogen atmosphere and the sample scan in red is a time domain scan for the electric field of a THz pulse passing through a 567 μm fused silica sample.

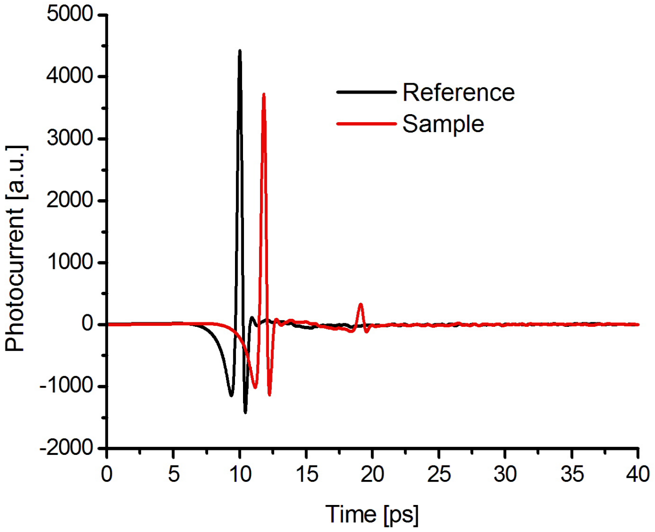

Figure 2.1: Time domain scans of the THz electric field of a 567 μm fused silica sample (red) and reference scan (black) taken using a TPS Spectra 3000.

The THz scans were taken by Dr. A. Zeitler at the University of Cambridge using a TPS Spectra 3000 Modular Terahertz Instrument (TeraView Ltd., Cambridge, UK), a schematic of the spectrometer is shown in fig. 2.2. The TPS Spectra 3000 uses PCA for THz generation and detection, each with a Si hemispherical lens mounted on the top. The emitted THz beam is collected by a 2 inch ellipsoid mirror which focuses the THz beam into the sample. An identical mirror is used to collect the transmitted THz beam and focus it onto the detector. The THz electric field is scanned using a fast delay with a 40 ps optical length, it is measured 1800 times and then averaged.

Comparing the differences between the sample and reference scan it is possible to determine information about the sample, for example the average refractive index of the fused silica sample is 2.08. The average refractive index can be determined by measuring the time difference between the main pulse in the reference and sample scan Δt and using the following equation,

$$n_{avg} = 1 + \frac{c\Delta t}{L}, \tag{2.1}$$

where L is the sample thickness and c is the speed of light in a vacuum. This is a basic measurement of the refractive index that neglects the frequency dependent information contained within

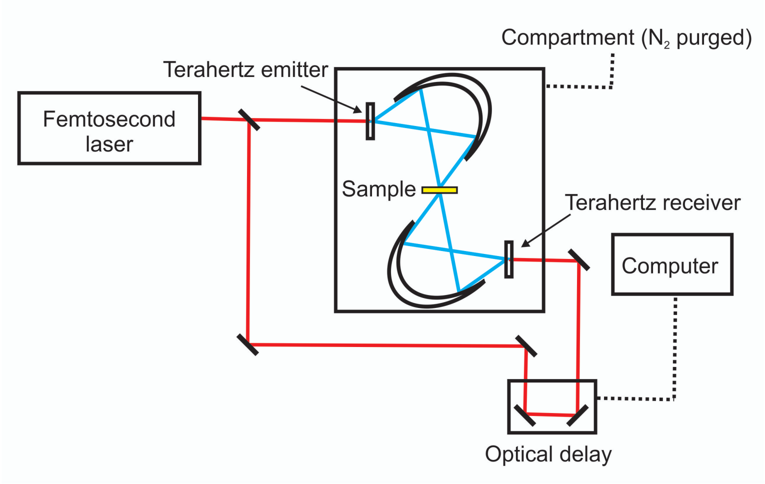

Figure 2.2: Schematic of a TPS Spectra 3000 Modular Terahertz Instrument (TeraView Ltd., Cambridge, UK).

the THz scans, to measure the frequency dependent complex refractive index a more complicated method is required. The definition of the complex refractive index is

$$\tilde{n}(\omega) = n(\omega) + i\epsilon(\omega), \tag{2.2}$$

where $n(\omega)$ is the refractive index and $\epsilon(\omega)$ is the extinction coefficient of the material. The real part of the complex refractive index is dependent on the speed at which the THz radiation travels through the material and the imaginary part of the complex refractive index is dependent on the attenuation in the amplitude of the radiation. Fig. 2.3 shows the amplitude of the THz spectra. The amplitude of the spectra is found by first taking the Fourier transform of the individual THz scans and then taking the natural logarithm of the Fourier transforms, the real component of the natural logarithm is the amplitude of the spectra.

The dynamic range of the spectra is 36 dB and the frequency resolution set by the scan length is 25.2 GHz. The spectra has a bandwidth of 0.1 to 4.0 THz, therefore it is possible to determine the complex refractive index over this range. Material parameter extraction is the analysis used to determine the complex refractive index over the range of frequencies present in the THz spectra.

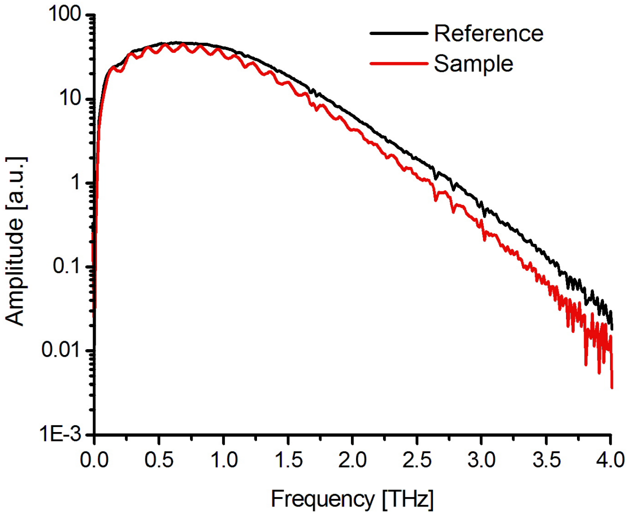

Figure 2.3: THz spectra of a 567 μm fused silica sample (red) and a reference scan (black) which taken using a TPS Spectra 3000.

2.2 Calculating the experimental transfer function

A transfer function is the frequency dependent relation between the input and the output of a system. If the transfer function of a system is known it can be used to determine the output for a given input provided that the system is linear and time invariant (LTI). Transfer functions have been used to characterise systems in broad area of fields such as digital filtering [95], economics [96] and physiology [97]. The relationship between the transfer function, input and output of a system can be expressed using,

$$Y(\omega) = H(\omega) \cdot X(\omega), \tag{2.3}$$

where $Y(\omega)$ is the output signal, $X(\omega)$ is the input signal, $H(\omega)$ is the transfer function of the system and ω is the angular frequency.

The time dependent equivalent of the transfer function is the impulse response which is the Fourier transform of its transfer function described by,

$$h(t) = \int_{-\infty}^{+\infty} H(\omega) \cdot e^{-i\omega t} d\omega, \tag{2.4}$$

where $h(t)$ is the impulse response. The output $y(t)$ from a the system is equal to its impulse response convoluted with the input $x(t)$, given by,

$$y(t) = h(t) * x(t). \tag{2.5}$$

The complex refractive index $\tilde{n}(\omega)$ is a frequency dependent variable and the subsequent model for the propagation of the THz electric field is also frequency dependent because of its inherent dependence on $\tilde{n}(\omega)$. Therefore this extraction method is performed in the frequency domain which requires the frequency dependent transfer function. The frequency dependent transfer function of the system can be determined from a given frequency dependent input and output like so,

$$H(\omega) = \frac{Y(\omega)}{X(\omega)}. \tag{2.6}$$

In material parameter extraction the traditional approach is take a sample scan with the sample placed in the THz beam and a reference scan without the sample placed in the THz beam. These two scans can be Fourier transformed to produce, $Y(\omega)$, the sample spectra and, $X(\omega)$, the reference spectra from which the experimental transfer function $H(\omega)$ can be determined. The material response from the various media which the THz pulse experiences as it propagates from the THz emitter to the THz detector is recorded in the THz spectra. The experimental transfer function $H(\omega)$ is the division of the $Y(\omega)$ the sample spectra by $X(\omega)$ the reference spectra. Therefore the effect on the THz electric field in the sample spectra due to its propagation up to the sample and after the sample will be divided out by the reference spectra provided that the experimental conditions are the same between each scan. The system which the experimental transfer function $H(\omega)$ describes is the material response of the sample and the column of air which is unoccupied by the sample in the reference scan. The response of the THz electric field due to the column of air which is embedded in the experimental transfer function is taken into account when modelling the theoretical transfer function which enables the determination of solely the sample response.

The first step to producing the experimental transfer function is to Fourier transform the THz scans shown in fig. 2.1 to produce THz spectra. To observe the amplitude and phase of the spectra the natural logarithm of the Fourier transform is taken as this separates the amplitude and phase of the spectra into real and imaginary components. The amplitude and phase of the spectra are shown in figures. 2.3 and 2.4 respectively. The peak amplitude of the spectra shown in fig. 2.3 is at 630 ± 15 GHz which is the peak frequency transmitted and received by the

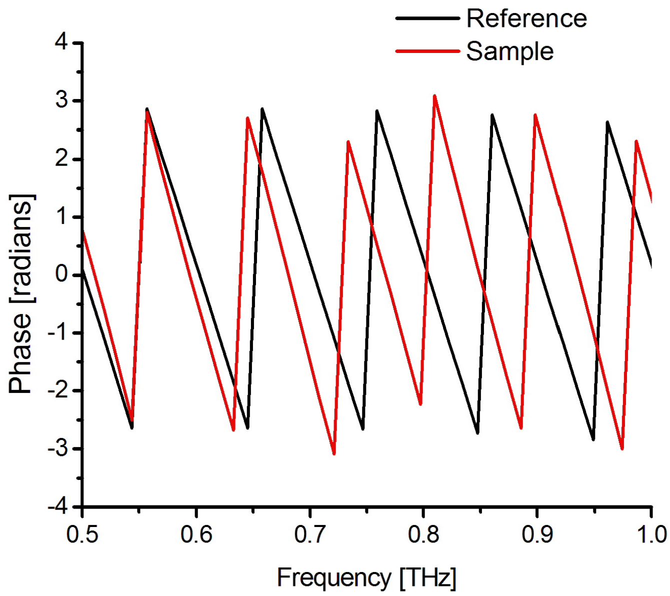

Figure 2.4: Phase of the sample and reference spectra over the frequency range of 0.5 - 1.0 THz. The phase is calculated from the Fourier transform of the sample and reference THz time domain scans.

THz-TDS setup, there are also dips in the amplitude in both reference and sample spectra which indicate absorption within the system. The phase of the spectra are wrapped between $\pm\pi$, this will produce a transfer function with a wrapped phase which must be corrected to determine the correct complex refractive index. The effects of wrapped phase and phase unwrapping are discussed in section 2.5.

The real and imaginary components of the experimental transfer function are shown in fig. 2.5. The experimental transfer function is an oscillating function with an amplitude that decays with frequency, the imaginary component is out of phase with the real component. It is more practical to show the amplitude of the transfer function which is shown in fig. 2.6, there are oscillations in the transfer function which have a frequency of 150 GHz. These oscillations originate from the etalon produced by the sample and are observed in the amplitude of the sample spectra with the same frequency. The reflected radiation from the sample interfaces produce constructive and destructive interference between the transmitted and reflection radiation which is frequency dependent. The frequency dependence of the oscillations is dependent on the free spectral range

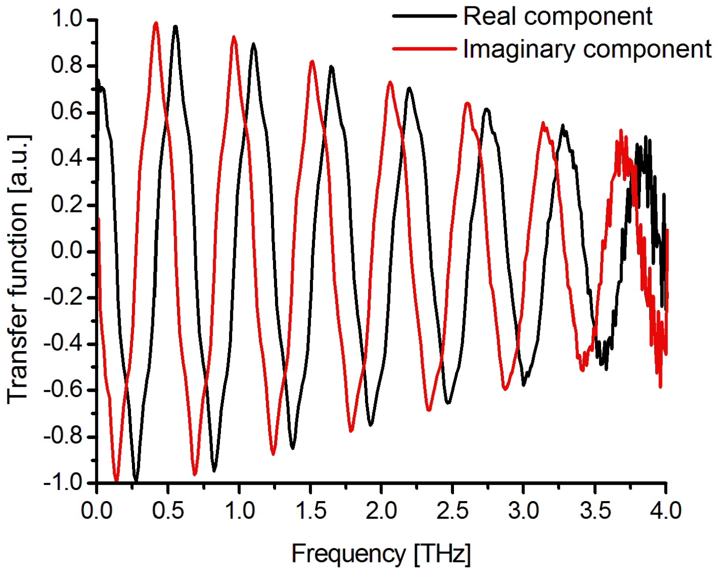

Figure 2.5: The real and imaginary component of the transfer function which was constructed from the division of the sample spectra by the reference spectra.

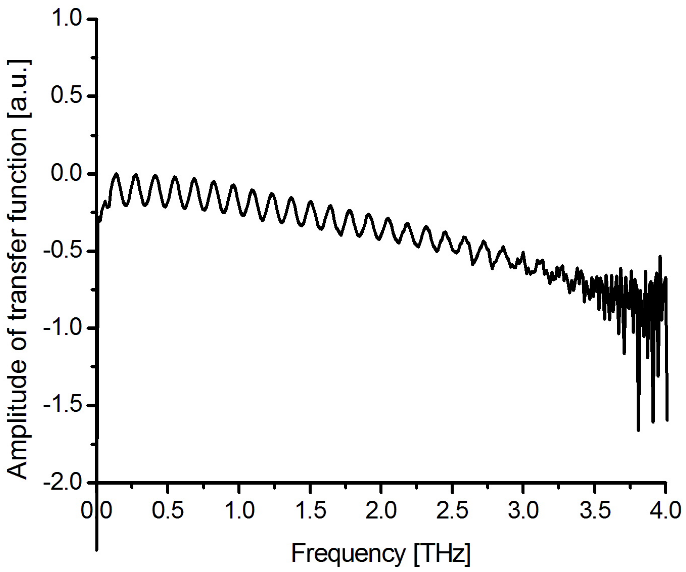

Figure 2.6: Amplitude of the transfer function which is calculated by taking the real component of the natural logarithm of the transfer function.

of the etalon given by,

$$\Delta\nu = \frac{c}{2nL}, \tag{2.7}$$

where c is the speed of light in a vacuum, n is the refractive index of the etalon and L is the etalon thickness. For an etalon with average refractive index of 2.0, thickness 567 μm the free spectral range is 150 GHz the same frequency as the oscillations observed in the amplitude of the transfer function. The etalon effect of the sample has been demonstrated as a method for frequency calibration of terahertz time-domain spectrometers [98] by comparing the THz-TDS transmission spectra of thin sample with a Fabry-Perot etalon model.

2.3 Modelling the THz electric field

The correct modelling for the propagation of the THz electric field is crucial for the accuracy of the extracted complex refractive index, the aim is to produce a model which describes the transfer function of the experimental data. The Fresnel equations are used to model the electric field of the THz pulse that is incident normal to the interface of two adjacent media with different complex refractive indices, the Fresnel transmission and reflection coefficients are given by,

$$T_{ab}(\omega) = \frac{2\tilde{n}_a(\omega)}{\tilde{n}_a(\omega) + \tilde{n}_b(\omega)} \tag{2.8}$$

and

$$R_{ab}(\omega) = \frac{\tilde{n}_a(\omega) - \tilde{n}_b(\omega)}{\tilde{n}_a(\omega) + \tilde{n}_b(\omega)}, \tag{2.9}$$

where T_{ab} and R_{ab} are the transmission and reflection coefficients respectively. $\tilde{n}_a$ and $\tilde{n}_b$ are the complex refractive indices of the two adjacent media which create an interface, ω is the angular frequency of the electric field and L is the length of the medium. The Fresnel coefficients only account for specular reflections and do not model diffuse reflections or scattered radiation that may be collected by the detector, therefore the sample should have polished surfaces at which the THz beam propagates through. The propagation coefficient for the THz electric field through a medium is also required and is given by,

$$P_a = e^{-i\tilde{n}_a(\omega)\omega L/c}, \tag{2.10}$$

where P_a is propagation coefficient, $\tilde{n}_a$ is the complex refractive index of the medium, ω is the angular frequency of the electric field and L is the length of the medium. The transfer function can be constructed from Fresnel equations and propagation coefficient by defining the THz electric field propagation for the sample spectra $Y(\omega)$ and reference spectra $X(\omega)$.

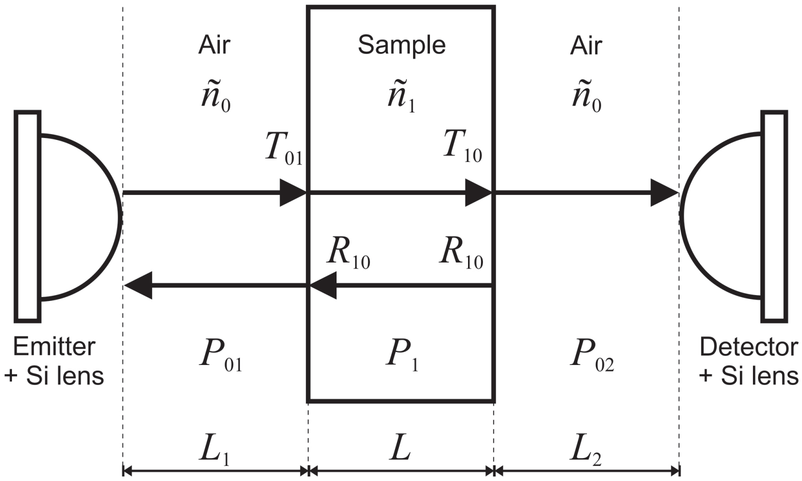

Figure 2.7: Schematic diagram showing the propagation of a plane wave THz beam in a sample scan. The THz beam propagates from the THz emitter, passes through the sample, and then propagates to the THz detector.

A schematic of the propagation of a plane wave THz beam passing through the sample with the relevant coefficients that are considered is shown in fig. 2.7 and an equivalent schematic for the reference scan is shown in fig. 2.8. The THz pulse propagates from the emitter to the sample through a section of air with length L_1, through the sample with thickness L and then from the sample to the detector through another section of air with length L_2. The electric field that propagates in the sample scan is defined by,

$$E_{sample}(\omega) = \eta(\omega) \cdot P_{01}(\omega, L_1) \cdot T_{01}(\omega) \cdot P_1(\omega, L) \cdot T_{10}(\omega) \cdot P_{02}(\omega, L_2) \cdot F_{refl} \cdot E(\omega), \tag{2.11}$$

$$F_{refl}(\omega) = \sum_{k=0}^{+\infty} \left\{ R_{10}(\omega) \cdot P_1(\omega, L) \cdot R_{10}(\omega) \cdot P_1(\omega, L) \right\}^k, \tag{2.12}$$

where η is the optical admittance which is the inverse of optical impedance of the system. The following terms are defined as P_{01} the propagation of the electric field from the THz emitter to the sample, T_{01} the transmission through the first sample interface, P_1 propagation through the sample, T_{10} transmission through the second sample interface and finally P_{02} the propagation from the sample interface to the receiver. $E(\omega)$ is the frequency dependent electric field of the THz radiation, the reflection coefficients are included in the term F_{refl} where k is the number

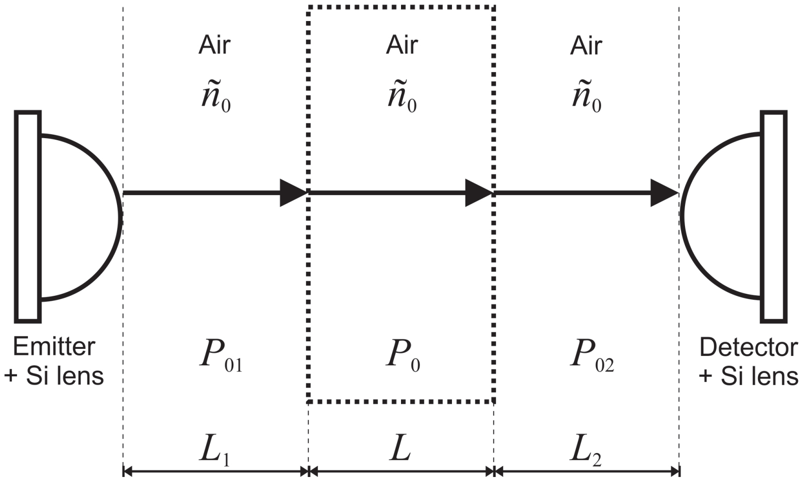

Figure 2.8: Schematic diagram showing the propagation of a plane wave THz beam in a reference scan. The THz beam propagates from the THz emitter, passes through a column of air that replaces the sample, and then to the THz detector.

reflections and R_{10} is the reflection coefficient for an electric field inside the sample incident on a sample air interface. The electric field for the reference scan is as follows,

$$E_{reference}(\omega) = \eta(\omega) \cdot P_{01}(\omega, L_1) \cdot P_0(\omega, L) \cdot P_{02}(\omega, L_2) \cdot E(\omega). \tag{2.13}$$

In this case the propagation terms considered which define the electric field propagation are P_{01} a section of air from the emitter to a column of air which is where the sample would be placed, P_1 the propagation through that column of air and then P_{02} which is another section of air to the receiver. The transfer function for an electric field propagating through a material is as follows,

$$H(\omega, \tilde{n}(\omega)) = \frac{E_{sample}(\omega, \tilde{n}(\omega))}{E_{reference}(\omega, \tilde{n}(\omega))}, \tag{2.14}$$

substituting in eqs. 2.11 and 2.13 leads to

$$H(\omega) = \frac{T_{01}(\omega) \cdot P_1(\omega, L) \cdot T_{10}(\omega)}{P_0(\omega, L)} \cdot \sum_{k=0}^{+\infty} \left\{R_{10}(\omega) \cdot P_1(\omega, L) \cdot R_{10}(\omega) \cdot P_1(\omega, L)\right\}^k . \tag{2.15}$$

The construction of the transfer function cancels the propagation terms to and from the sample (P_{01}, P_{02}) which allows for a simpler equation, this is under the assumption that the conditions of the THz beam path to and from the sample remain the same between scans. This method relies on the assumption that there is consistency of the experimental conditions between the sample and reference scan for optimum fitting of the Fresnel model to the experimental data.

The theoretical transfer function depends on the complex refractive index of the sample and also the complex refractive index of the medium which takes the place of the sample in the reference scan. If, for example, the scans are taken in an atmosphere which contains water vapour, then water absorption lines will appear in the complex refractive index as gain, therefore optimum extraction is achieved when the THz beam is under vacuum or nitrogen atmosphere. The theoretical transfer function uses Fresnel model equations which assume a planewave for the THz beam with no angular dependencies, therefore for optimum extraction the sample should be placed in a collimated beam with the sample surface normal to the beam propagation direction.

2.4 Fitting the transfer function

To find the complex refractive index $\tilde{n}$ of the sample the following equality must be solved

$$H_{theo}(\omega, \tilde{n}) = H_{exp}(\omega), \tag{2.16}$$

where $H_{theo}(\omega, \tilde{n})$ is the theoretical transfer function and $H_{exp}(\omega)$ is the experimental transfer function. Essentially the complex refractive index $\tilde{n}$ of the theoretical transfer function is varied until eq. 2.16 is satisfied, at which point the complex refractive index of the Fresnel model must be equal to the complex refractive index of the sample. To perform this task a fitting procedure must be formulated that can accurately fit the theoretical transfer function to the experimental transfer function. The Newton-Raphson method is the basis for the fitting procedure demonstrated here, the Nelder-Mead [84] method is another example which can be used. The Newton-Raphson method is a recursive root finding method given by,

$$x_{i+1} = x_i - \frac{f(x_i)}{f'(x_i)}, \tag{2.17}$$

where x_{i+1} is the root of the function $f(x_i)$, $f'(x_i)$ is the derivative and x_i is the previous iteration or initial value for the root. An example of the Newton-Raphson method is shown in fig. 2.9 where $f(x) = e^x - 10$. The initial guess is $x_0 = 5$, the value of $f(x_0)$ is calculated and divided by the gradient at x_0 which produces the difference term that is subtracted from the initial guess to find the next iteration x_1. The progression of the iteration is shown in fig. 2.9 by the red numbers, the iteration moves up the red dotted line from $x_0 = 5$ to the red cross $f(x_0)$ then moves down the green line to intersect $y = 0$ to find x_1. This process repeats until the change in x_i is at some minimum criteria. The inset graph of fig. 2.9 shows the value of x_i for each iteration, it shows negligible change after 5 iterations.

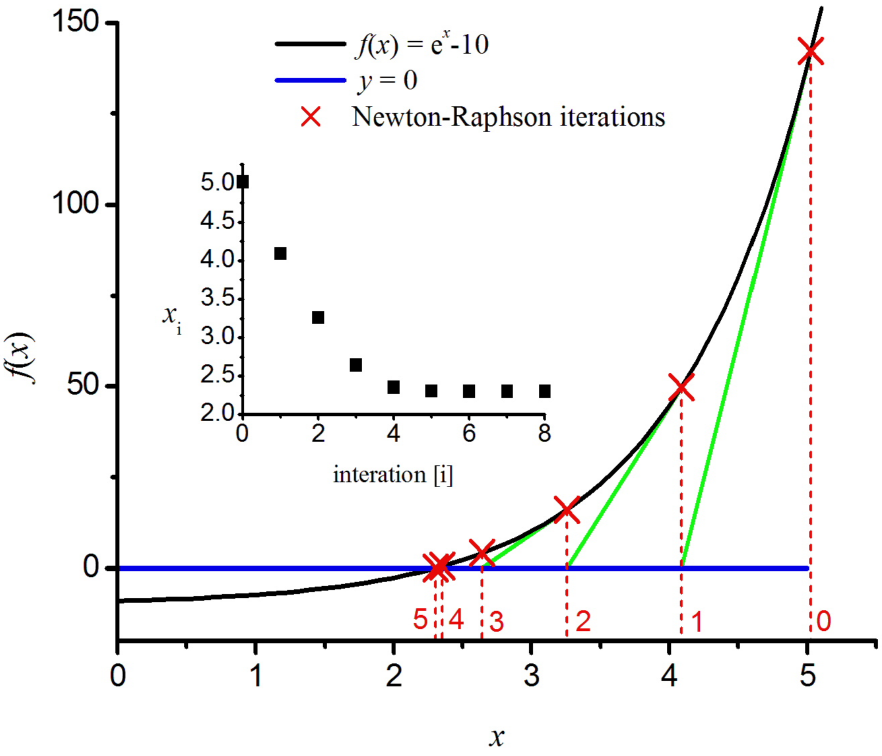

Figure 2.9: This figure shows the Newton-Raphson method applied to the function $f(x) = e^x - 10$, the initial starting value is $x_0 = 5$. The iterations are shown by the red crosses and the inset shows the value of x_i for each iteration i

The equality in eq. 2.16 must be modified so that it can be used by the Newton-Raphson method to find the complex refractive index $\tilde{n}$, the natural logarithm is taken and rearranged to give,

$$\ln(H_{theo}(\omega, \tilde{n}(\omega))) - \ln(H_{exp}(\omega)) = 0. \tag{2.18}$$

If the root $\tilde{n}$ of eq. 2.18 is found then the complex refractive index for the angular frequency ω has been determined, the function which is solved by Newton-Raphson method is,

$$f(\omega, \tilde{n}) = \ln(H_{theo}(\omega, \tilde{n}(\omega))) - \ln(H_{exp}(\omega)). \tag{2.19}$$

The derivative of $f(\omega, \tilde{n})$ is also required, remembering that $H_{exp}(\omega)$ is a constant the derivative is given by,

$$f'(\omega, \tilde{n}) = \frac{H'_{theo}(\omega, \tilde{n}(\omega))}{H_{theo}(\omega, \tilde{n}(\omega))}. \tag{2.20}$$

Taking the natural logarithm of the experimental and theoretical transfer functions is not essential for the Newton-Raphson method, however it does separate the amplitude and phase of the transfer function into the real and imaginary components which allows for convenient phase unwrapping of the experimental transfer function which is discussed in section 2.5.

It is now possible to find the complex refractive index of the material for different frequencies by substituting eq. 2.19 and 2.20 into the Newton-Raphson equation given by eq. 2.17. The material parameter extraction algorithm was written in Python which is a high level programming language that is able to process real and complex components collectively. This is unlike some extraction methods which treat the real and complex components separately and require separate routines to do this. The majority of fitting algorithms [77] fit to a transfer function in the frequency domain, it is generally simpler to fit in the frequency domain when the transfer function itself is a frequency dependent function. However some extraction methods fit in the time domain such as waveform rebuilding [83] which works by building a time domain sample scan constructed using a frequency dependent transfer function which is then compared with the experimental time domain sample scan. The error between the rebuilt and experimental sample scans are minimised by changing the complex refractive index, when the error is minimised the complex refractive index is known.

The Newton-Raphson algorithm uses an initial starting value for complex refractive index and when the change in complex refractive index between iterations is less than 10^{-7} the algorithm stops iterating. In general the Newton-Raphson algorithm would require tens of iterations to reach the accuracy criteria, if however the accuracy criteria was never met then after 100 iterations the algorithm would terminate to prevent the material parameter extraction algorithm from stalling. The algorithm starts at a frequency where the SNR is high and then steps down to zero frequency, it then steps up in frequency from the starting position to determine the complex refractive index at the higher frequencies. The difference between the theoretical transfer function that was fitted using the Newton-Raphson method and the experimental transfer function is shown in fig. 2.10. The difference between the theoretical and experimental transfer function is typically less than 10^{-12} which is five orders of magnitude smaller than the Newton-Raphson accuracy criteria and suggests the Newton-Raphson algorithm is adequate for the fitting process. The relative size of the peaks and dips shown in fig. 2.10 in comparison to the Newton-Raphson accuracy criteria (10^{-7}) suggest they are of no spectral significance.

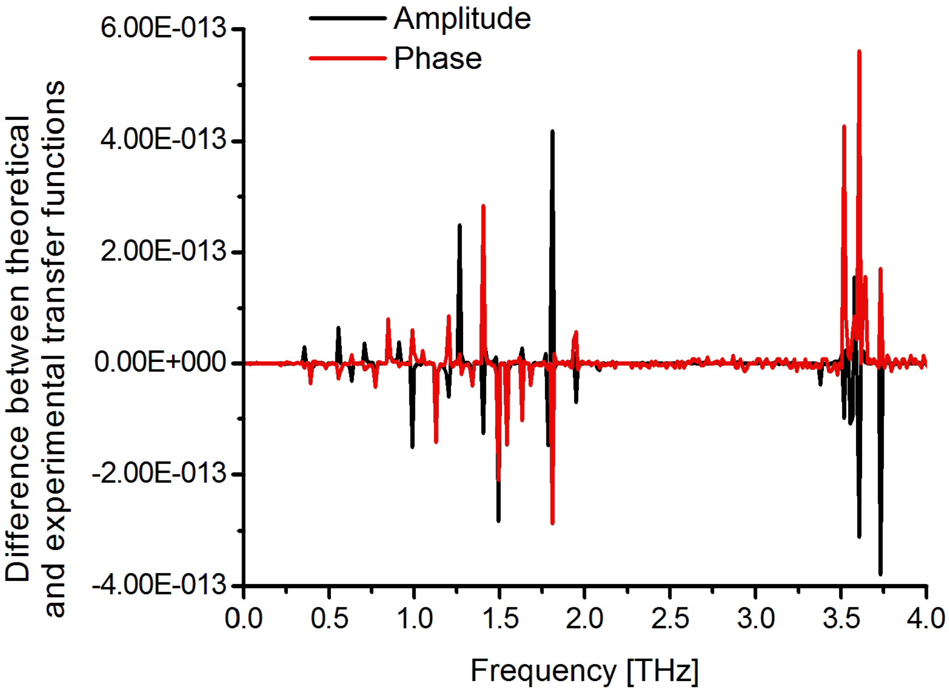

Figure 2.10: The difference between the theoretical transfer function fitted using the Newton-Raphson method and the experimental transfer function. The difference is typically less than 10^{-12} which is five orders of magnitude smaller than the Newton-Raphson accuracy criteria of 10^{-7}, this suggests the Newton-Raphson algorithm is adequate for the fitting process.

The material parameter extraction algorithm constructed using the theory in this chapter was used to determine the complex refractive index of a 567 μm fused silica sample, the THz time domain scans for the 567 μm fused silica sample is shown in fig. 2.1. The extracted refractive index and extinction coefficient are shown in fig. 2.11 and 2.12 respectively, they both show noise at high and low frequencies where the SNR of the THz scans become low. The extinction coefficient becomes positive at low frequencies which could be interpreted as amplification of THz radiation at those frequencies, however it is a consequence of the low SNR of the THz scans at low frequencies. There are also oscillations on the refractive index and extinction coefficient that have a frequency 150 GHz which are due to the etalon produced by the sample and the assumed infinite reflections of the theoretical transfer function. Optimisation of the length parameter which is detailed in section 3.2 was used in order to reduce the etalon oscillations. The extracted complex refractive index of a 567 μm fused silica sample demonstrates that the material parameter extraction method works, this extraction method forms the basis for the following chapters on material parameter extraction. Optimisation techniques are applied to this extraction method in chapter 3 and the extraction method is extended in chapter 4 to enable analysis of a converging THz beam. In the future this extraction method will be adapted further by other members of the THz group at the University of Southampton to investigate different samples such as liquid crystals, thin films such as multi-crystalline graphene. Also my converging beam extraction algorithm can be used to estimate angular profiles just by two measurements of an arbitrary sample at the focused and collimated of the THz beam. This gives an elegant new solution to angular beam profiling of focused THz beams.

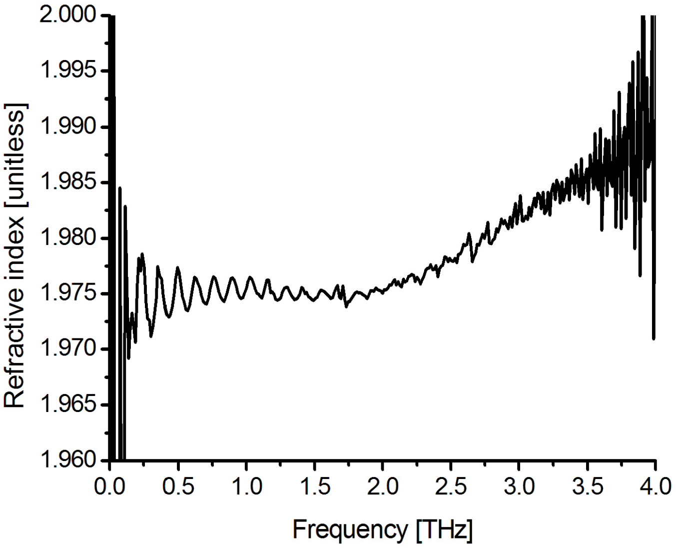

Figure 2.11: Refractive index extracted using infinite reflection model transfer function of a 567 μm fused silica sample. An optimum length parameter of 555 μm was used in the extraction to reduce the etalon oscillations. The extraction is noisy below 0.25 THz and above 3.0 THz where the SNR of the THz scans are low.

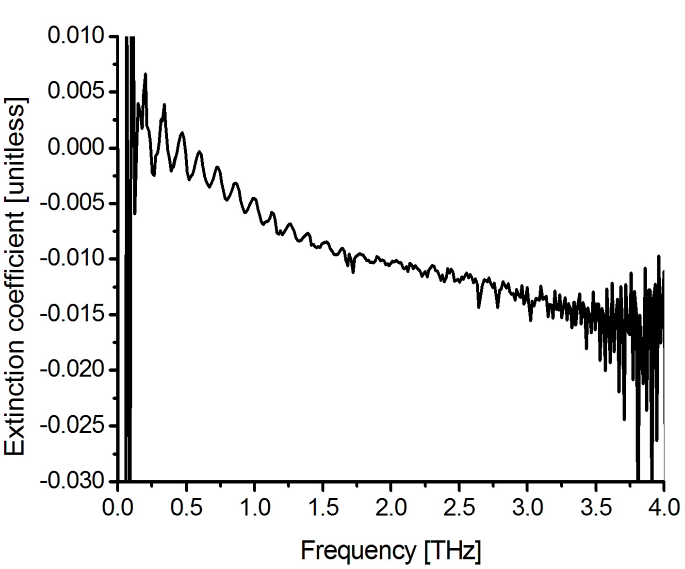

Figure 2.12: Extinction coefficient extracted using infinite reflection model transfer function of a 567 μm fused silica sample. An optimum length parameter of 555 μm was used in the extraction to reduce the etalon oscillations. The extraction is noisy below 0.25 THz and above 3.0 THz where the SNR of the THz scans are low.

2.5 Phase corrections

In THz-TDS, although the phase of the experimental transfer function is known there are corrections which must be applied to the phase to reconstruct the correct phase. These corrections are applied before fitting the theoretical transfer function to the experimental transfer function and are necessary because fitting the theoretical transfer function to the incorrect phase will produce an incorrect complex refractive index.

2.5.1 Origin of wrapped phase

The phases of the THz spectra shown in fig. 2.4 are wrapped, this means the phase is restricted to the values of $\pm\pi$. The experimental transfer function is dependent on these spectra hence it is also wrapped. The phase of the experimental transfer function must be unwrapped otherwise the complex refractive index that is extracted will be incorrect.

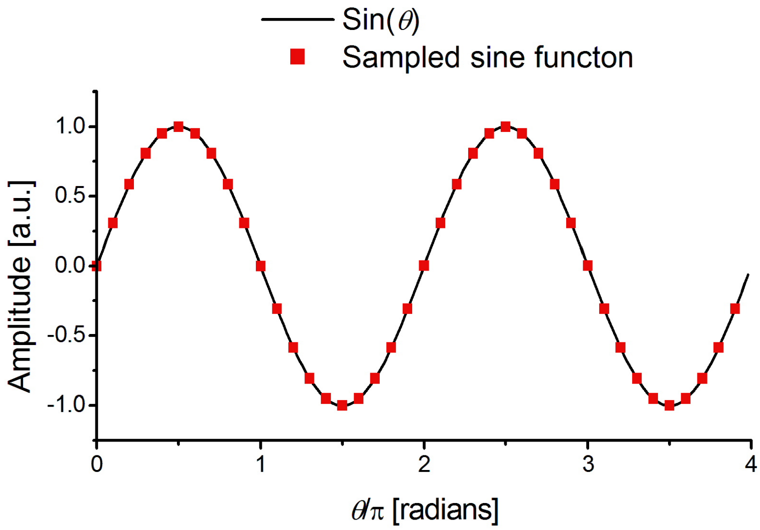

Figure 2.13: An example of a sinusoidal function $y = \sin(\theta)$ (black) which has been sampled (red dots).

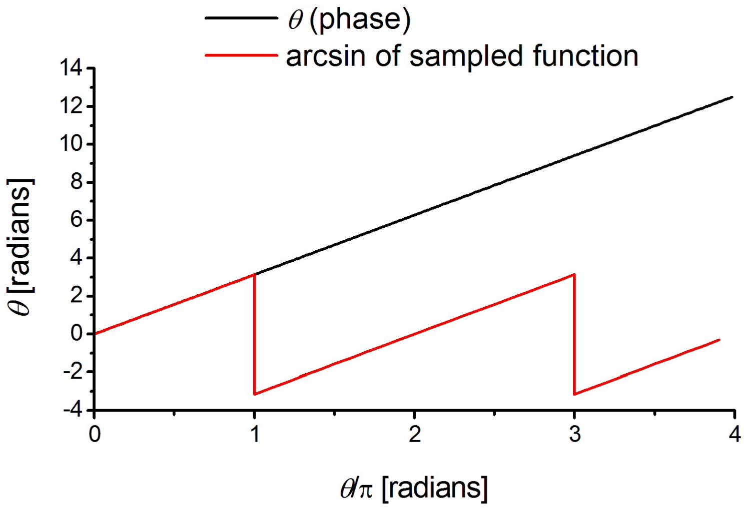

Figure 2.14: An example of the calculated phase (red) from the sampled points which becomes wrapped phase and the original phase (black).

The origin of the wrapped phase is demonstrated in figures 2.13 and 2.14, it shows an example of how the phase θ of the sinusoidal function $y = \sin(\theta)$ will become wrapped when attempting to calculate the original phase from y. This is analogous to calculating the phase of a THz spectrum from a THz time domain scan. The continuous function $y = \sin(\theta)$ is shown in fig. 2.13 by the continuous black curve, the function was sampled every 0.1 radians from 0.0 to 4.0 radians to produce a discrete data set shown by the red squares. The discrete data set is equivalent to a THz spectrum which is comprised of individual data points for each frequency component. The recovery of the phase θ from the data set of y is found by using the inverse function ($\theta = \arcsin(y)$), the resulting phase is shown in fig. 2.14 by the red sawtooth waveform which indicates the wrapped phase. This is due to the inverse sinusoidal function restricting the output between $\pm\pi$, it is restricted because there is ambiguity in the output y. In other words there are multiple values of θ separated by 2π which will give the identical result of y and the inverse sinusoidal function gives the first order result only. The original value of θ is shown by the black line in fig. 2.13, phase unwrapping is the recovery of the original phase from the sawtooth waveform.

2.5.2 Phase unwrapping algorithm

Phase unwrapping of the experimental transfer function is shown in fig. 2.15 for a 567 μm fused silica sample, the original phase is shown by the black sawtooth waveform and the unwrapped phase is shown by the red line. The phase unwrapping algorithm works by detecting the discontinuities in the phase that are larger than 1.4π which identifies where the 2π steps in the phase occur in frequency. The algorithm then adds $-2p\pi$ to a section of the phase that is in between step p and $p + 1$, for example the phase section in between the first and second step will have -2π added and the phase section between the second and third step will have -4π added to the phase. It is important to start phase unwrapping algorithm where the SNR is high, extract to the lower frequencies first then move from the high SNR position to the higher frequencies.

The SNR of the THz scans at the high frequencies is low due to the finite bandwidth of the THz spectrometer, this is where there is low signal in both amplitude and phase of the experimental transfer function which causes the solutions of the complex refractive index to break down in the extraction process. The phase unwrapping begins at 510 GHz, a consequence of starting the phase unwrapping where the SNR is high is that the intercept of the phase with

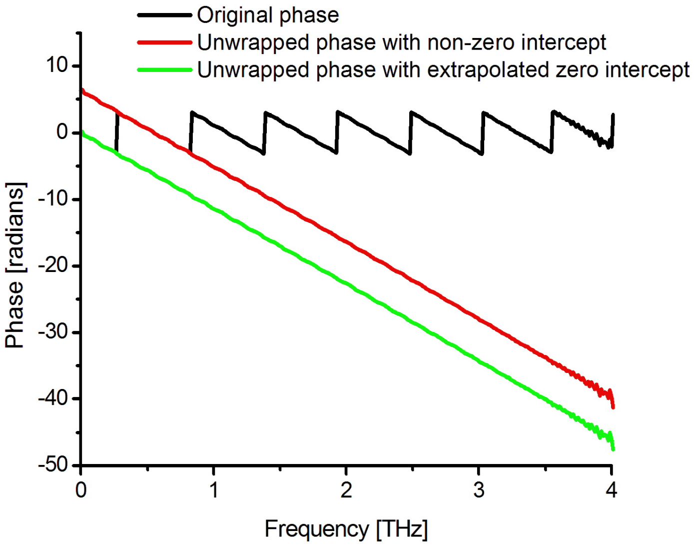

Figure 2.15: Phase unwrapping of the experimental transfer function for a 567 μm fused silica sample showing the original phase, unwrapped phase with non-zero intercept and unwrapped phase with zero intercept that was extrapolated using a linear regression on the unwrapped phase. The phase is negative because the sample causes a phase delay.

the y-axis is not necessarily at zero phase which is seen by the red line shown in fig. 2.15. This has been corrected by forcing zero phase at zero frequency shown by the green line, in order to do this the y-intercept from the unwrapped phase (red line) was calculated using a linear regression. The value of the y-intercept was then subtracted from the unwrapped phase to give zero phase at zero frequency, the importance of the phase at the y-intercept is discussed below.

2.5.3 Phase intercept

The phase relationship between each frequency component of the THz pulse is dependent on the complex refractive index $\tilde{n}(\omega)$ of the propagating media. Under vacuum the phase relationship between each frequency component will be linear because as the frequency increases the phase of the EM wave at a particular position will increase proportional to that frequency increase due to the constant refractive index, however for a sample it will be dependent on its complex refractive index $\tilde{n}(\omega)$. The phase of the sample and reference scan can be represented as complex exponential functions,

$$Y(\omega) = R_y(\omega)e^{-i\theta_y(\omega)}, \tag{2.21}$$

$$X(\omega) = R_x(\omega)e^{-i\theta_x(\omega)}, \tag{2.22}$$

where $Y(\omega)$ and $X(\omega)$ is the spectrum of the sample and reference scan respectively, R and θ is the amplitude and phase of the corresponding THz spectrum which depend on the angular frequency ω. The experimental transfer function is given by

$$H_{exp}(\omega) = \frac{Y(\omega)}{X(\omega)}, \tag{2.23}$$

which leads to

$$H_{exp}(\omega) = \frac{|R_y(\omega)|}{|R_x(\omega)|}e^{-i(\theta_y(\omega)-\theta_x(\omega))}. \tag{2.24}$$

The phase of the experimental transfer function is the subtraction of the phase in the sample scan from the phase in the reference scan. Therefore the intercept of the phase is dependent on the two phases, should the phase of the sample and reference scan tend to zero at zero frequency then so will the experimental transfer function. If we consider the propagation of a THz pulse through a slab of material, the THz pulse can be deconstructed into the constituent frequency components. As the frequency of the components decreases to zero the wavelength will increase to infinity and the phase of the frequency components that is incident on the detector will also tend to zero. Therefore the phase should intercept zero at zero frequency in order to extract the correct complex refractive index, should the phase intercept be a non-zero value the extracted complex refractive index will be incorrect.

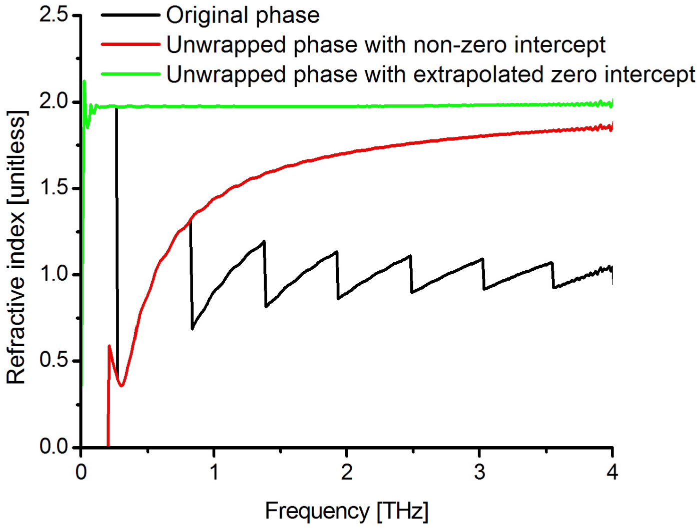

Figure 2.16: Refractive index extracted with original phase and unwrapped phase with a zero and non-zero intercept. The refractive index extracted with unwrapped phase that has a zero intercept shows the correct refractive index.

The refractive index and extinction coefficient of a 567 μm fused silica sample was extracted using the original wrapped phase, unwrapped phase with non-zero intercept and unwrapped phase with a zero intercept. Optimisation of the length parameter which is discussed in section 3.2 was used in the extraction process to reduce the etalon oscillations. The extracted refractive indices are shown in fig. 2.16. The refractive index extracted with the original phase shows a saw tooth curve which is similar to the original phase and the refractive index extracted using the unwrapped phase with non-zero intercept shows a curve. The refractive index which is extracted with unwrapped phase with zero intercept shows a linear refractive index in comparison to the other phase conditions used in the extraction process. The behaviour of the refractive index extracted with unwrapped phase with zero intercept is consistent with the behaviour of the refractive indices other forms of silica in the THz region [78].

The extinction coefficient is shown in fig. 2.17, it shows an oscillating curve for each phase

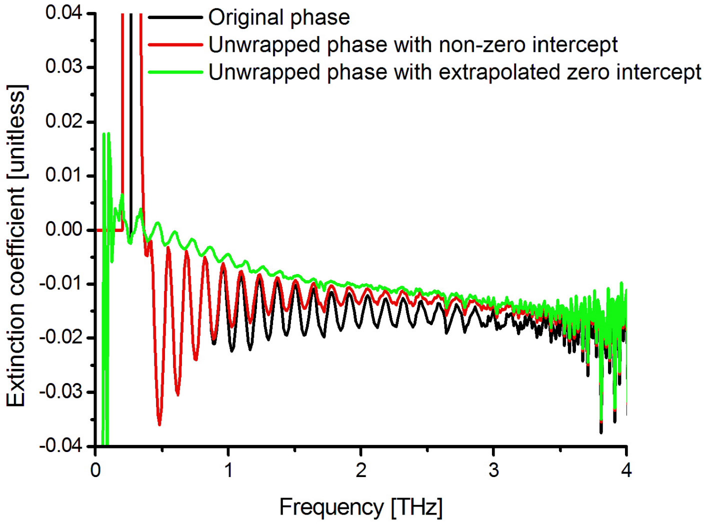

Figure 2.17: Extinction coefficient extracted with original and unwrapped phase with a zero and non-zero intercept. The extinction coefficient extracted with unwrapped phase that has a zero intercept shows an average extinction coefficient closer to zero than the others which suggests lower absorption.

condition. The extinction coefficient extracted with the original phase shows the largest oscillation amplitudes, the unwrapped phase with non-zero intercept shows slightly smaller oscillation amplitude and both of these extractions fail at low frequencies also seen in the refractive index. The extraction fails because the Newton-Raphson fitting procedure exceeds 100 iterations without reaching the accuracy criteria which suggests a solution is unlikely to be found. The extinction coefficient extracted with phase unwrapping that has also been extrapolated with a zero intercept shows no extraction failure at low frequency, it has the smallest oscillation amplitudes and has an extinction coefficient closer to zero which indicates smaller absorption. The results of the extracted complex refractive index suggest that the phase unwrapping algorithm is adequate for material parameter extraction.

The phase unwrapping with zero phase intercept is a critical process in material parameter extraction to find the correct complex refractive index. In the fitting process the natural logarithm of the theoretical transfer function is fitted to the natural logarithm of the experimental transfer function, that means the real and imaginary components of the transfer function are the amplitude and phase respectively. Therefore at each frequency the Newton-Raphson method fits the real component and the imaginary component of the theoretical transfer function to the amplitude and phase of the experimental transfer function using two variables the refractive index and extinction coefficient. There are multiple values for the refractive index and extinction coefficient of which the theoretical transfer function can be fitted to the amplitude and phase of the experimental transfer function. It is important to use phase unwrapping so that the theoretical transfer function is fit to the correct phase which ensures that the correct refractive index and extinction coefficient are extracted.

2.6 Comparison of the refractive index of fused silica and quartz

During my PhD research various THz time domain data were made available to me for analysis, each with different characteristics depending on the spectrometer and sample being investigated. These characteristics suited some investigations better than others. The initial THz spectra that were used to test the material parameter extraction algorithm were taken by myself at the University of Southampton. In particular many THz time domain scans of fused silica and quartz were acquired which are used throughout this work and a comparison of their respective complex refractive indices highlight the uncertainty found in their extracted complex refractive due to variations between different quartz samples and the characteristics of the different THz spectrometers. The material parameter extraction method that was detailed in this section was used to find the refractive index of each sample which are shown in fig. 2.18.

The avaliable THz scans were of a 567 μm, 1090 μm and 2054 μm fused silica sample taken by Dr. A. Zeitler at the University of Cambridge using a TPS Spectra 3000 Modular Terahertz Instrument (TeraView Ltd., Cambridge, UK). The TPS Spectra 3000 is shown in fig. 2.2 and the respective data from this spectrometer is labelled TeraView data. A scan of a 2000 μm quartz sample was also taken by Dr. A. Zeitler at the University of Cambridge using an experimental THz spectrometer which is discussed in section 4.4.1, the respective data is labelled Cambridge data. Finally a 2000 μm fused silica sample scan was taken on a spectrometer at the University of Southampton which is labelled Southampton data.

A range of 2.10 - 2.14 for refractive index of the quartz sample (Cambridge data) are shown in fig. 2.18 in comparison the the literature D. Grischkowsky et. al. determined the refractive index

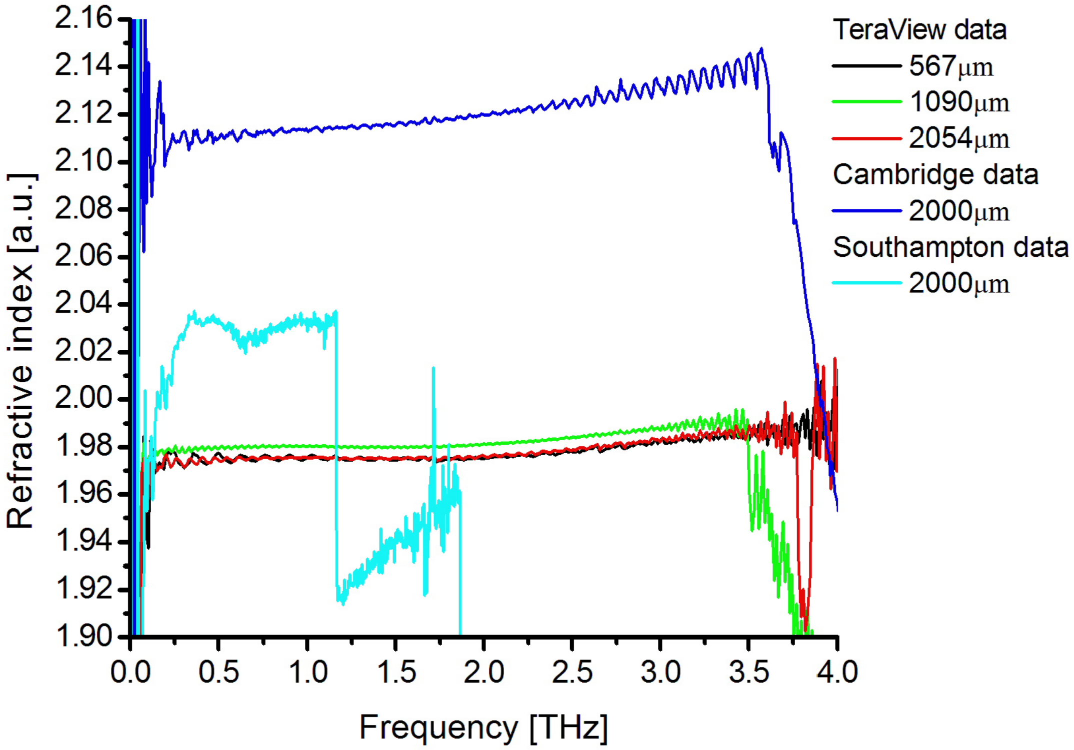

Figure 2.18: Refractive index extracted for different fused silica and quartz data using different THz spectrometers and the same material parameter extraction method. The TeraView data are from fused silica samples which are of the same grade, indicated by the proximity of their refractive indices. The Southampton data is from a fused silica sample and the Cambridge data is from a quartz sample. The figure highlights the variations in refractive index which can occur for different fused silica samples.

for crystalline quartz to be between 2.106 - 2.114 for an ordinary ray and 2.152 - 2.162 for the extraordinary ray over 0.1 - 2.0 THz [79]. Similar measurements were made by E. Castro-Camus et. al. who determined the average refractive index of crystalline quartz for the extraordinary and ordinary rays to be 2.16 and 2.11 respectively over the same THz range [99]. The refractive index of the TeraView fused silica samples range from 1.97 - 1.98 where as the refractive index of the Southampton fused silica sample range between 2.02 - 2.04, there is no definitive value for the refractive index of fused silica which has been obtained under THz-TDS within the literature. The TeraView fused silica samples are the same grade (spectrosil) of fused silica and the proximity of their refractive indices which required the optimisation of the length parameter which is detailed in section 3.2 demonstrates this. M. Naftaly et. al. measured the average refractive index of polycrystalline quartz to be 1.95 over 0.1 - 2.5 THz [78] which is also similar to the refractive index of the TeraView fused silica samples.

The ambiguity in the refractive indices between the different fused silica and quartz samples shown here and found within the literature make it difficult to determine which is the correct refractive index. Furthermore, the ambiguity in the refractive indices is exacerbated due to the presence of the imperfections in the experimental method and extraction process. Understanding these imperfections and how they influence the extracted complex refractive index are discussed throughout section 3. Knowledge of the exact refractive index of materials facilitates the creation of optical circuits, such as waveguides, gratings, integrated interferometers etc. Also there is not always the ability to measure complex refractive index change and accurate complex refractive index determination could facilitate comparisons between different studies.

Chapter 3

Material parameter extraction optimisation techniques

3.1 Introduction

In material parameter extraction there is the motivation to optimise the model with the experimental conditions because the closer the agreement [90, 91] between the model and experimental data the greater the accuracy of the extracted complex refractive index. Therefore it is crucial to understand how the model assumptions and initial parameters affect the behaviour of the complex refractive index, so that the agreement between model and experimental data can be determined. This can lead to various optimisation techniques which can improve the accuracy of the model and hence extracted complex refractive index such as length determination [100, 85, 88] and noise suppression [101].

In this chapter I will investigate the behaviour of the complex refractive index for different model assumptions and initial parameters, such as the assumed sample thickness and the number of reflections present within the model compared to the experimental data. I will demonstrate a method of noise suppression by modifying the theoretical transfer function to model noise. Finally, I will analytically determine the deficiencies in the transfer function between model and experimental data for a number of effects to investigate what impact this is expected to have on the extracted complex refractive index.

3.2 Length parameter

The length parameter, L, is the sample thickness of the model described by the theoretical transfer function. The closer the agreement between the length parameter and physical sample thickness the more accurate the extracted complex refractive index will be. The length parameter has a significant effect on both the real and imaginary components of the complex refractive index because it is present in the argument of the propagation term given by eq. 2.10 which contains both real and imaginary components.

In this section I demonstrate the behaviour that the length parameter has on the outcome of the complex refractive index by adjusting the length parameter to values which are different than the measured sample thickness. Understanding the behaviour has lead to methods for precise sample thickness determination [100] which is useful in cases where it is impractical to make physical measurements of the sample thickness such as multilayered samples, thin films and samples with thickness variations.

I initially demonstrate the behaviour that the length parameter has on the extracted complex refractive index using simulated data where all material parameters are known, I then apply the same demonstration to experimental THz time domain scans of three different fused silica samples. the physical measurement for the thicknesses of the three fused silica samples have been made are 567 μm, 1090 μm and 2054 μm. I will show that there is an optimum length parameter which can be deduced from the behaviour of the extracted complex refractive index and suggests optimum fitting of the Fresnel model to the experimental data.

3.2.1 Simulated data

The behaviour of the length parameter on the extracted complex refractive index was first analysed using simulated data. Simulated data has the advantage that the original material parameters are known and there are no experimental errors. An algorithm was produced to generate a simulated scan with set parameters for the sample thickness and complex refractive index. The simulated sample scan was generated by applying the theoretical transfer function (see eq. 2.15) to the experimental reference scan in fig. 2.1 using eq. 2.3. The material parameters for the simulated sample scan was a sample thickness of 555 μm and a complex refractive index of 1.980 - 0.005i which is constant with frequency. Simulated sample scans were generated for transfer functions which contained both infinite and zero reflections. A zero reflection transfer function contains no Fresnel reflection term, it is used to determine changes in complex refractive index due to the transmission of the THz electric field. The complex refractive index of the simulated sample scans were then determined using material parameter extraction with different length parameters close to the sample thickness. The extraction process used the original experimental reference scan and the respective transfer function for the number of reflections that was initially used to generate the simulated scan.

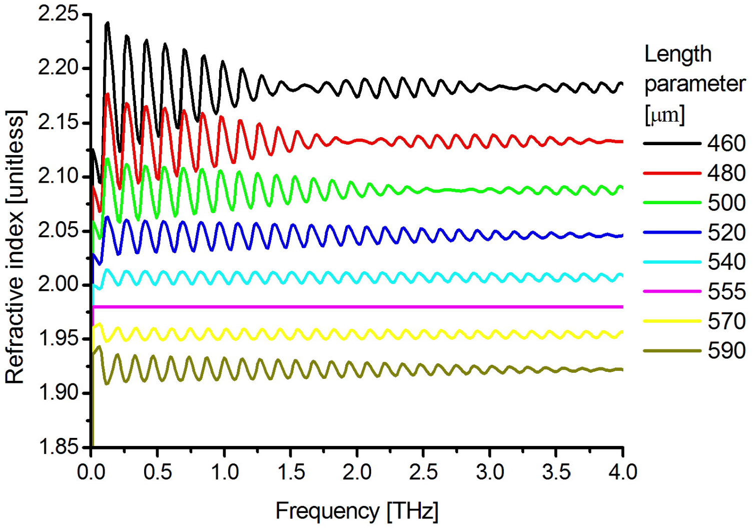

Figure 3.1: Refractive index of simulated data for a sample with a 555 μm thickness and a complex refractive index of 1.980 - 0.005i which was extracted using different length parameters. Both the simulated data and extraction process used a transfer function with infinite reflections. The refractive index (magenta) using the 555 μm length parameter shows the correctly extracted refractive index of 1.980 which is constant with frequency.

The effect on the refractive index

The effect on the refractive index due to a change of the length parameter for the simulated data is shown in fig. 3.1. The correct refractive index of 1.980 is extracted for a length parameter of 555 μm which is the original simulated sample thickness. The refractive index changes when a length parameter other than the sample thickness is used; the changes that occur are a shift in the average refractive index and presence of etalon oscillations. As the length parameter is increased the average refractive index decreases, the length parameter determines the extracted refractive index such that it is consistent with the phase of the experimental transfer function. In other words the Fresnel model of the theoretical transfer function compensates for an increasing path length by allowing the THz pulse to propagate at a faster speed through the sample so that the THz pulse always experiences the same time delay observed in the THz time domain scan.

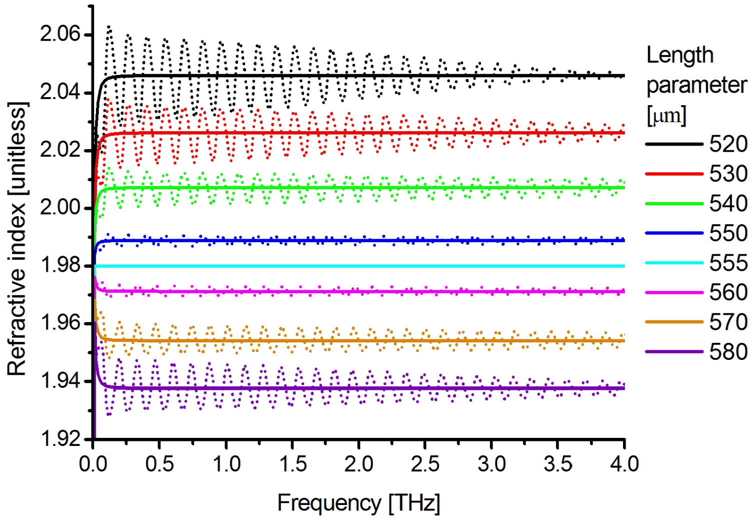

Figure 3.2: The solid lines show the refractive index of simulated data produced using the zero reflection transfer function for a sample with a 555 μm thickness and a complex refractive index of 1.980 - 0.005i. The refractive index was extracted using a zero reflection transfer function and truncated data with different length parameters to observed the effects from the transmission component of the transfer function. The dotted lines show the refractive indices that were simulated and extracted using the infinite reflection transfer function which contains reflections, hence the etalon oscillations.

The effect due to transmission components

The change in refractive index due to the zero reflection transfer function compared to the infinite reflection transfer function are shown in fig. 3.2, it shows that the shift in the refractive index due to the different length parameters is produced from the transmission component of the theoretical transfer function and the Fresnel reflection term is responsible for the etalon oscillations. Fig. 3.3 shows the average refractive index that was calculated for the range of a length parameters 100 μm to 1000 μm using the zero reflection transfer function. The change in average refractive index with length parameter is non-linear, as the length parameter tends to infinity the average refractive index tends to the asymptote of 1 and as the length parameter tends to zero the average refractive index will tend to infinity.

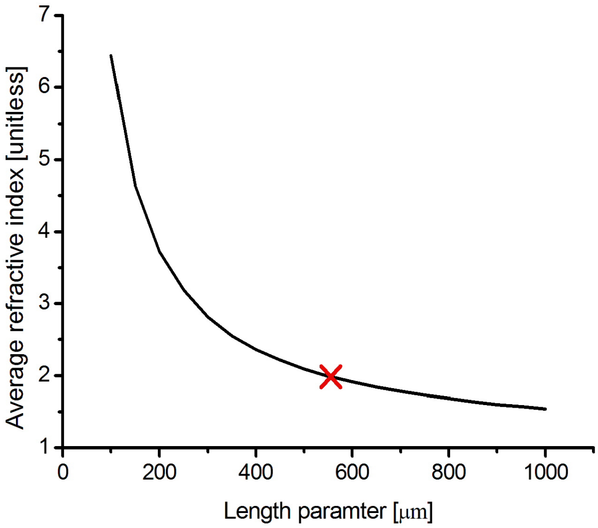

Figure 3.3: The dependence of the average refractive index on the length parameter of simulated data using the zero reflection transfer function for a sample with a 555 μm thickness and a complex refractive index of 1.980 - 0.005i. The refractive index was extracted using a zero reflection transfer function with different length parameters. The red cross indicates the refractive index for the optimum length parameter of 555 μm.

The effect due to reflection components

The etalon oscillations that are caused by the Fresnel reflection term are dependent on the length parameter, as the length parameter deviates from the actual sample thickness oscillations occur on the refractive index with increasing amplitudes. The difference in the phase of the oscillations between the overestimated and underestimated refractive indices is π. The frequency of the etalon oscillations on the refractive index is dependent on the free spectral range of the sample given by eq. 2.7. The envelope of the etalon oscillations in fig. 3.1 show frequency beating.

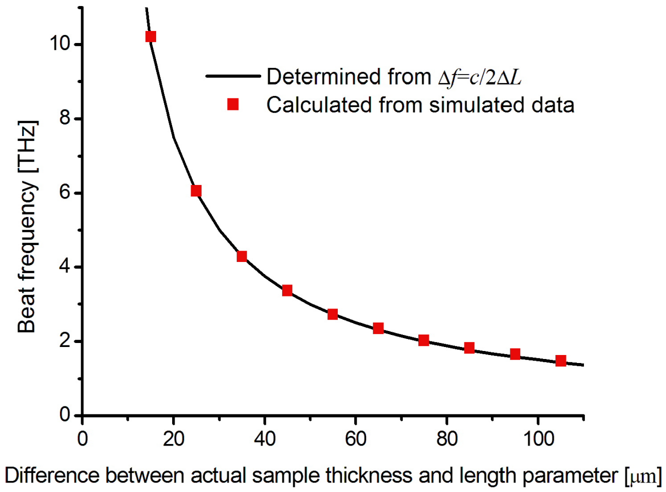

Figure 3.4: Beat frequency of the envelope of the etalon oscillations for the difference between the actual thickness and length parameter that occurs on the refractive index determined from the simulated data and using eq. 3.1.

The beat frequency measured from the extracted refractive indices for the difference in actual thickness and length parameter is shown in fig. 3.4 and was also determined by,

$$\Delta f \simeq \frac{c}{2\Delta L}, \tag{3.1}$$

where Δf is beat frequency per unit frequency and ΔL is the difference between the actual thickness and length parameter used. The variation of the etalon oscillation amplitudes on the refractive index indicate how close the Fresnel model fits the experimental data and can be used to determine how close the length parameter is to the actual sample thickness. This technique of minimising the etalon oscillations in the refractive index has been used to determine the precise sample thickness of optically thick samples, it was initially demonstrated by L. Duvillaret et. al. in 1999 [100]. It was also been demonstrated by T. Dorney et. al. in 2001 [85] and more recently has been applied to sub-100-μm by M. Scheller et. al. in 2009 [88]. The behaviour of the refractive index with respect to the chosen length parameter which has been demonstrated within the literature is in close agreement with the simulated data that was presented above. In section 3.2.2 I determine the optimum length parameter of fused silica samples with different thicknesses.

The effect on the extinction coefficient due to the transmission components

The change in extinction coefficient due to different length parameters with the zero reflection transfer function is shown in fig. 3.5, the correct extinction coefficient of -0.005i is extracted when the length parameter is set to the original simulated sample thickness. The behaviour of the extinction coefficient due to a different length parameter from the transmission component can be explained by two effects. First there is a frequency dependent change in the average extinction coefficient and second there is a linear shift in the average extinction coefficient but this is obscured by the first effect.

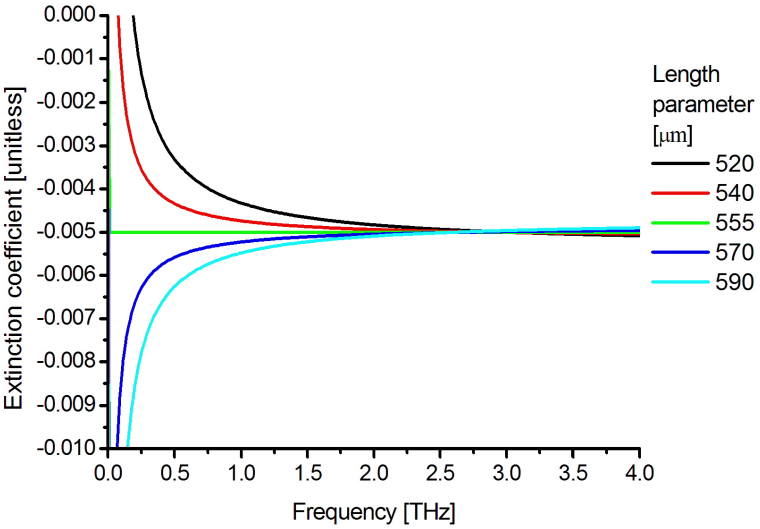

Figure 3.5: Extinction coefficient of simulated data produced using the zero reflection transfer function for a sample with a 555 μm thickness and a complex refractive index of 1.980 - 0.005i. The extinction coefficient was extracted using a zero reflection transfer function with different length parameters. The extinction coefficient (green) using the 555 μm length parameter shows the correctly extracted extinction coefficient of -0.005i which is constant with frequency.

The linear shift in the extinction coefficient is the smaller of the two effects and is analogous to the shift in refractive index. As the length parameter is increased the average extinction coefficient increases, the length parameter determines the extracted extinction coefficient such that it is consistent with total absorption of the sample. The total absorption of the sample is determined by the sample thickness and absorption per unit length, the absorption per unit length is related to the extinction coefficient by,

$$\alpha = \frac{2\omega\kappa}{c}, \tag{3.2}$$

where α is the absorption coefficient per unit sample length, ω is the angular frequency, κ is the extinction coefficient and c is the speed of light. The theoretical transfer function compensates for an increasing path length by reducing the absorption per unit length, this is equivalent to increasing absorption coefficient so that the THz pulse always experiences the same total absorption which is given by the amplitude of the experimental transfer function. The linear shift is obscured by the curvature imposed onto the extinction coefficient.

If a length parameter, different to the sample thickness is used, then the extracted average extinction coefficient becomes frequency dependent. The extinction coefficient increases with frequency for an overestimated length parameter and decreases with frequency for an underestimated length parameter. The determination of the extinction coefficient is dependent on the fit of the real part of the theoretical transfer function to the amplitude of the experimental transfer function, the real part of the theoretical transfer function contains both the refractive index and extinction coefficient. Therefore the extracted extinction coefficient is also dependent on the extracted refractive index, any frequency dependence observed on the refractive index can be imposed onto the extinction coefficient and vice versa.

The effect of the length parameter on the extinction coefficient due to the complex refractive index can be determined analytically by considering the transmission component of the theoretical transfer function,

$$T = \frac{4\tilde{n}}{(\tilde{n}+1)^2} e^{i(\tilde{n}-1)\omega L/c}, \tag{3.3}$$

where $\tilde{n}$ is the complex refractive index of the sample, the surrounding medium has a complex refractive index of 1, L is the length parameter, ω is the angular frequency of the THz radiation and c is the speed of light. The simulated data is generated with complex refractive $\tilde{n}$ and thickness L. It is then analysed with length parameter $L + \delta L$ to find the complex refractive index $\tilde{n} + \delta\tilde{n}$. Changes $\delta\tilde{n}$ and δL in $\tilde{n}$ and L lead to a change in $\log T$, which is given by

$$\frac{\partial \log T}{\partial \tilde{n}}\delta\tilde{n} + \frac{\partial \log T}{\partial L}\delta L. \tag{3.4}$$

If $\log T$ does not change we get

$$\delta\tilde{n} = -\frac{\partial \log T/\partial L}{\partial \log T/\partial \tilde{n}}\delta L. \tag{3.5}$$

The derivatives are

$$\frac{\partial \log T}{\delta L} = -i(\tilde{n}-1)\omega/c, \tag{3.6}$$

and

$$\frac{\partial \log T}{\delta \tilde{n}} = \frac{1}{\tilde{n}} - \frac{2}{\tilde{n}+1} - i\frac{\omega L}{c} = -\frac{1}{\tilde{n}}\left[\frac{\tilde{n}-1}{\tilde{n}+1} + i\frac{\tilde{n}\omega L}{c}\right]. \tag{3.7}$$

Substituting the derivatives into eq. 3.4 gives

$$\delta\tilde{n} = -\frac{-i\tilde{n}(\tilde{n}-1)\omega/c}{(\tilde{n}-1)/(\tilde{n}+1) + i\tilde{n}\omega L/c}\delta L. \tag{3.8}$$

Eqn. 3.8 determines how a change in length parameter will change the complex refractive index due to the transmission component of the transfer function. Changes to the extinction coefficient due to the extracted refractive index will be determined by the imaginary component of eqn. 3.8 with the assumption that $\tilde{n}$ is essentially real, this gives

$$\frac{-in\omega(n-1)^2/(n+1)c}{[(n-1)/(n+1)]^2 + [n\omega L/c]^2} \tag{3.9}$$

and this term is always negative so increasing the length parameter leads to the imaginary part of the refractive index becoming more negative. At THz frequencies the second term in the denominator is larger than the first, so the shift in the imaginary part decreases with frequency. The frequency dependent change on the extinction coefficient is on the same magnitude as the frequency dependent change on the refractive index, it is more visible on the extinction coefficient than the refractive index because the relative size of the extinction coefficient is smaller.

The effect on the extinction coefficient due to the Fresnel components

The change in extinction coefficient due to different length parameters with the infinite reflection transfer function is shown in fig. 3.6. The top figure shows length parameters less than 555 μm and the bottom figure shows length parameters greater than 555 μm. The Fresnel component of the theoretical transfer function introduces oscillations onto the extinction coefficient with the same behaviour that was observed on the refractive index. The amplitudes of the oscillations increase with the mismatch between length parameter and sample thickness, the oscillations also display frequency beating. The amplitudes of the oscillations are greater than the change of extinction coefficient due to the transmission component of the theoretical transfer function.

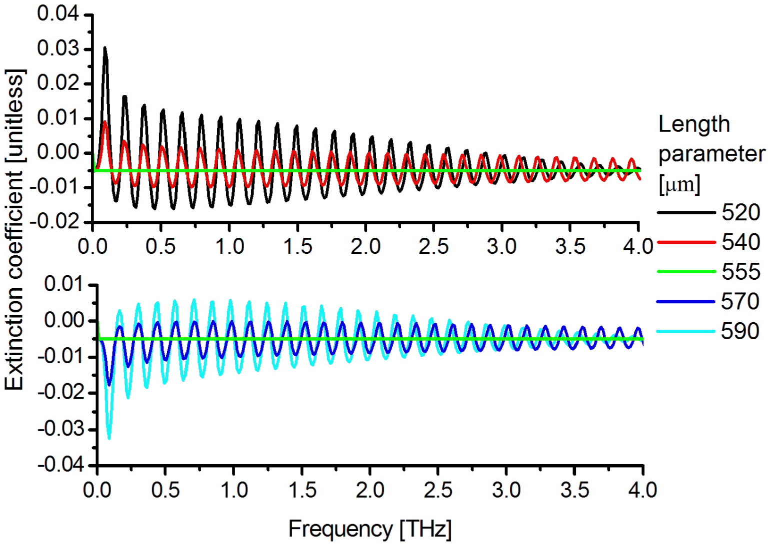

Figure 3.6: Extinction coefficient of simulated data produced using the infinite reflection transfer function for a sample with a 555 μm thickness and a complex refractive index of 1.980 - 0.005i. The extinction coefficient was extracted using an infinite reflection transfer function with different length parameters. The top figure shows length parameters less than 555 μm and the bottom figure shows length parameters greater than 555 μm. The extinction coefficient (green) using the 555 μm length parameter shows the correctly extracted extinction coefficient of -0.005i which is constant with frequency.

3.2.2 Experimental data

The effect of the length parameter on the complex refractive index of fused silica was investigated, THz data for the three fused silica samples used were taken by Dr. A. Zeitler on the TPS Spectra 3000 shown in fig. 2.2. The samples were synthetic fused silica of the same grade with thicknesses 567 μm, 1090 μm and 2054 μm. The complex refractive index for each of these samples was extracted using the infinite reflection transfer function for different length parameters.

The effect on the refractive index

The extracted refractive index for the 567 μm fused silica sample is shown in fig. 3.7, the length parameter was varied between 460 μm and 590 μm. The range of length parameters were chosen to show sufficient coverage of the refractive index.

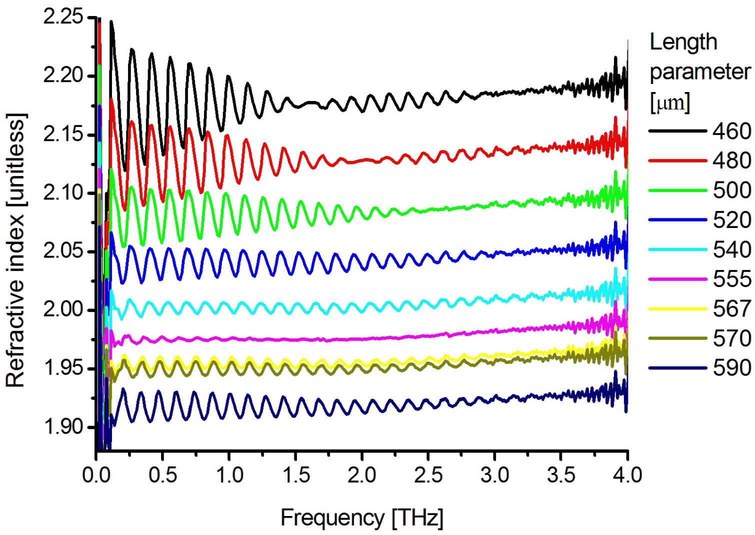

Figure 3.7: Refractive index of fused silica with thickness 567 μm extracted with different length parameters using the infinite reflection transfer function. The refractive index (magenta) using the 555 μm length parameter shows the optimum extraction indicated by the reduced oscillation amplitudes. The refractive index (yellow) using the measured thickness of 567 μm is also shown.

The effect on the refractive index due to the length parameter has the same features as the simulated data in fig. 3.1. There is a shift in the average refractive index and there is a change in the amplitude of the Fresnel oscillations which display frequency beating. The oscillation amplitudes are smallest when a length parameter of 555 μm is used, this is the optimum length parameter and suggests that the Fresnel model is in close agreement with the experimental data.

The same behaviour of the refractive index was also observed when the length parameter was varied on the THz data for the 1090 μm and 2054 μm fused silica samples. Fig. 3.8 shows the extracted refractive for the 1090 μm fused silica sample where the length parameter was varied from 960 μm to 1100 μm. The optimum length parameter where the oscillation amplitudes are minimum for the 1090 μm fused silica sample was 1070 μm. Fig. 3.9 shows the extracted refractive for the 2054 μm fused silica sample where the length parameter was varied from 1980 μm to 2054 μm. The optimum length parameter where the oscillation amplitudes are minimum for the 2054 μm fused silica sample was 2010 μm.

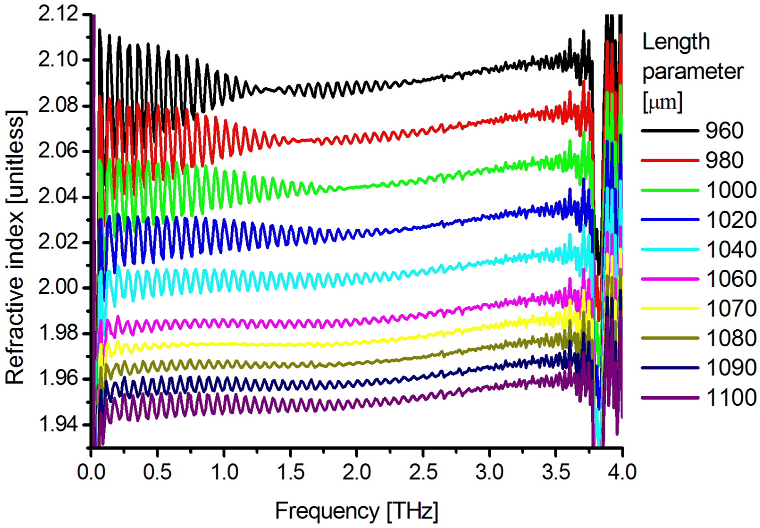

Figure 3.8: Refractive index of fused silica with thickness 1090 μm extracted with different length parameters using the infinite reflection transfer function. The refractive index (yellow) using the 1070 μm length parameter shows the optimum extraction indicated by the reduced oscillation amplitudes. The refractive index (navy) using the measured thickness of 1090 μm is also shown.

The change in average refractive index and oscillation amplitudes is dependent on the length parameter used relative to the optimum length parameter. That is why the greatest oscillation changes are observed on the refractive index of the 567 μm fused silica sample, and the smallest on

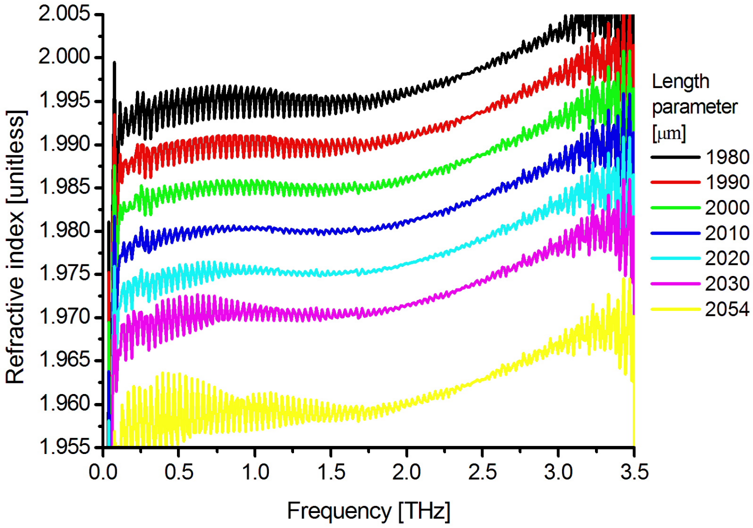

Figure 3.9: Refractive index of fused silica with thickness 2054 μm extracted with different length parameters using the infinite reflection transfer function. The refractive index (blue) using the 2010 μm length parameter shows the optimum extraction indicated by the reduced oscillation amplitudes. The refractive index (yellow) using the measured thickness of 2054 μm is also shown. The frequency dependent behaviour of the refractive index is more evident in this figure than the 567 μm and 1090 μm fused silica samples because the scale is smaller.

the 2054 μm fused silica sample. The scale for refractive index of the 2054 μm fused silica sample is smaller than the 567 μm and 1090 μm fused silica samples and so the frequency dependence of the refractive index is magnified. The optimum length parameters of the 567 μm, 1090 μm and 2054 μm fused silica samples were 555 μm, 1070 μm and 2010 μm respectively, which is a difference of approximately 2% to their respective measured thicknesses.

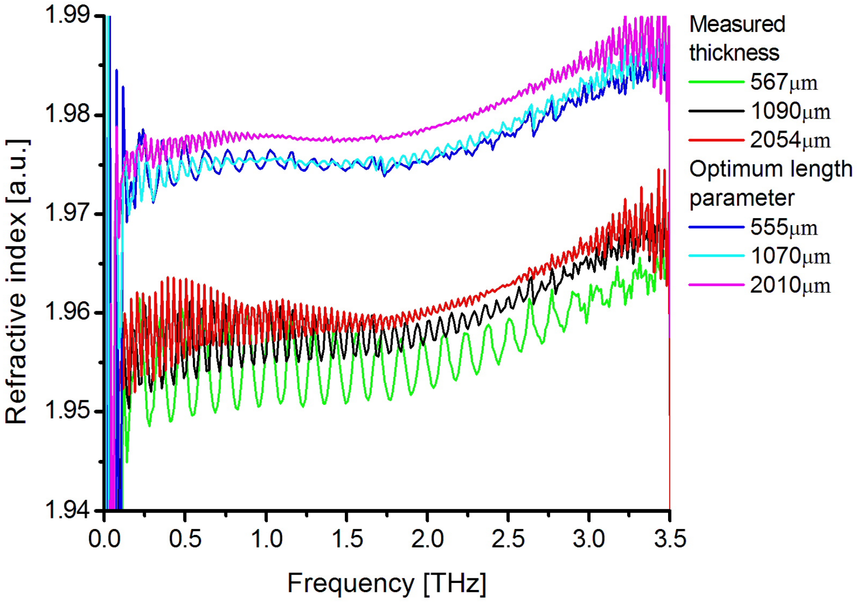

Figure 3.10: A comparison of refractive indices extracted using the measured thickness and optimum length parameter for the 567 μm, 1090 μm and 2054 μm fused silica samples.

Fig 3.10 shows a comparison of the refractive indices using the measured thickness and optimum length parameter for each fused silica sample. The refractive indices for each fused silica sample using the optimum length parameter not only show a reduction in the oscillation amplitudes, but also converge to a similar average refractive index. The samples are the same grade of synthetic fused silica, hence the consistency of the refractive indices between each fused silica sample is expected. The observations on the refractive indices using different length parameters show that the Fresnel model is in closer agreement to the experimental data for the optimum length parameter than the measured thickness. Provided there are no experimental errors due to the THz spectrometer or data acquisition then these observations suggest the actual thicknesses of the fused silica samples are 555 μm, 1070 μm and 2010 μm.

The effect on the extinction coefficient

The extracted extinction coefficient using different length parameters for the 567 μm, 1090 μm and 2054 μm fused silica samples is shown in figures 3.11, 3.12 and 3.13 respectively. The effect on the extinction coefficient due to the length parameter has the same features as the simulated data in fig. 3.6. Fresnel oscillations are present on the extinction coefficient which are dependent on the length parameter, for each fused silica sample there is an optimum length parameter where the oscillations are minimised. The optimum length parameters for the extinction coefficient are the same as the refractive index, which for the 567 μm, 1090 μm and 2054 μm fused silica samples are 555 μm, 1070 μm and 2010 μm respectively.

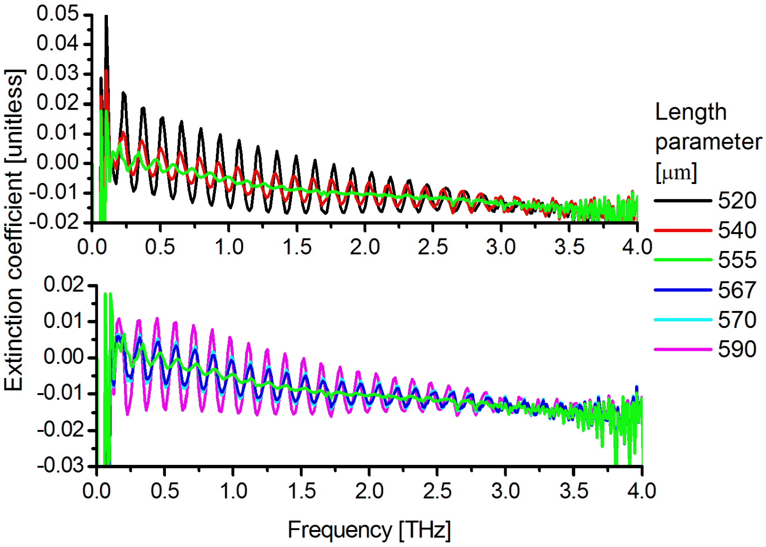

Figure 3.11: Extinction coefficient of fused silica with thickness 567 μm extracted with different length parameters using the infinite reflection transfer function. The extinction coefficient (green) using the 555 μm length parameter shows the optimum extraction. The extinction coeffficient (blue) using the measured thickness of 567 μm is also shown.

The magnitude of the oscillation amplitudes is much larger than any change in the average extinction coefficient due to the transmission component of the theoretical transfer function. The magnitude of the oscillations is the same as those found in the refractive index and appear larger than in the refractive index because the relative size of the extinction coefficient is smaller than the refractive index. The magnitude of oscillation amplitudes are dependent on the mismatch between the length parameter and optimum length parameter, the 567 μm fused silica sample is presented with the largest mismatch hence the oscillations are greatest. The 2054 μm fused silica sample has the smallest oscillations and due to the smaller scale used for the extinction coefficient the frequency dependent curvature of the extinction coefficient is more noticeable.

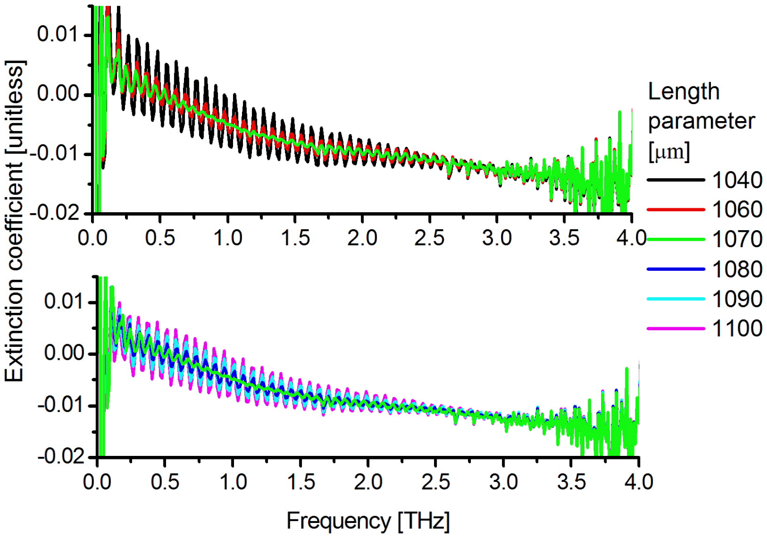

Figure 3.12: Extinction coefficient of fused silica with thickness 1090 μm extracted with different length parameters using the infinite reflection transfer function. The extinction coefficient (green) using the 1070 μm length parameter shows the optimum extraction. The extinction coeffficient (cyan) using the measured thickness of 1090 μm is also shown.

The extinction coefficient of each fused silica sample decreases with frequency, this implies an increasing amount absorption with frequency which is consistent with the literature [78, 79]. For each fused silica sample there is a positive extinction coefficient at frequencies less than 0.5 THz, this suggests amplification at those frequencies and is likely an artifact of the extraction process.

The results from the extinction coefficient suggest the same conclusions that were made with the refractive index. Provided there are no experimental errors due to the THz spectrometer or data acquisition then the actual thicknesses of the fused silica samples are the optimum length parameters which were 555 μm, 1070 μm and 2010 μm. This is because the optimum

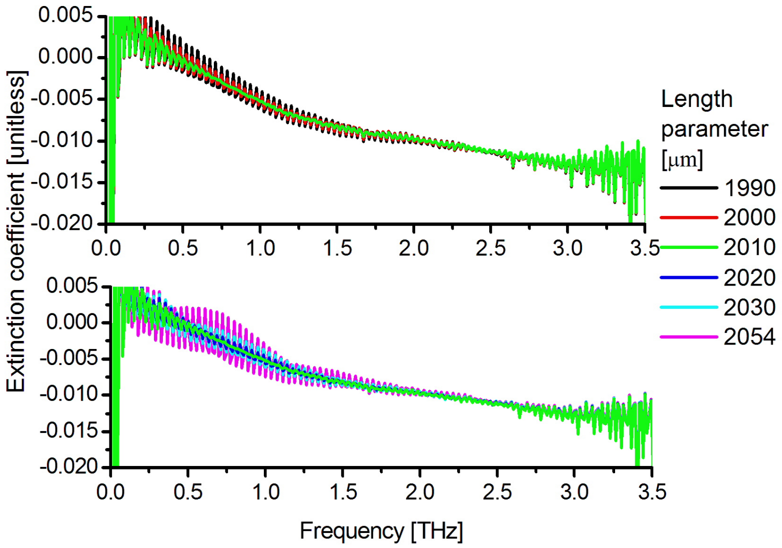

Figure 3.13: Extinction coefficient of fused silica with thickness 2054 μm extracted with different length parameters using the infinite reflection transfer function. The extinction coefficient using the 2010 μm length parameter (green) shows the optimum extraction. The extinction coeffficient (magenta) using the measured thickness of 2054 μm is also shown.

length parameter displays smaller oscillation amplitudes in complex refractive index than an extraction of the complex refractive index using the measured sample thickness which is indicative of a close agreement between Fresnel model and experimental data. In each case the optimum length parameter is smaller than the measured thickness, overestimating the sample thickness underestimates the refractive index and absorption per unit length of material so that the phase and total absorption of the experimental data is maintained.

The optimum length parameters of the 567 μm, 1090 μm and 2054 μm fused silica samples were approximately 2% smaller than their respective measured thicknesses. The consistency in this error between different sample datum taken from the same THz apparatus suggests the presence of a systematic error in the THz time domain scans. Assuming that the measured thicknesses are correct then an explanation for this could be a systematic error in the step size of the delay stage, this would produce indistinguishable errors from thickness errors and this is discussed in section 3.5. In cases where the optimum length parameter is larger than the measured thickness of the sample other systematic errors which would produce the effect of a larger thickness can be considered. A sample surface that experiences non-normal incidence of the THz beam will introduce a longer propagation length for the THz pulse through the sample and increase the apparent thickness in the THz time domain scans. A converging beam would also introduce a longer propagation length through the sample than a collimated beam which would make the sample effectively thicker. The comparison between planewave, sample orientation and converging beam Fresnel models is discussed in chapter 4.

3.3 Number of reflections

A sample placed within the THz beam will produce reflections at the sample interfaces, these reflections appear on the time domain scans as satellite pulses at set intervals with diminishing amplitudes after the main THz pulse which can be observed in fig. 3.14. The interval and amplitudes are dependent on the complex refractive index of the sample, therefore to benefit from this experimental data it is important to account for these reflections in the Fresnel model. If the sample has a refractive index close to the surrounding medium then the reflection coefficients are going to be small and in some cases can be ignored, if however there is a large difference between the refractive indices then reflections should be included. Furthermore, a delay line only allows for a finite time window of the THz time domain scan to be measured which will result in some of the reflections occurring beyond the time domain scan. Modeling the optimum number of reflections required for the theoretical transfer function is dependent on the sample being used and the length of the data set used for the extraction. There is also a necessity to use the entire time domain scan which includes the maximum number of possible reflections in order to maximise the frequency resolution of the extracted complex refractive index.

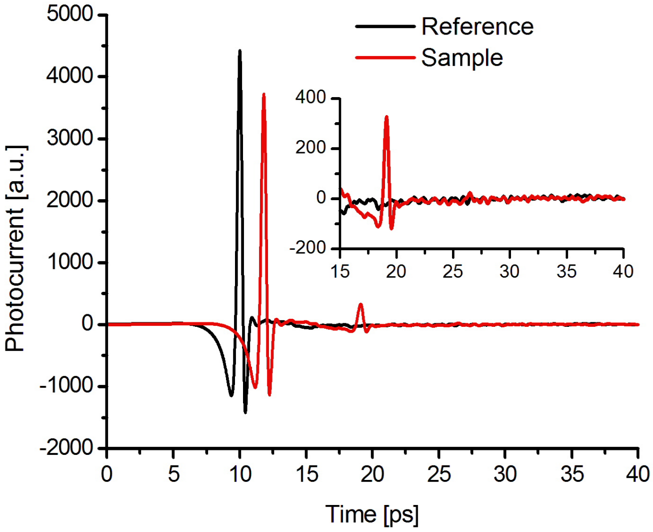

Figure 3.14: THz scans of a reference scan and 567 μm fused silica sample scan. The inset figure shows the reflected THz pulse which have been magnified.

In this section I will investigate the effect that the number of reflections, k, in the theoretical transfer function of eq. 2.15 has on the extracted complex refractive index. I will first define the transfer functions for zero, one and infinite numbers of reflections and then simulate sample scans using the defined transfer functions to check the number of reflections present. I will then perform material parameter extraction on experimental data with transfer functions using different numbers of reflections to determine the optimum number of reflections required for the experimental data. Finally I will change the number of reflections within the experimental data to observe how this affects the extraction using transfer functions with different numbers of reflections.

3.3.1 Transfer functions for different number of reflections

The theoretical transfer function for k number of reflections was derived in section 2.3 and is given by,

$$H(\omega) = \frac{T_{01}(\omega) \cdot P_1(\omega, L) \cdot T_{10}(\omega)}{P_0(\omega, L)} \cdot \sum_{k=0}^{+\infty} \left\{ R_{10}(\omega) \cdot P_1(\omega, L) \cdot R_{10}(\omega) \cdot P_1(\omega, L) \right\}^k . \tag{3.10}$$

This is the transfer function for a single slab of material, it can be adapted to include any number of reflections by changing k to match the number of reflections present in the THz time domain scan. I have derived the transfer functions with zero, one and infinite reflections below.

Zero reflection transfer function

The theoretical transfer function for zero reflections is eq. 3.10 with $k = 0$, this leaves only the transmission components of the transfer function.

$$H_{zero}(\omega) = \frac{T_{01}(\omega) \cdot P_1(\omega, L) \cdot T_{10}(\omega)}{P_0(\omega, L)}. \tag{3.11}$$

The explicit equation used for the fitting process is the natural logarithm of eq. 3.11,

$$G_{zero}(\omega) = \ln\left(\frac{4\tilde{n}_0\tilde{n}_1}{(\tilde{n}_0 + \tilde{n}_1)^2}\right) - \frac{i\omega L}{c}(\tilde{n}_1 - \tilde{n}_0). \tag{3.12}$$

The derivative of eq. 3.12 with respect to $\tilde{n}_1$ is required for the Newton-Raphson method used for the fitting process,

$$G'_{zero}(\omega) = \frac{1}{\tilde{n}_1} - \frac{2}{\tilde{n}_0 + \tilde{n}_1} - \frac{i\omega L}{c}. \tag{3.13}$$

The zero reflection transfer function is required to investigate the effects that the transmission components have on the extracted complex refractive index or on THz time domain data where there are either negligible or no reflections.

One reflection transfer function

The theoretical transfer function for one reflection is eq. 3.10 with $k = 1$, this includes the Fresnel reflections terms to the first order and would be used if the experimental data were to include only one reflection.

$$H_{one}(\omega) = \frac{T_{01}(\omega) \cdot P_1(\omega, L) \cdot T_{10}(\omega)}{P_0(\omega, L)} \cdot (1 + R_{10}(\omega) \cdot P_1(\omega, L) \cdot R_{10}(\omega) \cdot P_1(\omega, L)). \tag{3.14}$$

The explicit equation used for the fitting process is the natural logarithm of eq. 3.14,

$$G_{one}(\omega) = \ln\left(\frac{4\tilde{n}_0\tilde{n}_1}{(\tilde{n}_0 + \tilde{n}_1)^2}\right) - \frac{i\omega L}{c}(\tilde{n}_1 - \tilde{n}_0) + \ln\left(1 + \left(\frac{\tilde{n}_1 - \tilde{n}_0}{\tilde{n}_1 + \tilde{n}_0}\right)^2 e^{-2i\tilde{n}_1\omega L/c}\right). \tag{3.15}$$

The derivative of eq. 3.15 with respect to $\tilde{n}_1$ is

$$G'_{one}(\omega) = \frac{1}{\tilde{n}_1} - \frac{2}{\tilde{n}_0 + \tilde{n}_1} - \frac{i\omega L}{c} + \left(\frac{2\left(\frac{\tilde{n}_1 - \tilde{n}_0}{\tilde{n}_1 + \tilde{n}_0}\right)^2 e^{-2i\tilde{n}_1\omega L/c}}{1 + \left(\frac{\tilde{n}_1 - \tilde{n}_0}{\tilde{n}_1 + \tilde{n}_0}\right)^2 e^{-2i\tilde{n}_1\omega L/c}}\right) \cdot \left(\frac{1}{\tilde{n}_1 - \tilde{n}_0} - \frac{1}{\tilde{n}_1 + \tilde{n}_0} - \frac{i\omega L}{c}\right). \tag{3.16}$$

Infinite reflection transfer function

In some cases the reflections are too close to the main pulse and the signal amplitude does not drop to zero so it is not possible to remove the reflections using truncation without introducing artifacts in the extraction, in which case a transfer function which contains an infinite number of reflections is the optimum solution. The theoretical transfer function for infinite reflections is eq. 3.10 with $k = \infty$, in this case the reflection terms can be treated as an infinite geometric series such that

$$\sum_{k=0}^{+\infty} \{R_{10}(\omega) \cdot P_1(\omega, L) \cdot R_{10}(\omega) \cdot P_1(\omega, L)\}^{+\infty} = \frac{1}{1 - R_{10}(\omega) \cdot P_1(\omega, L) \cdot R_{10}(\omega) \cdot P_1(\omega, L)}. \tag{3.17}$$

This simplifies the infinite reflection transfer function to

$$H_{inf}(\omega) = \frac{T_{01}(\omega) \cdot P_1(\omega, L) \cdot T_{10}(\omega)}{P_0(\omega, L)} \cdot \frac{1}{1 - R_{10}(\omega) \cdot P_1(\omega, L) \cdot R_{10}(\omega) \cdot P_1(\omega, L)}. \tag{3.18}$$

The explicit equation used for the fitting process is the natural logarithm of eq. 3.18 is

$$G_{inf}(\omega) = \ln\left(\frac{4\tilde{n}_0\tilde{n}_1}{(\tilde{n}_0 + \tilde{n}_1)^2}\right) - \frac{i\omega L}{c}(\tilde{n}_1 - \tilde{n}_0) - \ln\left(1 - \left(\frac{\tilde{n}_1 - \tilde{n}_0}{\tilde{n}_1 + \tilde{n}_0}\right)^2 e^{-2i\tilde{n}_1\omega L/c}\right). \tag{3.19}$$

The derivative of eq. 3.19 with respect to $\tilde{n}_1$ is

$$G'_{inf}(\omega) = \frac{1}{\tilde{n}_1} - \frac{2}{\tilde{n}_0 + \tilde{n}_1} - \frac{i\omega L}{c} + \left(\frac{2\left(\frac{\tilde{n}_1 - \tilde{n}_0}{\tilde{n}_1 + \tilde{n}_0}\right)^2 e^{-2i\tilde{n}_1 \omega L/c}}{1 - \left(\frac{\tilde{n}_1 - \tilde{n}_0}{\tilde{n}_1 + \tilde{n}_0}\right)^2 e^{-2i\tilde{n}_1 \omega L/c}} \right) \cdot \left(\frac{1}{\tilde{n}_1 - \tilde{n}_0} - \frac{1}{\tilde{n}_1 + \tilde{n}_0} - \frac{i\omega L}{c} \right). \quad (3.20)$$

The Newton-Raphson method requires the derivative of each transfer function with respect to the complex refractive index of the material, these are shown by equations 3.13, 3.16 and 3.20 for zero, one and infinite reflection transfer functions respectively. The transfer function and derivative for zero reflections is the simplest because it contains only transmission coefficients, the one and the infinite reflection transfer functions are similar except for two minus signs and they also have similar derivatives. As the number of reflections is increased beyond one the transfer function gains an increasing number of reflection terms which makes the analytical solution to the derivative increasingly harder to solve.

3.3.2 Checking the number of reflections using simulated data

To check that the correct number of reflections are produced by their respective transfer function a simulated sample scan was generated using each theoretical transfer function. The theoretical transfer functions for the zero, one and infinite number of reflections were calculated using a sample thickness of 500 μm and complex refractive index of $2.000 - 0.005i$ which is frequency independent. The theoretical transfer functions were then applied to the experimental reference scan shown in fig. 2.1 using eq. 2.3 to produce simulated sample scans.

The simulated transfer function for the differing number of reflections are shown in fig. 3.15, the infinite and one reflection transfer function are on top of each other and show an oscillating function which is due to the Fresnel terms. The zero reflection transfer function contains no Fresnel terms hence there are no oscillations. The simulated sample scans are shown in fig. 3.16, each scan has a main pulse that is delayed from the reference scan pulse with a reduced amplitude. The main pulse on the simulated sample scans are overlapped so it is hard to distinguish between each scan, however the magnified scale in fig. 3.17 shows that the different number of reflections for each transfer function can be observed. The figure shows that the zero reflection transfer function has produced a sample scan with zero reflections, the one reflection transfer function has produced one reflection. The infinite reflection model has produced three observable reflections,

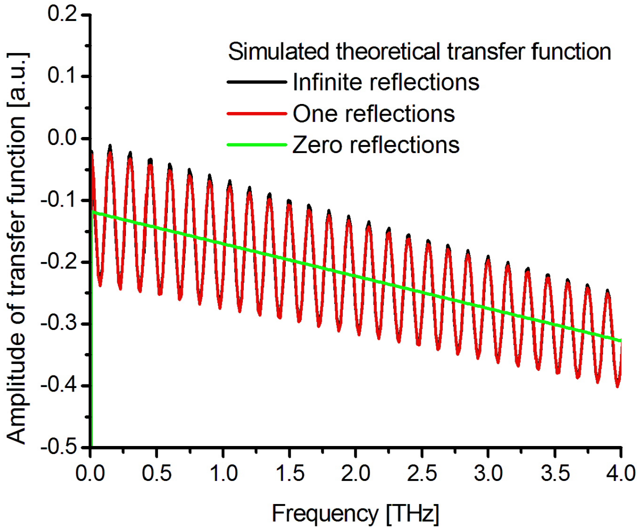

Figure 3.15: The amplitude of simulated theoretical transfer functions for differing numbers of reflections. The sample parameters are a thickness of 500 μm and complex refractive index $2.000 - 0.005i$ which is frequency independent.

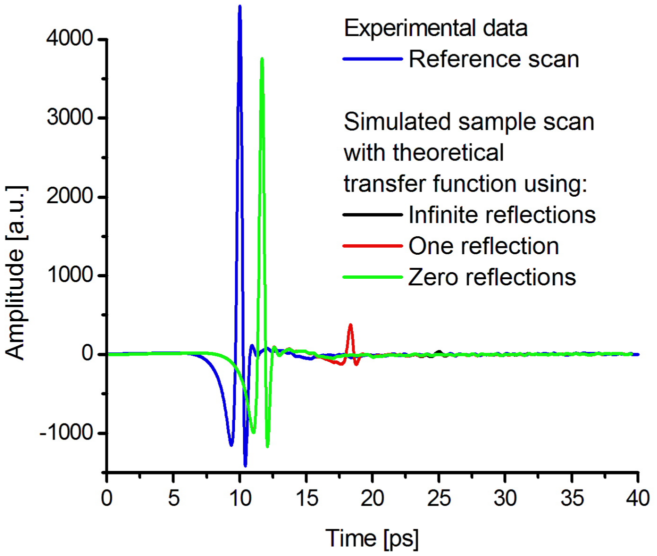

Figure 3.16: Simulated sample scans over the full scan range 0 - 40 ps using transfer functions with differing numbers of reflections. The sample parameters are a thickness of 500 μm and complex refractive index $2.000 - 0.005i$ which is frequency independent.

the first reflection is behind the reflection from the one reflection model, the subsequent reflections are not observable due to diminishing amplitudes. Each theoretical transfer function has been shown to model the correct number of reflections.

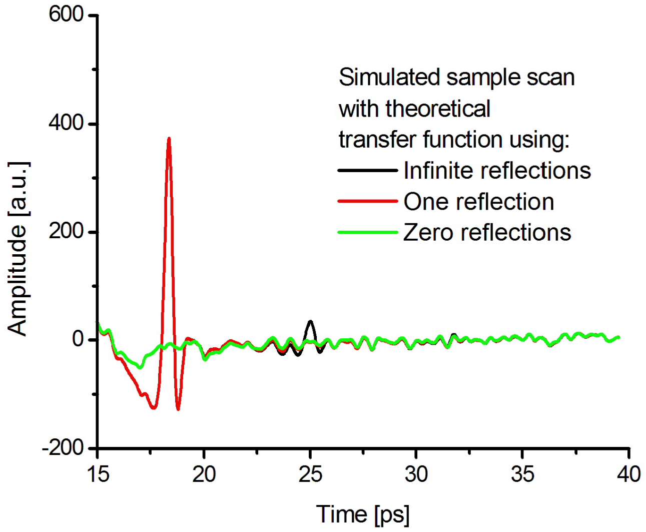

Figure 3.17: Simulated sample scans using transfer functions with differing numbers of reflections that has been magnified to clearly observed the reflections. The sample parameters are a thickness of 500 μm and complex refractive index $2.000 - 0.005i$ which is frequency independent.

3.3.3 Extraction with a different number of reflections on real data

To demonstrate how the extracted complex refractive index is affected by the number of reflections in the theoretical transfer function in comparison to the number of reflections present in the experimental data the complex refractive index of a 567 μm fused silica sample was extracted using the theoretical transfer functions with different numbers of reflections.

The THz scans for the 567 μm fused silica sample is shown in fig. 3.18, the length of the scan is 40 ps, this is long enough to accommodate at least three reflections however only two reflections are visible above the zero level which can be seen from the inset of fig. 3.18. The length parameter used in the extraction was the optimum length parameter of 555 μm which was determined in section 3.2.

Figures 3.19 and 3.20 show the refractive index and extinction coefficient respectively which

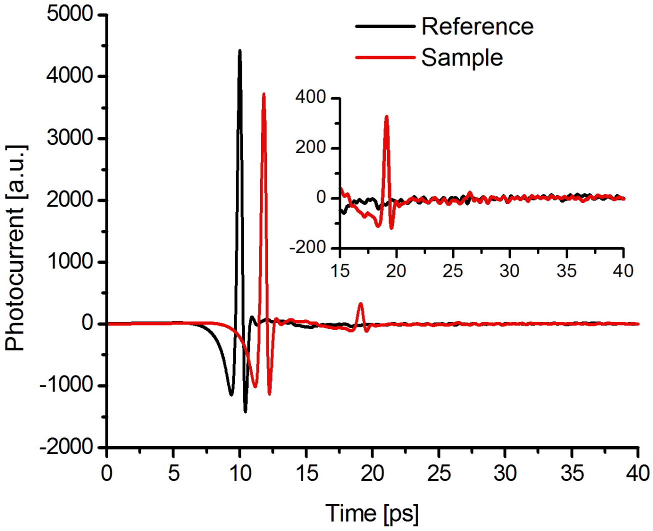

Figure 3.18: THz scans of a reference scan and 567 μm fused silica sample scan. The inset figure shows the reflected THz pulse which have been magnified.

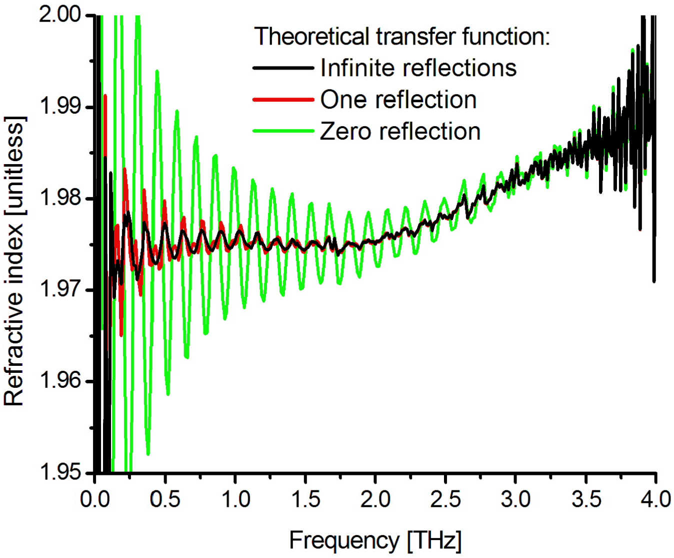

Figure 3.19: Refractive index extraction for different transfer functions including zero reflections, one reflection and infinite reflections.

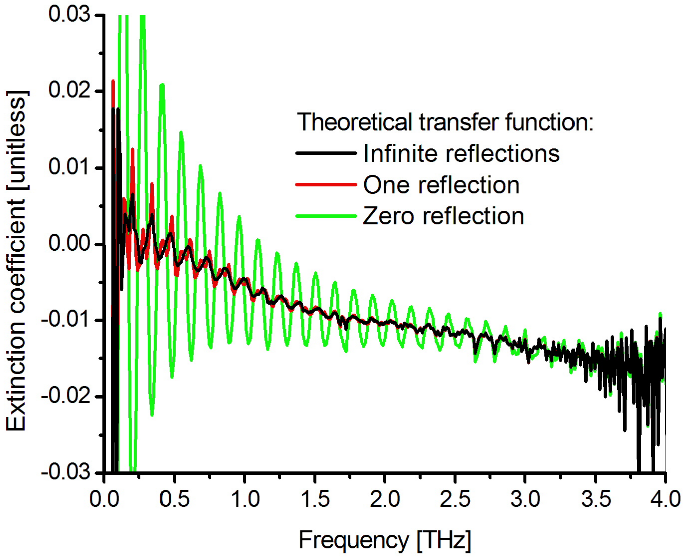

Figure 3.20: Extinction coefficient extraction for different transfer functions including zero reflections, one reflection and infinite reflections.

were extracted using the zero, one and infinite reflection transfer functions. The amplitude of the oscillations for the refractive index and extinction coefficient are shown in table 3.1 for 500 GHz and 1 THz, the relative size of the oscillations between the refractive index and extinction coefficient are the same at each frequency for each transfer function.

Oscillation amplitude of complex refractive index				
	Refractive index		Extinction coefficient	
Reflections	500 GHz	1 THz	500 GHz	1 THz
Zero	0.034±0.001	0.016±0.001	0.033±0.001	0.016±0.001
One	0.007±0.001	0.003±0.001	0.008±0.001	0.002±0.001
Infinite	0.004±0.001	0.002±0.001	0.004±0.001	0.002±0.001

Table 3.1: The complex refractive index oscillation amplitudes at 500 GHz and 1 THz for the different reflection models in the theoretical transfer function using the optimum length parameter of 555 μm.

Analysis of extracted data

The refractive index and extinction coefficient shown in figures 3.19 and 3.20 respectively show that the zero reflection transfer function has the largest amplitude oscillations, this is because the mismatch between the Fresnel model and data is the greatest. The zero reflection transfer function contains no Fresnel term and therefore cannot model the oscillations that occur on the experimental transfer function and hence oscillations appear on the complex refractive index. The extraction with infinite reflections shows the smallest amplitude oscillations in complex refractive index because the infinite reflection transfer function contains Fresnel terms which model the oscillations found in the experimental transfer function and hence reduce the oscillation amplitudes. The oscillations in the one reflection transfer function are slightly larger than the infinite reflection transfer function because the one reflection model does not accommodate for the second and third reflections in the sample scan which produces a mismatch between the Fresnel model and experimental data.

The amplitude of the oscillations that occur on the complex refractive index decrease with frequency. As shown in eq. 3.2, for a constant absorption the calculated extinction coefficient is inversely proportional to frequency. This is also exhibited in fig. 3.5 where we have extracted for simulated data with a constant extinction coefficient; a mismatch on the extraction of the simulated data gives an increased error with wavelength. Furthermore, in eq. 3.12 the same effect can be seen for the real part of the refractive index. Essentially this shows that in the propagation of the EM wave the phase change and absorption due to refractive index is in wavenumbers.

Analysis of transfer functions

The difference in the transfer function (eq. 3.10) for different numbers of reflections is the final term,

$$F_{refl}(\omega) = \sum_{k=0}^{+\infty} \left\{ R_{10}(\omega) \cdot P_1(\omega, L) \cdot R_{10}(\omega) \cdot P_1(\omega, L) \right\}^k , \tag{3.21}$$

for which the natural logarithm can be written as,

$$\begin{aligned}\ln(F_{refl}(\omega)) = \ln\Bigg(1 + \left(\frac{\tilde{n}_1 - \tilde{n}_0}{\tilde{n}_1 + \tilde{n}_0}\right)^2 e^{-2i\tilde{n}_1\omega L/c} + \left(\frac{\tilde{n}_1 - \tilde{n}_0}{\tilde{n}_1 + \tilde{n}_0}\right)^4 e^{-4i\tilde{n}_1\omega L/c} \\ + \ldots + \left(\frac{\tilde{n}_1 - \tilde{n}_0}{\tilde{n}_1 + \tilde{n}_0}\right)^{2k} e^{-2ki\tilde{n}_1\omega L/c}\Bigg),\end{aligned} \tag{3.22}$$

where k is the number of reflections. With each additional reflection there is an additional reflection factor $e^{-2ki\tilde{n}_1\omega L/c}$, each additional reflection factor allows the theoretical transfer function to model changes in the complex refractive index with increasing frequency resolution. The length of the THz scan determines the extraction resolution which is the frequency resolution at which the complex refractive index is extracted. The free spectral range of the sample which is given by eq. 2.7 determines the frequency of the oscillations on the experimental transfer function. Provided the extraction resolution is high enough then the oscillations due to the etalon will be observed on the experimental transfer function.

As long as the number of reflections in the theoretical transfer function is equal to or larger than the number of reflections in the experimental data then the theoretical transfer function will be sufficient for the extraction. So provided there are reflections in the data the infinite reflection theoretical transfer function will accommodate for any number of reflections that are present in the experimental data. Therefore the infinite reflection transfer function is the optimum transfer function for THz time domain scans that includes one or more reflections.

3.3.4 Modelling the reflections with truncated data

It was previously shown in section 3.3.3 that the amplitude oscillations on the complex refractive index are dependent on the number of reflections used in the theoretical transfer function, here I investigate this further by changing the number of reflections present within the experimental data. Truncation which is also known as apodisation is used to change the number of reflections present within the experimental. I begin by describing the method of truncation because changing the number of reflections within the experimental data requires careful truncation techniques to avoid introducing artifacts onto the extracted complex refractive index.

Method of truncation

The method of truncation used is important as this will affect the extraction, to demonstrate this two different methods of truncation have been used which are applied to the experimental THz time domain scans which were shown in fig. 3.18. The profiles of the two truncation functions are shown in fig. 3.21 with the THz time domain scan of the 567 μm fused silica sample. The two methods of truncation were a sharp cut off where all of the data beyond the cut off point is set to zero and a smooth cut off where the data is gradually set to zero. The smooth truncation is applied by multiplying the THz time domain scan by the function,

$$F(k) = \frac{1}{1 + e^{(k-(k_{peak}+k_{delay}))/A}}, \tag{3.23}$$

where k is the sample number in frequency, k_{peak} is the sample number of the peak for the main THz pulse, k_{delay} is the number of samples from which the truncation is delayed form the main THz pulse and A is a scaling factor which determines how fast the truncation goes to zero. This function enables the truncation to begin at some constant time after the main THz pulse for each THz time domain scan.

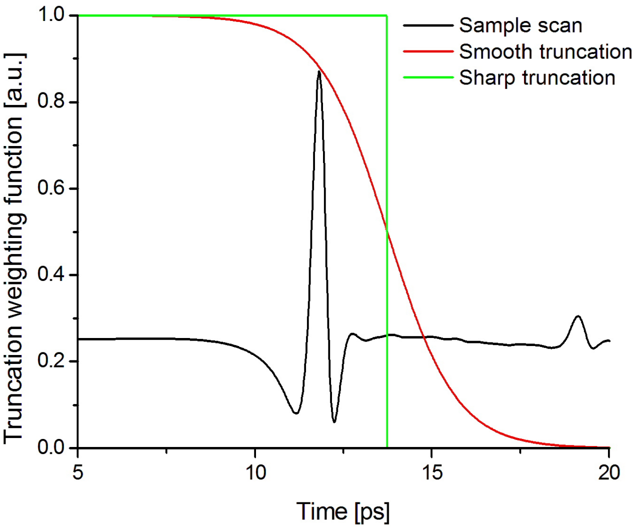

Figure 3.21: Original sample scan with the truncation functions for a sharp and smooth cut off present.

Truncation was applied to the time domain scans for a 567 μm fused silica sample in three different ways to remove all reflections. These were a sharp cut off after some chosen point which is the same for the reference and sample scan, a sharp cut off which is chosen some time after the main pulse of each individual scan and a smooth cut off chosen some time after the main pulse of individual each scan. The data is always padded with zeros beyond the cut off position to the original data length to maintain a consistent frequency resolution between the scans. The complex refractive index for a 567 μm fused silica sample was then extracted using a theoretical transfer function with zero reflections to determine which truncation method is closest to a THz scan with zero reflections, a complex refractive index with zero reflections should contain no oscillations. The optimum length parameter of 555 μm was used for the extraction. The refractive index and extinction coefficient for the different truncation methods are shown in figures 3.22 and 3.23 respectively.

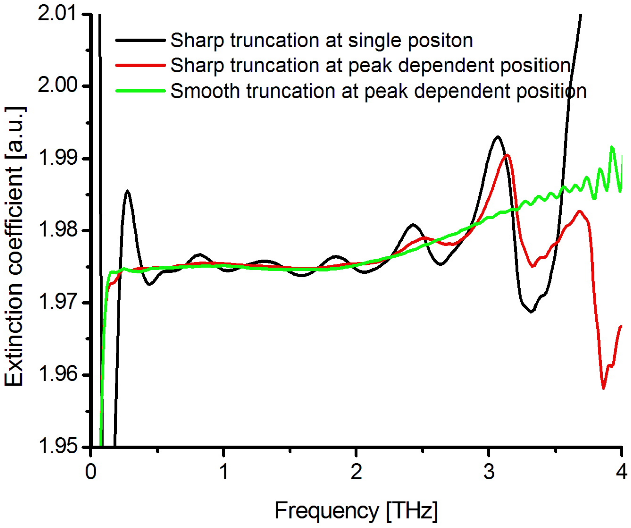

Figure 3.22: Refractive index of 567 μm fused silica extracted using the zero reflection transfer function with three different methods of truncation weighting functions. The optimum length parameter of 555 μm was used for the extraction.

The sharp truncation with a single position which is the same for the reference and sample scan produces the largest oscillations on the complex refractive index, the oscillations are reduced for the sharp truncation with peak dependent position and are smallest when the smooth truncation is used. The peak dependent position for the cut off effectively truncates each scan

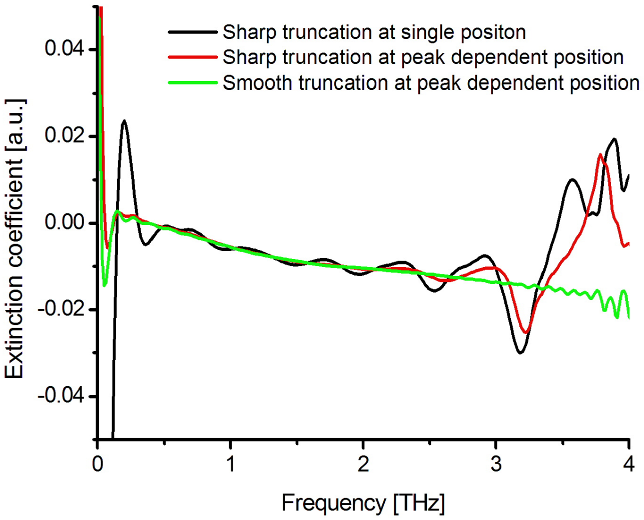

Figure 3.23: Extinction coefficient 567 μm fused silica extracted using the zero reflection transfer function with three different methods of truncation weighting functions. The optimum length parameter of 555 μm was used for the extraction.

with the same delay after the main pulse giving each truncated scan the same scan length. The same scan length is required so that the Fourier transforms produce THz spectra with the same frequency resolution, this is essential for accurate material parameter extraction and the reason why the peak dependent cut off is better than the single position cut off. The sharp cut off produces oscillations in the complex refractive index because there is a discontinuity at the cut off position which causes the photocurrent to go from a non-zero value to zero, the smooth cut off eliminates this discontinuity and hence produces minimal oscillations and is therefore the optimum truncation method for removing reflections.

Truncated experimental scans

The original THz scans of 567 μm fused silica sample are shown in fig. 3.18, the inset shows the presence of more than one reflection. The truncated scans are shown in fig. 3.24 with the reflections removed, the peak dependent smooth cut off is shown by the dashed lines. The length parameter used in the extraction was the optimum length parameter of 555 μm which was determined in section 3.2. The refractive index and extinction coefficient are shown in fig. 3.25

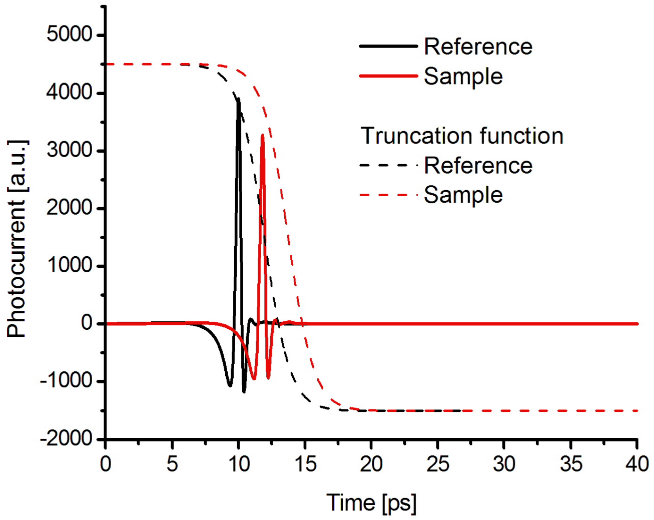

Figure 3.24: THz scans of a reference scan and 567 μm fused silica sample scan which has been truncated so that satellite pulses due to reflections within the sample interfaces in the sample are removed. Smooth cut off truncation functions are used for each scan, these are also shown by the dashed lines. The starting position for each truncation function is dependent on the peak of the main pulse for each individual scan.

and 3.26 respectively, these were extracted with the infinite and zero reflection theoretical transfer functions using truncated and non-truncated data. The extraction with the zero reflection transfer function and truncated data shows no oscillations present on the complex refractive index because the experimental data has zero reflections due to the truncation. The extraction with infinite reflections and non-truncated data shows the next best extraction because the infinite transfer function contains reflections and so does the non-truncated data.

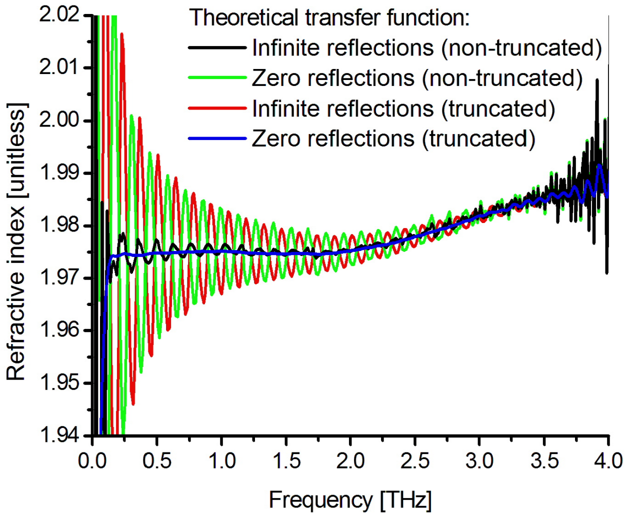

Figure 3.25: Refractive index extraction results for a 567 μm fused silica sample which has been processed with a infinite and zero reflection theoretical transfer functions and with truncated and non-truncated data.

The zero reflection transfer function with non-truncated and infinite reflection transfer function with truncated data each show the largest oscillation amplitudes because in each case there is a mismatch between the Fresnel model and experimental data. It is interesting that their amplitudes are the same and the phase of the oscillations are different by π, this is because the two cases are complete opposites of each other. When extracting non-truncated data with the zero reflection transfer function, the experimental transfer function contains Fresnel oscillations but the theoretical transfer function does not contain Fresnel oscillations. When extracting the truncated data with infinite reflection transfer function, the experimental transfer function contains no Fresnel oscillations but the theoretical transfer function does contain Fresnel oscilla-

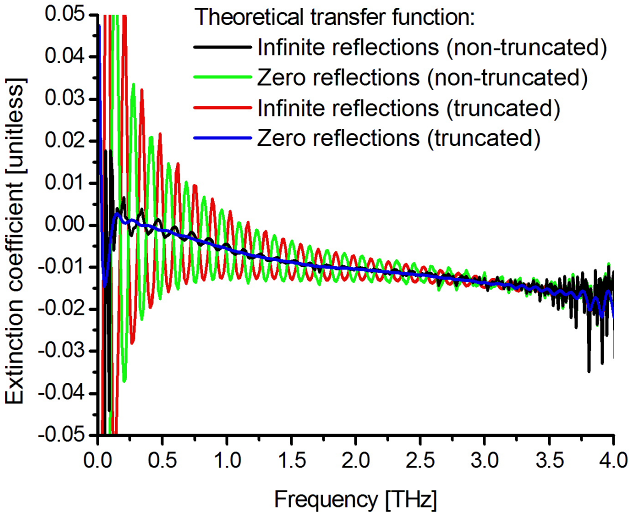

Figure 3.26: Extinction coefficient extraction results for a 567 μm fused silica sample which has been processed with a infinite and zero reflection theoretical transfer functions and with truncated and non-truncated data.

tions. These results confirm that the infinite reflection transfer function is the optimum transfer function for THz time domain scans that includes one or more reflections and the zero reflection transfer function is of course the optimum transfer function if no reflections are present.

3.4 Noise suppression

In material parameter extraction the range of frequencies over which it is possible to investigate a sample is limited by the bandwidth of the THz time domain scan which in turn is dependent on the THz bandwidth produced by the THz spectrometer. The THz emitter and detector generate and detect some finite bandwidth of the THz radiation which is fundamentally limited by noise [102, 103]. The bandwidth of the extracted complex refractive index is limited by the SNR of the experimental transfer function, when the SNR is low the extraction will either fail or be influenced by the perturbations from the noise. This is a limitation when investigating absorption features at regions in the THz spectra where SNR is low or samples that are highly absorbing to THz radiation and produce scans with an insufficient SNR. There are however methods of reducing noise on the THz spectra using signal processing techniques such as Wavelet de-noising [101] and Wiener deconvolution algorithms [104] which can improve the SNR to aid real-time THz imaging and signal recognition. In this section I demonstrate a method of noise suppression which is applied to noisy experimental THz time domain scans to increase the useful spectral bandwidth and reveal spectral features that were difficult to detect beforehand. The method of noise suppression works by using a modified theoretical transfer function to model white noise present on the THz spectra. I begin by detailing the various sources of noise present in a THz spectrometer and then demonstrate the noise suppression method.

3.4.1 Sources of noise

The noise can be random or systematic depending on the source and can be defined as having either a long or short time dependence. Noise fluctuations which occur on the time scales of the entire THz scan are considered long term fluctuations and noise fluctuations that occur on the time scales similar to the time interval of the measurements are considered short term fluctuations. The two main sources of noise in a THz-TDS system occur from fluctuations of the incident intensity on the THz antenna and electronic noise within the THz antenna.

THz antenna

The PCA is susceptible to electronic noise such as thermal and shot noise. The thermal noise of electrons within the photoconductive semiconductor cause random fluctuations of the photocurrent for both the detector and emitter, the random fluctuations in the time domain translates to a constant bias in the frequency domain. Shot noise produces fluctuations in photocurrent due to the quantised charge that an electron carries and is proportional to the photocurrent, the behaviour of shot noise in the frequency domain will be proportional to the amplitude of frequency spectrum. It is also possible for the detector to receive radiation from other sources other than the main THz beam path which can introduce artifacts on the THz scan. This may occur if THz radiation is being scattered off of optical components and is reaching the detector.

Intensity fluctuations

Fluctuations of the optical intensity incident on the PCA can also introduce noise within THz scans. Slowly varying intensity fluctuations can be caused by fluctuations in the laser output power and by mechanical drift of the setup which changes the position or size of the incident spot size. THz spectrometers which use long delay lines or have long data acquisition times are more susceptible to slowly varying laser fluctuations. Slowly varying intensity fluctuations will produce an error on the extracted extinction coefficient, this is because the effective gain of the spectrometer will be inconsistent between scans. Fast varying intensity fluctuations can be caused by mechanical instabilities due to vibrations within the setup, intensity fluctuations have been shown to be comparable random errors in THz-TDS [105]. Fluctuations due to the laser itself can be removed if the laser output is monitored simultaneously when taking a time domain scan.

3.4.2 Modified transfer function for noise suppression

The purpose of the noise suppression is to reduce the amount of noise on the observed signal to improve the result of material parameter extraction. A theoretical transfer function which models the noise using the term $\nu(\omega)$ is used to filter noise present on a the final extraction which can be applied to the experimental transfer function as follows,

$$H(\omega) = \frac{Y(\omega) \cdot X^*(\omega)}{X(\omega) \cdot X^*(\omega) + \nu(\omega)} \tag{3.24}$$

where $X(\omega)$ is the reference spectra, $Y(\omega)$ is the sample spectra and $\nu(\omega)$ is a noise suppression term. This method is a SNR dependent filter which stops the amplification of noise in the sample spectra and is similar to a Wiener filter which is an adaptive finite impulse response filter. When the signal is small on reference spectra and there is noise on the sample spectra the conventional transfer function $H(\omega) = Y(\omega)/X(\omega)$ is susceptible to amplify that noise. The modified transfer function in eq. 3.24 prevents this by having a noise suppression term so that when the signal is small in the reference spectra there is always a term in the denominator that remains, this reduces any amplification of noise from the sample spectra.

3.4.3 Noise suppression applied to experimental data

The noise suppression transfer function was applied to noisy THz scans of 4 mm silicon which were acquired in a humid atmosphere to test the noise suppression. The THz scans for the reference and sample scan are shown in fig. 3.27 which were taken at the University of Southampton with

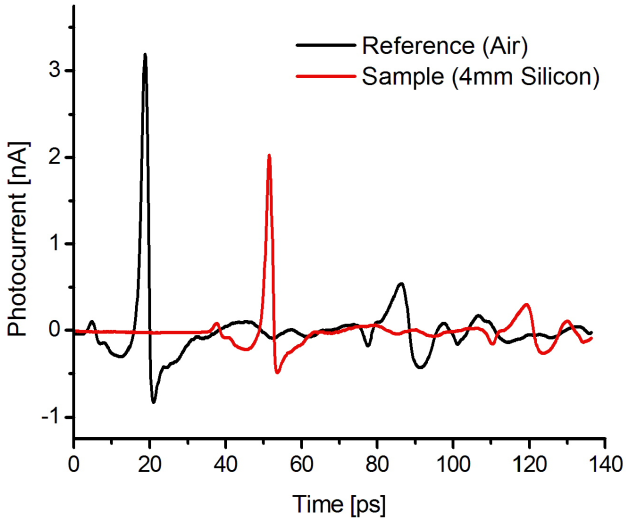

Figure 3.27: THz time domain scan of 4 mm silicon and a reference scan which was acquired in a humid atmosphere at the University of Southampton.

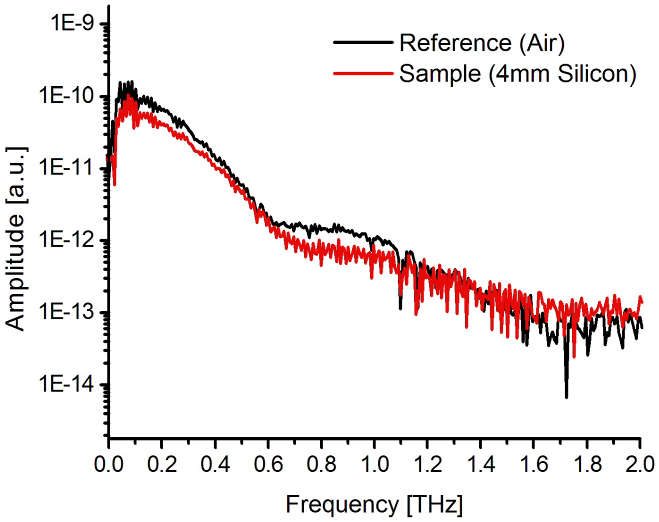

Figure 3.28: Noisy THz spectra of 4 mm silicon and reference scan which are not noise suppressed.

a THz spectrometer that used PCA for both the emitter and detector. The THz spectra of the scans are shown in fig. 3.28, THz spectra have a frequency resolution of 7.3 GHz, the dynamic range is 34 dB and the noise floor occurs at approximately 1.6 THz. The spectra contains absorption lines due to water vapour, the relative humidity as measured by the hygrometer in the vicinity of the THz spectrometer was 39%. The noise of the spectrometer was modelled as white noise which is a stochastic random variation in the time domain and represented as the constant value ν in the frequency domain. The effect of the noise suppression on the impulse response is shown in fig. 3.29, as the noise term is increased the noise from the impulse response is removed.

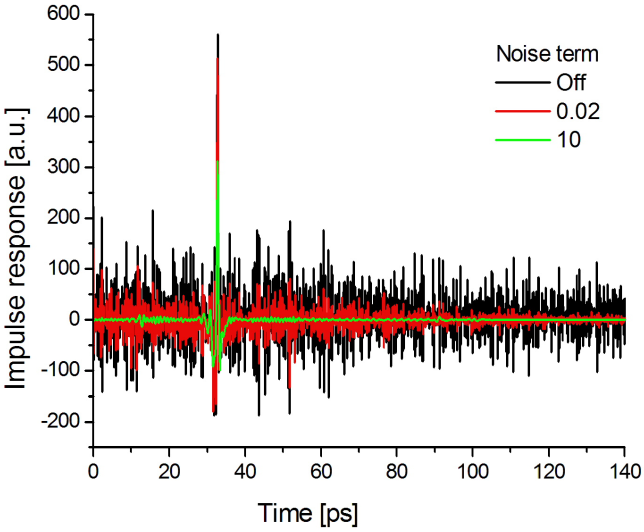

Figure 3.29: Impulse response of 4 mm silicon which was aquired in a humid atmosphere using different amounts of noise suppression.

The improvement on the extracted refractive index and extinction coefficient due to the noise suppression are shown in figures 3.30 and 3.31 respectively. The extinction coefficient shows two levels of noise suppression, when the noise term is set to 10 there are spectral features which can not be observed with a noise term of 0.02. These spectral lines correspond to rotational modes of water in the gas phase [106, 107] which was present in the column of air that was unoccupied by the sample in the reference scan. The water absorption was not modelled in the theoretical transfer function so they appear in the final extraction. The same absorption lines are seen in

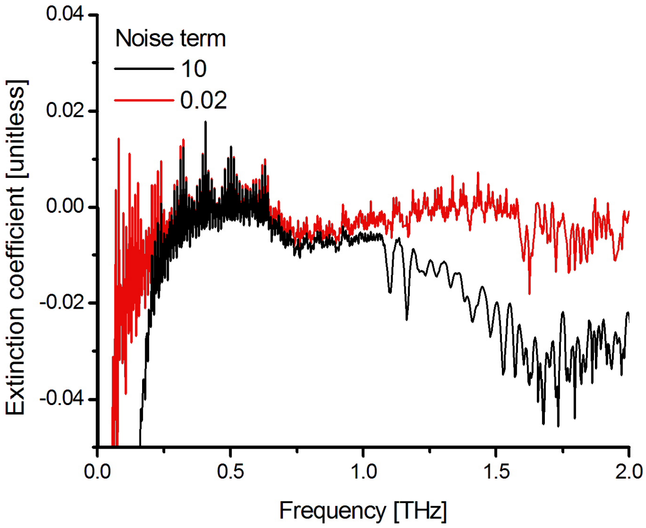

Figure 3.30: Refractive index extracted using different amounts noise suppression for 4mm silicon in a humid atmosphere.

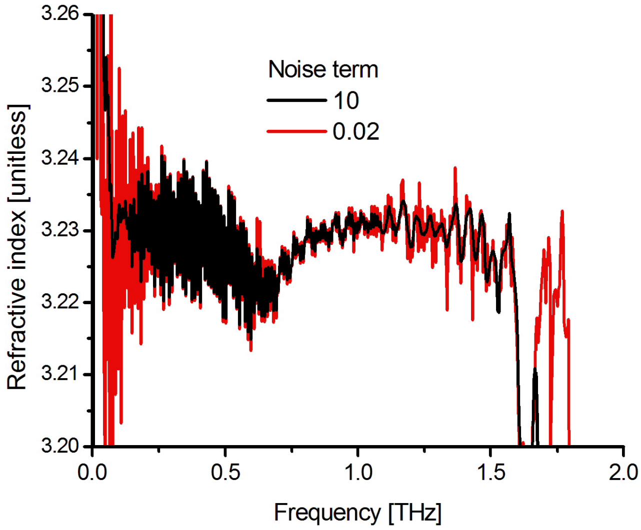

Figure 3.31: Extinction coefficient extracted using different amounts noise suppression for 4mm silicon in a humid atmosphere.

the refractive index, they are less pronounced because the relative magnitude of the refractive index compared to the magnitude of the absorption lines is larger than that of the extinction coefficient.

The SNR dependence of the noise suppression can be seen by the varying smoothness of the complex refractive index with frequency. At frequencies below 1.0 THz the SNR is sufficient that the filter has minimal effect that the complex refractive index oscillates, beyond 1.0 THz the SNR is small enough for noise suppression and the complex refractive index becomes smooth. An artifact of the noise suppression is that there is a bias applied to the complex refractive index, this is because a constant noise term is used and it is fixed for the reference spectra but not the sample spectra which is a limitation of the noise suppression method in its current form.

The advantage of this noise suppression method is that it can be used to reveal spectral features where the SNR is low which would otherwise be hidden using standard material parameter extraction methods, noise suppression effectively increases the useful bandwidth of the THz-TDS system. Finding an accurate frequency dependent model for the noise to use on the noise suppression term $\nu(\omega)$ would improve this technique. It is difficult to know the exact behaviour of noise and to be able to quantify noise exactly due to the various sources that were discussed in section 3.4.1 without further experiments. Ideally one would want to characterise deterministic noise of the THz system and actively measure the random noise with each scan. For example a beam splitter could be used to pick off part of the ultrafast laser beam to measure the fluctuations, the THz time domain scan could then be corrected according to the level of fluctuations. The lock-in amplifier has the capability to measure the noise on the photocurrent, this measurement could be used to characterise the noise on the THz system which would lead to a more accurate noise model and more effective noise suppression.

3.5 Deficiencies in Transfer Function

Throughout this chapter various effects have been investigated which show imperfections in the extraction process, the most dominant effect observed due to these imperfections is the presence of etalon oscillations in the complex refractive index. The imperfections appear larger in the extinction coefficient than the refractive index because the relative size of the extinction coefficient is smaller than the refractive index, in fact the relative size of oscillations in the extinction coefficient and the refractive index are the same as shown in table 3.1. The complex refractive index of a sample is determined by fitting the theoretical transfer function to the observed values in the experimental transfer function. The fit is actually made to the logarithm of the transfer function (eq. 2.15) and for a slab of material of thickness L with complex refractive index $\tilde{n}$ embedded in material of complex refractive index $\tilde{n}_0$. The logarithm of the transfer function is

$$G = \ln(T_0) - i\omega(\tilde{n} - \tilde{n}_0)L/c - \ln(1 - R^2 e^{-2i\tilde{n}\omega L/c}) \tag{3.25}$$

where

$$T_0 = \frac{4\tilde{n}\tilde{n}_0}{(\tilde{n} + \tilde{n}_0)^2} \tag{3.26}$$

is the transmission coefficient of two interfaces and

$$R = \frac{\tilde{n} - \tilde{n}_0}{\tilde{n} + \tilde{n}_0} \tag{3.27}$$

is the internal reflection coefficient of the slab. In the process of material parameter extraction the equation $G_{theo}(\tilde{n}_0, \tilde{n}, \omega, L) = G_{exp}(\omega)$ is solved for $\tilde{n}$ using the value of $G_{exp}(\omega) = \ln(H_{exp}(\omega))$ computed from the data and assumed values of $\tilde{n}_0$ and L. It is difficult using this expression to see the effect on $\tilde{n}$ of small changes in $G_{theo}(\omega)$ so let us make the approximation that R^2 is small. If, for example, $\tilde{n} = 2$ and $\tilde{n}_0 = 1$ which is similar to the complex refractive index of a fused silica sample in a nitrogen atmosphere, then $R^2 \simeq 0.1$, so this is not unreasonable. Then we can write

$$G \simeq \ln(T_0) - i\omega(\tilde{n} - \tilde{n}_0)L/c + R^2 e^{-2i\tilde{n}\omega L/c} \tag{3.28}$$

Differentiating with respect to $\tilde{n}$ gives

$$\frac{dG}{d\tilde{n}} \simeq (\ln(T_0))' - i\omega L/c + \left[(R^2)' - R^2 i\omega L/c\right] e^{-2i\tilde{n}\omega L/c} \tag{3.29}$$

If we assume that T_0 and R vary slowly with $\tilde{n}$ in comparison to the exponential and the sample thickness is at least several wavelengths so that $\omega L/c \gg 1$ we get the approximate result,

$$\delta G \simeq \frac{-i\omega L}{c}(1 + 2R^2 e^{-2i\tilde{n}\omega L/c})\delta\tilde{n} \tag{3.30}$$

$$\delta\tilde{n} \simeq \frac{ic}{\omega L}(1 - 2R^2 e^{-2i\tilde{n}\omega L/c})\delta G \tag{3.31}$$

The conclusion to be drawn from this is that unless δG specifically cancels the factor $(1 - R^2 e^{-2i\tilde{n}\omega L/c})$ etalon oscillations in complex refractive index are inevitable. We now examine various particular models for δG to see if their effects on $\tilde{n}$ can be identified. We examine

- Time offset between sample data and reference data.
- Phase extrapolation to zero frequency wrong.
- Gain change between sample and reference.
- Sampling interval specified wrongly.
- Thickness of sample wrong.
- Sample not oriented perpendicular to terahertz beam.
- Sampling interval different in sample and reference data.

These effects listed above are incorporated into the equations δG to predict $\tilde{n}$ which for some effects can be compared with that computed from the data. In the following x and y refer to the ideal reference and sample data and x' and y' to the values that are actually measured. The notation $x(t)$, for example, will imply that t is a continuous time variable and a subscript t will imply a sample value with t as an integer.

3.5.1 Time offset between sample and reference data

The time offset between sample and reference data is synonymous with errors in the delay stage position. Should the delay stage not return to the original position between scans or an integer of the step size then a time offset between the sample and reference scan will occur. We will take the reference time values as correct so $x'(t) = x(t)$ and $y'(t) = y(t + \delta t)$. The corresponding spectra will be related by

$$Y'(f) = Y(f)e^{2\pi i f \delta t} \tag{3.32}$$

and so

$$H'(f) = H(f)e^{2\pi i f\delta t} = He^{2\pi i f\delta t} \tag{3.33}$$

and therefore $G' = G + 2\pi i f\delta t$. It follows that $\delta G = 2\pi i f\delta t$. Substituting this into eq. 3.31 derived in the first section

$$\delta\tilde{n} \simeq \frac{ic}{\omega L}(1 - 2R^2 e^{-2i\tilde{n}\omega L/c})\delta G \tag{3.34}$$

and noting that $\omega = 2\pi f$ gives

$$\delta\tilde{n} \simeq \frac{c\delta t}{L}(1 - 2R^2 e^{-2i\tilde{n}\omega L/c}) \tag{3.35}$$

and

$$\delta G \simeq \frac{-i\omega\delta t}{c} \tag{3.36}$$

The important thing to note here is that in eq. 3.34 the factor ω cancels so that the shift and amplitude of the oscillations in $\tilde{n}$ is independent of frequency albeit the exponential decay. The effect on transfer function due to the time offset is shown by eq. 3.36, it will be purely a change in the phase which is linear with angular frequency. It is shown by eq. 3.35 that the effect of a time offset between the sample and reference data will produce a shift in the refractive index and produce constant oscillations in both the real and imaginary part of the complex refractive index.

To compare the analytical effects concluded by equations 3.35 and 3.36 a time offset was applied to a simulated sample scan, the complex refractive index was extracted and the experimental transfer function determined. The simulated sample scan was generated from the experimental reference scan shown in fig. 2.1 using the infinite reflection transfer function. A complex refractive index of $\tilde{n} = 2.000 - 0.005i$ and sample thickness of 500 μm was used, the sample scans were also delayed with time offsets of 193 fs and 386 fs. The original reference scan and simulated sample scans can be seen in fig. 3.32. It is shown in fig. 3.33 that the effect of the time offset on the phase of the experimental transfer function is a linear with frequency as predicted by eq. 3.36. There appear to be some small differences in the amplitude of the transfer function at high frequencies where the SNR is low as shown in fig. 3.34, however the dominant effects on the experimental transfer function are purely imaginary.

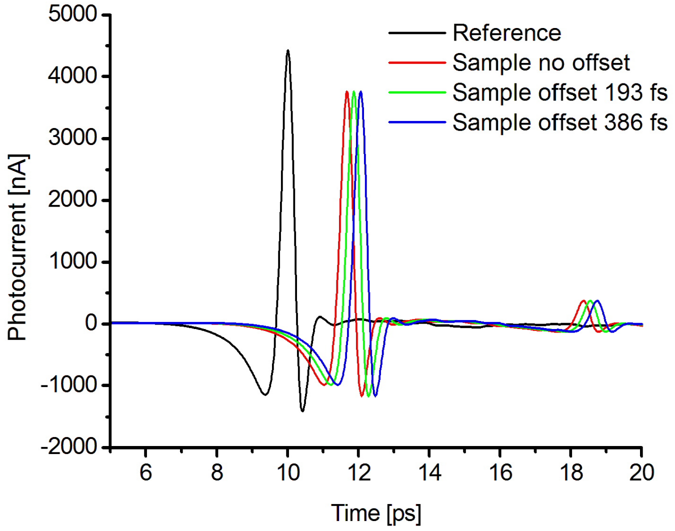

Figure 3.32: Reference scan and simulated sample scan with artificial time delays from the original position, 193 fs and 386 fs.

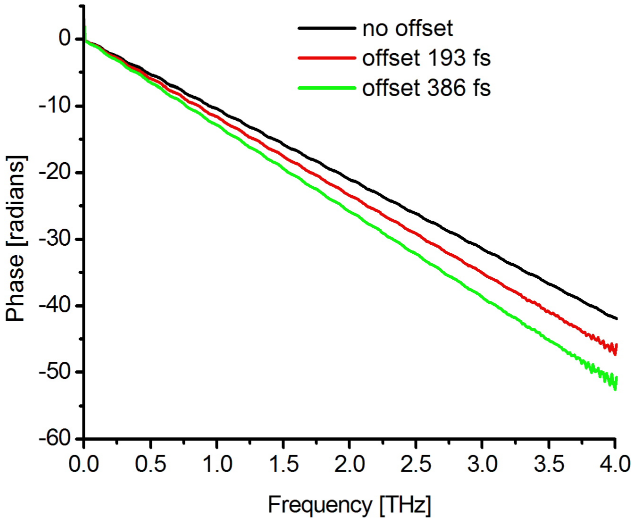

Figure 3.33: Phase of the experimental transfer functions with the time offsets 193 fs and 386 fs between the simulated sample and reference scan.

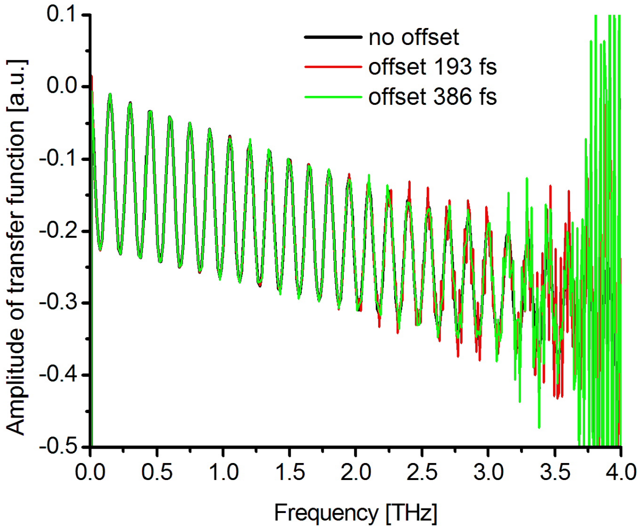

Figure 3.34: Amplitude of transfer functions with the time offsets 193 fs and 386 fs between the simulated sample and reference scan.

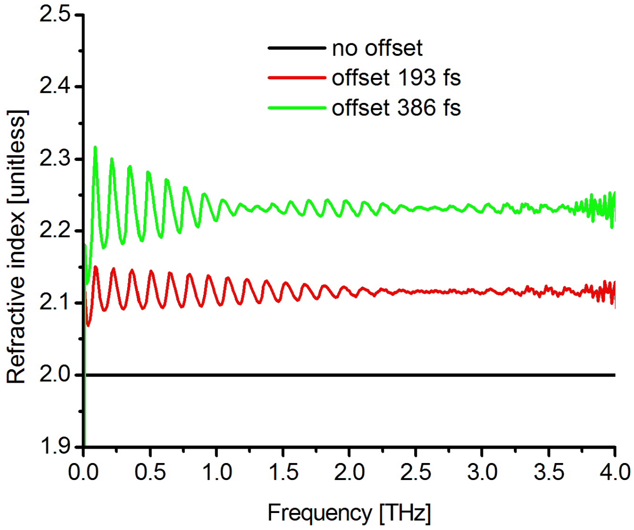

Figure 3.35: Refractive index extracted for a simulated sample scan which has a time offsets 193 fs and 386 fs between the simulated sample and reference scan.

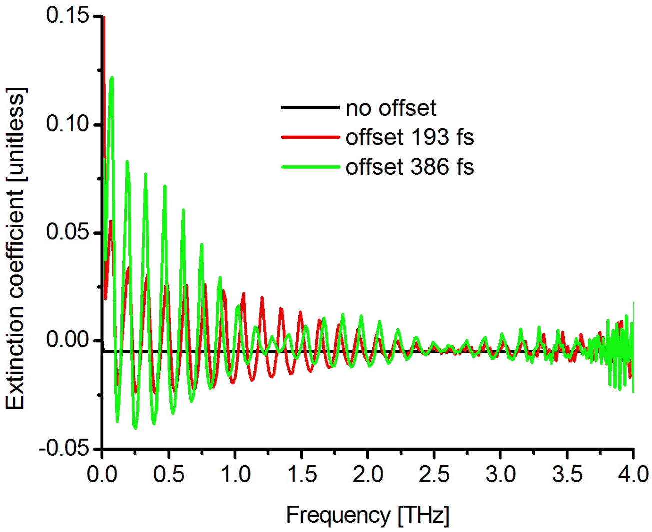

Figure 3.36: Extinction coefficient extracted for a simulated sample scan which has a time offsets 193 fs and 386 fs between the simulated sample and reference scan.

The extracted refractive index is shown in fig. 3.35, there is indeed a shift in the real part of the complex refractive index that is proportional to the time offset. There are also amplitude oscillations that are not simply an exponential decay as there is frequency beating, this is also observed in the extinction coefficient shown in fig. 3.36. The frequency beating on the complex refractive index was not predicted by equations 3.35 and 3.36 due to the approximation made earlier that R varies slowly with $\tilde{n}$. In particular if the term $(R^2)'$ in eq. 3.29 was considered then the change in the complex refractive index $\delta\tilde{n}$ would be an additional exponential term that was frequency dependent which would account for the frequency beating. The time interval between data points of the THz scans is 19.3 fs, the time offsets of 193 fs and 386 fs corresponds to an error of 10 and 20 time intervals. The change in the average refractive indices for the time offset of 10 and 20 time intervals are 2.12 and 2.23 respectively, therefore for every time offset error of 19.3 fs the average refractive index would change by 0.012 for a sample of refractive index 2.0 and thickness 500 μm.

3.5.2 Phase extrapolation wrong or Gain change

If there is low SNR of the THz scans then the phase extrapolation process could give the wrong phase, the phase extrapolation process is described in section 2.5. If the conditions of the THz setup change between scans then it is possible that the gain between scans is different, this can occur due to mechanical instabilities within the setup or large intensity fluctuations of the laser. It is convenient to deal with these effects together as they lead to the equation

$$H'_k = Ae^{i\psi}H_k \tag{3.37}$$

or

$$G'_k = G_k + \ln(A) + i\psi \tag{3.38}$$

where A and ψ is the incorrect gain and phase offset of the experimental transfer function respectively. This leads to $\delta G = \ln(A) + i\psi$ which is substituted into eq. 3.31 giving a change in complex refractive index,

$$\delta\tilde{n} \simeq \frac{(i\ln(A) - \psi)c}{\omega L}(1 - 2R^2e^{-2i\tilde{n}\omega L/c}) \tag{3.39}$$

and a change in transfer function is given by,

$$\delta G \simeq (\ln(A) + i\psi)(1 - 2R^2e^{-2i\tilde{n}\omega L/c}) \tag{3.40}$$

The effect of a phase offset on G is purely imaginary and independent of frequency. The effect of phase offset on $\tilde{n}$ is a shift in refractive index and large oscillations especially at low frequency, decreasing at high frequency. The effects of the phase offset were investigated on experimental data in section 2.5.3 where the phase intercept was changed and the complex refractive index extracted. Oscillations were observed on the extinction coefficient and the refractive index and the curvature of the refractive index was dependent on the phase intercept. The effect of gain on G is purely real and also independent of frequency this produces an effect on $\tilde{n}$ which is a shift in absorption and large oscillations especially at low frequency, decreasing at high frequency.

3.5.3 Sampling interval, thickness or orientation wrong

The sampling interval between the data points is determined by the time it takes for the delay stage to complete a scan in conjunction with the sampling rate of the data acquisition, should either of these be specified incorrectly then the sampling interval will be incorrect. The result of an incorrect sampling interval is an incorrect scan length which affects the scan by giving the incorrect time delay between THz pulses in the sample and reference scans. This is analogous to using the incorrect sample thickness which can also be produced by assuming the wrong sample orientation. So again it is convenient to treat these all together because they all affect the transfer function in the same way. The expression for the transfer function of a sample not oriented perpendicular to the terahertz beam is derived in section 4.2.2. The transfer function depends on

$$\frac{2\pi kL\cos(\theta)}{N\Delta t} = k\psi \tag{3.41}$$

where k is sample number in frequency and N the total number of samples. Let ψ and $\tilde{n}$ be the true values of $2\pi L\cos(\theta)/N\Delta t$ and the refractive index, and assume the data is analysed with a wrong value ψ' which produces a wrong refractive index $\tilde{n}'$. The true logarithm of the transfer function is

$$G = \ln(T_0(\tilde{n})) - ik(\tilde{n} - \tilde{n}_0)L + R(\tilde{n})^2 e^{-2ik\tilde{n}L} \tag{3.42}$$

and the formula used for interpretation is

$$G' = \ln(T_0(\tilde{n}')) - ik\tilde{n}'\psi' - ik\tilde{n}_0\psi' + R(\tilde{n}')^2 e^{-2ik\tilde{n}'\psi'} \tag{3.43}$$

By far the biggest terms are those involving $k\psi$ and if we make $\tilde{n}'\psi' = \tilde{n}\psi$ then $G' \simeq G + ik\tilde{n}_0(\psi' - \psi)$ and $\delta G = ik\tilde{n}_0(\psi' - \psi)$, this gives

$$\delta\tilde{n} \simeq \frac{\tilde{n}_0(\psi' - \psi)}{L}(1 - 2R^2 e^{-2i\tilde{n}\omega L/c}). \tag{3.44}$$

We have already investigated this modification to G, hence eq. 3.44 is the same as eq. 3.35 for time offset between the sample and reference data. We conclude that any of the effects we are considering are equivalent to a time offset and an additional scaling of the refractive index

$\tilde{n}' = \tilde{n}(\psi/\psi')$. This scaling alone does not introduce oscillations in the refractive index, in fact it will be undetectable, but the implied time offset will produce oscillations. Therefore the effect on G is equivalent to scaling the refractive index which is purely imaginary and linear with k. The effect on $\tilde{n}$ is a scaled value of the refractive index with amplitude oscillations on both the refractive index and extinction coefficient. The crucial point to note is that even though I have investigated the qualitative effects from incorrect sampling interval, sample thickness or orientation on the complex refractive index, these effects are indistinguishable and this creates difficulty in determining such errors in experimental data.

3.5.4 Sampling interval different in reference and sample data

A different sampling interval in the reference and sample data can occur due to the data acquisition errors. For example when multiple continuous scans by an oscillating delay stage are taken and the sampling rate is kept constant, there can be a change in the delay cycle frequency. This will produce data sets with a different number of data points with differing time intervals which is a problem for extraction because the Fourier components of the reference and sample spectra will not overlap producing errors. For the correct extraction it is required that the reference and sample scan have the same number of data points and time interval so that their spectra have the same frequency interval and spectrum length. To determine the effect of a different sampling interval between the sample and reference data the sampling rate of the sample data is defined as the correct sampling rate, so $y'(t) = y(t)$ and $x'(t) = x(t/\eta)$ where η is a number near unity which is the ratio of the sampling intervals used in the two data files. The spectra are related by $Y'(f) = Y(f)$ and $X'(f) = X(\eta f)$. The transfer function computed will then be

$$H'(f) = \frac{Y'(f)}{X'(f)} = \frac{Y(f)}{X(f)}\frac{X(f)}{X(\eta f)} = H(\eta f)\frac{X(f)}{X(\eta f)}. \tag{3.45}$$

The point of writing the modified transfer function in this form is that the change depends only on the reference signal and we can gain insight by using a simple model for this. Suppose $x(t)$ can be approximated as the derivative of a Gaussian pulse of width τ at time T:

$$x(t) = (t-T)e^{-(t-T)^2/\tau^2} \tag{3.46}$$

The corresponding spectrum is

$$X(f) \propto f e^{-\pi^2 \tau^2 f^2} e^{-2\pi i f T} \tag{3.47}$$

Let $\eta = 1 + \epsilon$ then, ignoring ϵ^2,

$$\frac{X(f)}{X(\eta f)} = \frac{1}{\eta} e^{+2\pi i e f T} e^{+2\pi^2 e \tau^2 f^2} \tag{3.48}$$

$$\delta G = -\ln(\eta) + 2\pi i \epsilon f T + 2\pi^2 \epsilon \tau^2 f^2 \tag{3.49}$$

In order to see how robust this conclusion is consider the alternative model of a derivative Lorentzian for the pulse, this will have an exponential spectrum, leading to δG being linear rather than quadratic in f. The value of ϵ could be positive or negative so δG may increase or decrease with frequency. The $\ln(\eta)$ term is frequency independent, leading to large $\delta \tilde{n}$ at low frequencies. The effect on G is a smooth change that is not necessarily a linear increasing or decreasing variation with frequency and does not vanish at zero frequency. The effect on $\tilde{n}$ is oscillations with amplitude possibly varying over the whole frequency range and large at low frequencies.

3.6 Conclusion

I have demonstrated data analysis various techniques which optimised the theoretical transfer function for material parameter extraction with the aim of improving the extracted complex refractive index. I have investigated the improved agreement between the Fresnel model and experimental data by finding the optimum length parameter required to reduce the Fresnel oscillations present on the complex refractive index. I also extracted the complex refractive index for different numbers of reflections in the theoretical transfer function compared with the experimental data. From the comparison it was concluded that as long as the number of reflections in the theoretical transfer function is equal to or larger than the number of reflections in the experimental data then the theoretical transfer function will be sufficient for the extraction. The infinite reflection transfer function is the optimum transfer function for THz time domain scans that include one or more reflections.

I have demonstrated a noise suppression algorithm which was applied to experimental data, it revealed spectral features where the SNR is low which would otherwise be hidden using standard material parameter extraction methods. This effectively increased the useful bandwidth of the THz-TDS system. The noise suppression algorithm modelled random spectrometer noise, with further noise characterisation, the technique could be improved. Ideally one would want to characterise deterministic noise of the THz system and actively measure the random noise with each scan. For example a beam splitter could be used to pick off part of the ultrafast laser beam to measure the fluctuations, the THz time domain scan could then be corrected according to the level of fluctuations. The lock-in amplifier has the capability to measure the noise on the photocurrent, this measurement could be used to characterise the noise on the THz system which would lead to a more accurate noise model and more effective noise suppression.

Finally, I approximated the theoretical transfer function to analytically determine how deficiencies in the transfer function with experimental data change the complex refractive index. The deficiencies investigated were the time offset between sample data and reference data, incorrect phase extrapolation to zero frequency, gain changes between sample and reference, incorrect sampling interval specified, incorrect sample thickness, sample misorienation with respect to the terahertz beam and sampling interval different in sample and reference data. The principle changes observed on the complex refractive index from these deficiencies was a shift or amplitude oscillations in either refractive index or extinction coefficient. If a combination of these deficiencies were to occur on experimental data it would be difficult to distinguish them from each other because the principle errors which they would create on the extracted complex refractive index are so similar. A more detailed analysis which is specific to the sample being investigated and includes simulation of these individual principle effects in the extraction process is required to determine the subtle differences. This work is relevant in cases where highly accurate determination of the complex refractive index is required and the THz system is on the limit of detection, for example material characterisation of thin films [88, 89].

Chapter 4

Converging beam extraction methods

4.1 Introduction

In terahertz time domain spectroscopy (THz-TDS), a series of lenses are used to guide THz radiation from the emitter to the receiver; depending on the sample that is investigated, either a collimated or a focused THz beam can be used. A focused beam is required when investigating small dimension samples so that the THz beam propagates entirely through the sample and is also necessary for high resolution THz imaging [108].

Material parameter extraction is a primary tool for investigating samples where the usual method is to fit a theoretical model of the THz electric field to the experimental data in the frequency domain. The closer the agreement between the model and the experiment the more accurate the extracted complex refractive index will be, this was demonstrated in chapter 3 using the Fresnel model transfer function. Material parameter extraction models based on transfer functions can be of varying complexity based on the requirements for accuracy and also the difficulty of factoring all experimental parameters [77, 100]. A common assumption for the theoretical model is that the THz beam is a plane wave. The plane wave hypothesis is commonly used for focused THz beam spectrometers in order to simplify the analysis, however it results in an overestimation of the refractive index due to underestimating the optical thickness.

At the focus of a converging THz beam a range of wave vectors produce a planar wave front due to the relationship between the phase contributions. A planar wave front however still has an angular spectrum and at the focus of the converging beam that is distinct from a collimated or planewave beam [109]. Therefore, even if the sample is placed in the focus, a converging beam assumption has to be used.

I present here an extraction method, which assumes a converging beam and is therefore more accurate than the plane wave assumption for converging beam experimental apparatus. There is research calculating or characterising the beam of a THz system [110, 111, 112, 113, 114] and limited experimental investigation showing the difference on the material parameter extraction when a converging or plane beam was used [115]. There is also recent research on material parameter extraction using a Gaussian beam assumption and single pass propagation [116].

The converging beam algorithm was developed by Dr Geoff Daniell and is based on the summation of plane waves. It can account for an arbitrary beam profile with an arbitrary frequency dependence including the reflection terms that give rise to the etalon effect. I will begin by describing the theory of the converging beam transfer function and show the application of the converging beam algorithm on simulated converging beam data, using a Gaussian and a top-hat beam profile which may occur within a THz-TDS setup. I will then demonstrate the converging beam algorithm on experimental data for a quartz sample which has been placed in both a collimated and focused section of the THz beam which is also compared to plane wave extraction. Finally, I use the converging beam extraction method to determine the angular beam profile of the focussed THz beam.

4.2 Converging beam Fresnel model

A transfer function describes mathematically the relation of input and output signals on a system, which is linear and time-invariant. Time invariance and linearity can be assumed true in a THz spectrometer. In the case of a material that is investigated in a THz spectrometer the input is the THz electric field as it reaches the material, after being generated by the emitter and propagated through the optical system. The output is the THz electric field after it is transmitted through the investigated material system as well as the optical system. In practice the experimental transfer function is easily calculated as the ratio of the spectra of one measurement performed without the sample and one measurement performed with the sample. As everything in the system, up to the material, and after it, is the same for both measurements, all these elements cancel out and the ratio of the reference and sample spectra reveals only the transfer function of the sample. The complex refractive index can be determined by fitting the theoretical transfer function to the experimental transfer function of the material, this has been described for the plane wave assumption in chapter 2. The converging beam extraction follows the same process as the plane wave extraction except the theoretical transfer function models a converging beam, the strategy is as follows:

1. Create an angular spectrum of plane waves that propagate through a material.
2. Determine the angular dependent transfer functions to apply to the individual angles.
3. Limit the angular spectrum to determine a beam profile.
4. Collect the angular spectrum by integrating over the angles to construct the converging beam transfer function.
5. Fit the converging beam transfer function to the experimental data using the Newton-Raphson method.

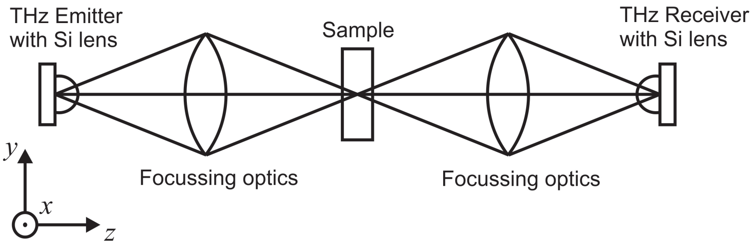

Figure 4.1: Schematic showing the propagation of the THz radiation along the z-axis. The transmitting dipole from the antenna is along the y-axis, the lenses represent the focusing optics used to focus and collimate the THz beam.

The converging beam is constructed using a summation of plane waves propagated at different angles. A schematic which shows the defined propagation of the converging beam is shown in Fig. 4.1. Axes are taken with the z-axis in the propagation direction of the THz beam and normal to the plane of the sample. The y-axis is parallel to the dipole transmitter axis and therefore parallel to the THz electric field. It is convenient to let $\boldsymbol{x}$, $\boldsymbol{y}$ and $\boldsymbol{z}$ to be unit vectors along the axes. The field of a transmitting dipole is expressed as an angular spectrum of plane waves and then the angles, which are used to form an image of the dipole antenna on the sample, are limited. The electric field of a transmitting dipole can be derived from a Hertz vector [117] along y using,

$$\mathbf{E} = \nabla\nabla \cdot \mathbf{\Pi} + \boldsymbol{k}^2\mathbf{\Pi} \tag{4.1}$$

and $\mathbf{\Pi}$ has only a $\boldsymbol{y}$ component

$$\Pi_y = \frac{e^{ikr}}{r}. \tag{4.2}$$

Specifically,

$$\mathrm{E}_x = \frac{\partial^2 \mathbf{\Pi}}{\partial x \partial y}, \tag{4.3}$$

$$\mathrm{E}_y = \left(k^2\mathbf{\Pi} + \frac{\partial^2 \mathbf{\Pi}}{\partial y^2}\right), \tag{4.4}$$

and,

$$\mathrm{E}_z = \frac{\partial^2 \mathbf{\Pi}}{\partial y \partial z}. \tag{4.5}$$

4.2.1 Angular spectrum of plane waves

The spherically symmetric quantity Π_y can be written as

$$\frac{e^{ikr}}{r} = \frac{i}{2\pi}\int_{-\infty}^{\infty}\int_{-\infty}^{\infty} \frac{e^{ik\cdot r}}{(k^2 - k_1^2 - k_2^2)^{1/2}} dk_1 dk_2, \tag{4.6}$$

with $k_1^2 + k_2^2 + k_3^2 = k^2 = \omega^2/c^2$, where k_1, k_2 and k_3 are the orthogonal components of the wave vector k, and k_3 is the propagation direction. The electric field components are obtained by doing the differentiations set out above in equations 4.3, 4.4 and 4.5, this introduces factors of,

$$\mathbf{E}(k_1, k_2) = \left(\frac{k_1 k_2}{k^2}, -\frac{(k^2 - k_2^2)}{k^2}, \frac{k_2 k_3}{k^2}\right). \tag{4.7}$$

This shows that $\boldsymbol{k} \cdot \mathbf{E} = 0$ so $\mathbf{E}$ is perpendicular to k as is required for a transverse wave. $\mathbf{E}$ lies in the plane of $\boldsymbol{k}$ and $\boldsymbol{y}$, also,

$$|\mathbf{E}|^2 = 1 - k_2^2/k^2 = 1 - \cos^2\alpha, \tag{4.8}$$

where α is the angle between k and the y-axis, so the magnitude of $\mathbf{E}$ is $\sin\alpha$ a condition required for dipole radiation.

To work out the reflection and transmission coefficients this electric field must be resolved into components $\mathbf{E}_{\|}$ in the plane of incidence and $\mathbf{E}_{\perp}$ normal to the plane of incidence because the Fresnel coefficients are polarisation dependent. The plane of incidence is that containing $\boldsymbol{k}$ and $\boldsymbol{z}$ so the vector $\boldsymbol{k} \times \boldsymbol{z} = (k_2, -k_1, 0)$ is perpendicular to it and a unit vector in this direction is $\boldsymbol{p} = (k_2/\bar{k}, -k_1/\bar{k}, 0)$ where $\bar{k}^2 = k_1^2 + k_2^2$. The perpendicular component of $\mathbf{E}$ normalised is therefore,

$$\mathbf{E}_{\perp} = (\mathbf{E} \cdot \boldsymbol{p})\boldsymbol{p} = \frac{k_1}{\bar{k}}\boldsymbol{p} = \left(\frac{k_1 k_2}{\bar{k}^2}, -\frac{k_1^2}{\bar{k}^2}, 0\right). \tag{4.9}$$

and the parallel component can be computed as,

$$\mathbf{E}_{\|} = \mathbf{E} - \mathbf{E}_{\perp} = \left(-\frac{k_1 k_2 k_3^2}{k^2 \bar{k}^2}, -\frac{k_2^2 k_3^2}{k^2 \bar{k}^2}, \frac{k_2 k_3}{k^2}\right). \tag{4.10}$$

4.2.2 Polarisation dependent transfer function

At the first surface of the sample the angle of incidence is given by $\cos\theta_1 = k_3/k$ or $\sin\theta_1 = \bar{k}/k$ and the angle of the transmitted wave θ_2 by $\tilde{n}_1 \sin\theta_1 = \tilde{n}_2 \sin\theta_2$. The polarisation dependent reflection and transmission coefficients [86] are

$$r_{\perp} = \frac{\tilde{n}_i \cos\theta_i - \tilde{n}_t \cos\theta_t}{\tilde{n}_i \cos\theta_i + \tilde{n}_t \cos\theta_t}, \tag{4.11}$$

$$r_{\|} = \frac{\tilde{n}_t \cos\theta_t - \tilde{n}_i \cos\theta_i}{\tilde{n}_i \cos\theta_t + \tilde{n}_t \cos\theta_i}, \tag{4.12}$$

$$t_{\perp} = \frac{2\tilde{n}_i \cos\theta_i}{\tilde{n}_i \cos\theta_i + \tilde{n}_t \cos\theta_t}, \tag{4.13}$$

$$t_{\parallel} = \frac{2\tilde{n}_i \cos\theta_i}{\tilde{n}_i \cos\theta_t + \tilde{n}_t \cos\theta_i}, \tag{4.14}$$

where $\tilde{n}_i$ and $\tilde{n}_t$ are the complex refractive indices and θ_i and θ_t are the angles of incidence and transmission appropriate for the interface involved. The propagation of the plane wave at non-normal incidence to an interface is shown in fig. 4.2, the red and blue indicates a polarisation component perpendicular and parallel to the plane of incidence respectively.

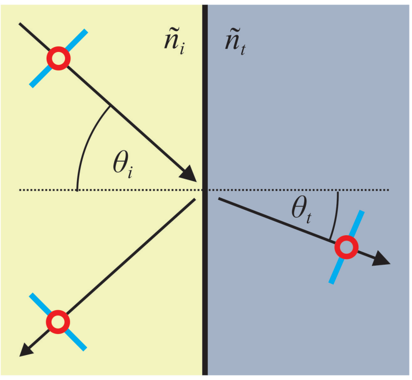

Figure 4.2: The propagation of the plane wave at non-normal incidence with polarisation components perpendicular and parallel to the plane of incidence shown by the red and blue respectively.

The propagation term becomes angle dependent such that $P_1 = e^{-i\tilde{n}_1 \omega L/c \cos\theta_2}$ where L is the sample thickness, however attention must be paid to the derivation of the propagation term in the transmission component. Ordinarily in the plane wave case the propagation coefficients in the transmission component of the transfer function would be P_1/P_2, this is the phase difference between propagating through the sample and air. The phase difference for the converging beam is equivalent to the phase difference for an etalon at an angle. To calculate the phase difference for an etalon at an angle a path length outside of the sample must also be considered as shown in fig. 4.3 by the blue line. The solution for the phase difference for a converging beam is $P_3 = \exp\left[-ikL(\tilde{n}_2 \cos\theta_2 - \tilde{n}_1 \cos\theta_1)\right]$.

The direct transmission of the THz pulse through the sample is expressed by multiplication of the field by $T_2 P_3 T_1$ where, $T_1 = t(\theta_1, \theta_2)$, $T_2 = t(\theta_2, \theta_1)$. Transmission with q pairs of internal

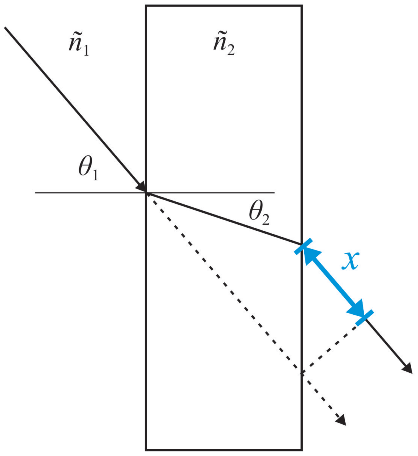

Figure 4.3: Propagation of a ray through an etalon showing the extra path length x outside of the etalon which must be taken into account when calculating the phase difference for the converging beam model.

reflections leads to,

$$T_2P_3T_1\sum_{q=0}^{+\infty}\{P_2R_2P_2R_2\}^q \tag{4.15}$$

where $R_2 = r(\theta_2,\theta_1)$ and $P_2 = e^{-i\tilde{n}_2\omega L/c\cos\theta_2}$. For an infinite number of the reflections the summation reduces to

$$\sum_{q=0}^{+\infty}\{P_2R_2P_2R_2\} = \frac{1}{1-P_2R_2P_2R_2}. \tag{4.16}$$

The polarisation dependent transfer functions are,

$$F_{\|} = t_{\|}(\theta_1,\theta_2)\cdot P_3\cdot t_{\|}(\theta_2,\theta_1)\cdot\frac{1}{1-P_2\cdot r_{\|}(\theta_2,\theta_1)\cdot P_2\cdot r_{\|}(\theta_2,\theta_1)} \tag{4.17}$$

and

$$F_{\perp} = t_{\perp}(\theta_1,\theta_2)\cdot P_3\cdot t_{\perp}(\theta_2,\theta_1)\cdot\frac{1}{1-P_2\cdot r_{\perp}(\theta_2,\theta_1)\cdot P_2\cdot r_{\perp}(\theta_2,\theta_1)}. \tag{4.18}$$

These equations are also the equivalent plane wave transfer functions for a sample placed at an angle with respect to the incident THz electric field. The electric field of the emerging wave from a sample is then:

$$\mathbf{E} = F_{\|}\mathbf{E}_{\|} + F_{\perp}\mathbf{E}_{\perp} \tag{4.19}$$

where $F_{\|}$ and $F_{\perp}$ are angle dependent plane wave transfer functions of the electric field with polarisations parallel and perpendicular to the plane of incidence respectively.

4.2.3 Collecting the angular spectrum

The emerging waves are focused on the detector. The focusing lens or mirror is a device that introduces phase delays so that all the waves arrive at the detector simultaneously. The signal at the detector is therefore obtained by summing over all k_1 and k_2. We will introduce a weighting function $W(k_1, k_2)$ to shape the beam which can be selected accordingly to match the beam profile of the spectrometer. The final result is that the detected signal is

$$\int\int \frac{W(k_1, k_2)}{k_3}(F_{\|}(k_3)\mathbf{E}_{\|} + F_{\perp}(k_3)\mathbf{E}_{\perp})dk_1 dk_2. \tag{4.20}$$

where

$$\mathbf{E}_{\|} = \left(-\frac{k_1 k_2 k_3^2}{k^2 \bar{k}^2}, -\frac{k_2^2 k_3^2}{k^2 \bar{k}^2}, \frac{k_2 k_3}{k^2}\right). \tag{4.21}$$

and

$$\mathbf{E}_{\perp} = \left(\frac{k_1 k_2}{\bar{k}^2}, -\frac{k_1^2}{\bar{k}^2}, 0\right) \tag{4.22}$$

The x and z components are antisymmetric in either k_1 or k_2 and so the integrals vanish and, as expected, there is only a y component at the focus. If we convert to polar coordinates in the k_1, k_2 plane, writing $k_1 = \bar{k}\cos\phi$ and $k_2 = \bar{k}\sin\phi$ the ϕ integral for the y component gives a value of π. The final result is

$$\frac{1}{2}\int_0^{\infty} \frac{W(\bar{k})}{k_3}\left(\frac{k_3^2}{k^2}F_{\|}(k_3) + F_{\perp}(k_3)\right)\bar{k}d\bar{k}. \tag{4.23}$$

If we convert to polar coordinates in the $\bar{k}$, k_3 plane where $\bar{k} = k\sin\theta$ and $k_3 = k\cos\theta$, the final result is

$$-\pi\int_0^{\theta_{max}} W(\theta)(\cos^2\theta F_{\parallel}(\theta)+F_{\perp}(\theta))\sin\theta d\theta. \tag{4.24}$$

Now the weighting function becomes $W(\theta)$ which defines the angular profile of the THz wave that is emitted from the antenna and collected from the lenses. An upper limit of ∞ is irrelevant and is replaced by θ_{max} because the $W(\theta)$ reduces the integrand to zero at some finite angle. The finite angle also removes evanescent waves from the model which can occur at large angles.

To create a transfer function the signal from the sample scan is divided by a reference signal which can be obtained by setting $\tilde{n}_1 = \tilde{n}_2 = 1$ when $F_{\parallel}$ are $F_{\perp}$ both equal to unity in eq. 4.24. The transfer function for a converging beam through the sample is therefore obtained by dividing by,

$$-\pi\int_0^{\theta_{max}} W(\theta)(1+\cos^2\theta)\sin\theta d\theta \tag{4.25}$$

to give

$$H_{conv}(\omega,\theta_{max}) = \frac{\int_0^{\theta_{max}} W(\theta)(\cos^2\theta F_{\parallel}(\theta)+F_{\perp}(\theta))\sin\theta d\theta}{\int_0^{\theta_{max}} W(\theta)(1+\cos^2\theta)\sin\theta d\theta}. \tag{4.26}$$

The calculation of the transmission of the converging beam through the sample requires the numerical evaluation of these integrals during the fitting process. A Gaussian integral is used for the integrands which requires no significant computational burden. The fitting process also uses the Newton-Raphson method discussed in section 2.4 which requires the derivative of the transfer function. In the plane wave case the transfer function derivative was calculated analytically, however because the converging beam transfer function is more complex than the plane wave transfer function the finite difference method was used.

In the converging beam case it is difficult to perform phase unwrapping due to each wave for a single frequency undergoing a different phase shift. Therefore the converging beam transfer function is fitted to the experimental amplitude and raw phase. To ensure that the extraction process will converge to the correct value the plane wave algorithm is used to find the approximate value for the refractive index, which is then set as the initial guess refractive index value for the Newton-Raphson method in the converging beam extraction.

4.2.4 Limiting the angular spectrum

The final step is to select the weighting function $W(\theta)$ that should be used in eq. 4.26 to match the beam profile produced from the THz-TDS setup. The beam profile of a THz spectrometer is dependent on the geometry of the photoconductive emitter, the presence of a silicon lens and the optics used to focus the beam. In practise the measurement of the actual beam profile is a difficult task to perform and would require a new measurement for any significant alignment changes within a setup. In 1996, Jepsen et. al. [53] showed that a THz beam profile from a photoconductive emitter with a silicon lens can be approximated with a Gaussian beam emitted from a circular aperture equal to the diameter of the lens. A similar setup but with the addition of one focusing lens was measured by Jiang et. al. [113]. Since then, more research on THz beam profiling [112] has shown that a better approximation would be a series of Laguerre-Gaussian modes for THz beam propagation. Furthermore, the electric field in a focus of lenses was measured in [110, 111] and it was again found that THz-TDS exhibit behaviour that is affected by diffraction from an aperture.

The algorithm has the capability to model an arbitrary angular beam profile, here I have modelled a single mode Gaussian beam profile and also a top-hat beam profile as there are valid arguments for both approximations in most THz spectrometers. A Gaussian beam profile would assume that most of the beam is collected by the focusing mirrors, however this is unlikely to happen in experiment due to the finite size of the mirrors. The beam is likely to be apodized producing a sharper cut off in the angular spectrum in which case the top-hat beam profile would test the upper limit of this scenario. A top-hat beam profile would exhibit the Airy diffraction patterns that were measured in [110, 111, 112, 53].

A Gaussian function was simply used for the weighting function to produce the Gaussian beam profile. The half width of the Gaussian function determines the half angle of the angular spectrum, half width and half angle is used interchangeably throughout this chapter. The half width was defined as the $1/e^2$ level of the Gaussian function so that the beam waist ω_0 is related to the half width using

$$\omega_0 = \frac{c}{\pi \nu \theta_{1/e^2}} \tag{4.27}$$

where θ_{1/e^2} is the half width for a Gaussian beam, c is the speed of light, ω_0 is the beam waist

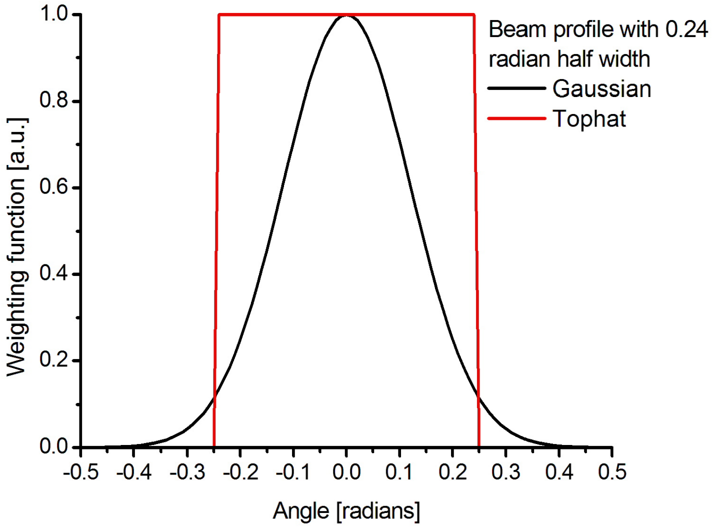

Figure 4.4: Weighting function for a Gaussian and a top hat beam profile.

and ν is the frequency. The weighting functions for the Gaussian and top hat beam profiles are shown in fig. 4.4, the top hat profile includes all angles of the converging beam up to the set half width. All angles beyond the half width are cut off, the focal ratio of the THz focusing optics will determine the appropriate half width to use. For example the TeraView data in section 2.6 was taken on a converging beam setup using 2 inch ellipsoid mirrors that have a focal ratio of 2, this limits the half width of the converging beam to 0.24 radians. The half width was calculated using,

$$\theta = \arctan \frac{D}{2f} \tag{4.28}$$

where D is the diameter and f is the focal ratio of the optics which focus the THz beam on the sample. The larger the half width, the greater the angular spectrum of the converging beam and the further from the plane wave model the converging beam solution will become.

4.3 Converging beam extraction using simulated data

An algorithm was also produced from the converging beam transfer function that allowed for simulated data with a converging beam to be generated. The simulated data was generated by applying the converging beam transfer function to an experimental reference scan with set parameters for sample thickness, complex refractive index, beam profile and half width. The sample thickness was 500 μm and the complex refractive index was $\tilde{n} = 1.975 - 0.000i$, both the Gaussian and top-hat beam profiles were used with a half width of 0.24 radians. The resultant simulated scans for the Gaussian and top-hat profiles are shown in fig. 4.5 with the original reference scan, the top-hat beam is similar to the Gaussian beam except for a small delay of the THz pulses. The advantage of using simulated data is that the original material parameters are known.

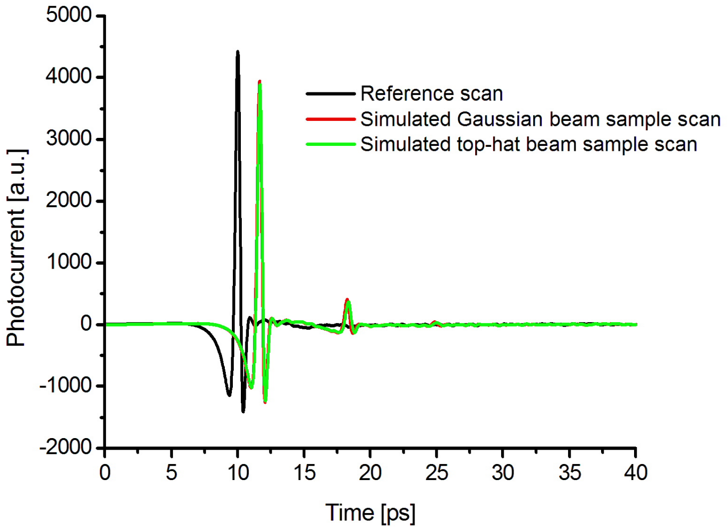

Figure 4.5: Simulated scan for a converging Gaussian beam with half width of 0.24 radians propagating through a sample of thickness 500 μm and complex refractive index was $\tilde{n} = 1.975 - 0.000i$. The original reference scan is also shown.

The simulated data are extracted with the appropriate beam profile using different half widths and also with the plane wave extraction algorithm. This has been done in order to determine the behaviour of the converging beam extraction algorithm on the complex refractive index. The half widths used for the Gaussian profile extraction were 0.00 - 0.48 radians in steps of 0.08 radians and the half widths used for the top-hat profile were 0.00, 0.08, 0.16, 0.24, 0.28 and 0.32 radians. The converging beam data were also produced using zero reflections and extracted with zero reflections to observe the effects from the transmission component of the transfer function and distinguish from effects which are due to the Fresnel reflections.

4.3.1 Refractive index

The extracted refractive indices for the Gaussian profile are shown in fig. 4.6, as expected the correct refractive index of 1.975 is extracted when the correct half width of 0.24 is used. When the half width deviates either side of the actual half width there is a shift in the refractive index, the dashed lines show the change in refractive index due to the transmission component of the transfer function which is effectively the average shift in the refractive index.

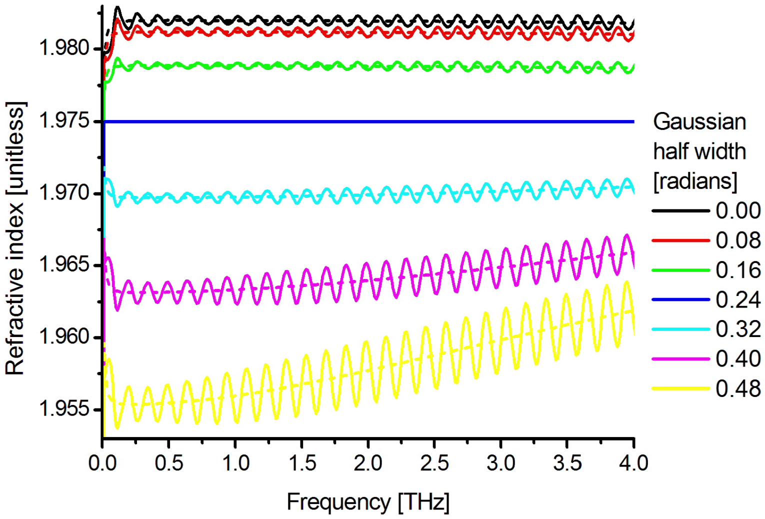

Figure 4.6: Refractive index for simulated data produced using a Gaussian half width of 0.24 radians which was then extracted using Gaussian half widths ranging from 0.00 - 0.48 radians in steps of 0.08 radians. The dashed lines show the change in refractive index due to the transmission component of the transfer function.

The sample thickness, refractive index and beam profile determines a range of optical path lengths in which the converging beam propagates; because there is no single optical path length it is useful to consider an average optical path length. The change in refractive index can be described in terms of this average optical path length that the converging beam experience when propagating through the sample. The phase of the experimental transfer function is determined by the average optical path length, when extracting the data the theoretical transfer function will change the refractive index in order to maintain consistency with the phase. This behaviour is analogous to a change in length parameter which was discussed in section 3.2, as the half width is increased from zero radians the refractive index decreases, this is because the effective optical path length determined by the theoretical transfer function assumes a greater range of optical paths lengths for larger half widths. This increases the average optical path length and reduces the refractive index, in other words the THz pulse travels faster through the sample maintaining the original phase of the experimental transfer function.

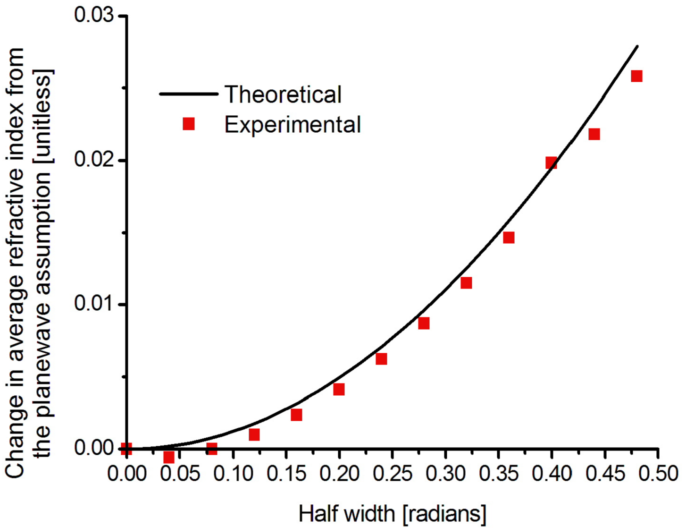

Figure 4.7: Change in the average refractive index from the plane wave assumption for different half widths of the Gaussian profiles.

The average optical path length can be deduced analytically from the integral of the converging beam transfer function to determine the average change in refractive index for different half widths, this can be compared with the changes seen in the extracted data. The comparison is shown in fig. 4.7 where the change in refractive is measured from the plane wave assumption, the experimental data points were determined by measuring the refractive index due to the transmission component of the transfer function at 300 GHz for each half width. The theoretical line was derived from the average optical path length due to a Gaussian beam profile as it propagates through the sample with a refractive index of 1.975 compared to the optical path length encountered by a Gaussian beam with half width 0.24 radians propagating through the same sample. A very close agreement between the experimental data points and theoretical curve is observed, the figure shows how the average optical path length of a Gaussian beam changes with an increasing range of angles present in the converging beam.

The smallest average optical path length is a zero half width, equivalent to the plane wave assumption which was used in chapter 2. The largest average optical path length is dependent on the focal ratio of the THz focusing optics, the simulated data was extracted for a mirror with a focal ratio of 2 which is a 0.24 radians. Practically it is unlikely that focusing optics that are used in a THz spectrometer will have focal ratio of less than 1 which puts an upper limit of 0.52 radians for the half width. The greater the difference in optical path between the experimental data and theoretical transfer function the greater the change in the refractive index, experimentally this means that the largest errors produced from extraction will be when collimated THz data is used in a converging beam algorithm or extracting focused THz data using a plane wave algorithm.

The change in refractive index is frequency dependent for the incorrect half widths, this is particularly apparent for the half widths which are greater than 0.24 radians. The Fresnel component of the transfer function introduces oscillations on the refractive index where there is a mismatch between the average optical path length of the experimental and theoretical transfer functions, hence when the correct half width is used there are no oscillations. The amplitude of the oscillations are also dependent on the mismatch between, the larger the mismatch the greater the oscillation amplitudes. The oscillation amplitudes appear to increase with frequency however this is the effect of the frequency beating similar to those observed in section 3.2. The frequency of the beats are dependent on the mismatch of the experimental and theoretical average optical path lengths, due to the small difference the beat frequencies are relatively large in comparison to the THz extraction range hence the second node of the beat is unobservable.

The extracted refractive indices for the top-hat profile are shown in fig. 4.8, the top-hat profile gives the same behaviour of the refractive index as Gaussian profile but the change in refractive index for a given half width is larger than the change in refractive index observed in the Gaussian profile. This is because the average optical path length for a given half width is greater than

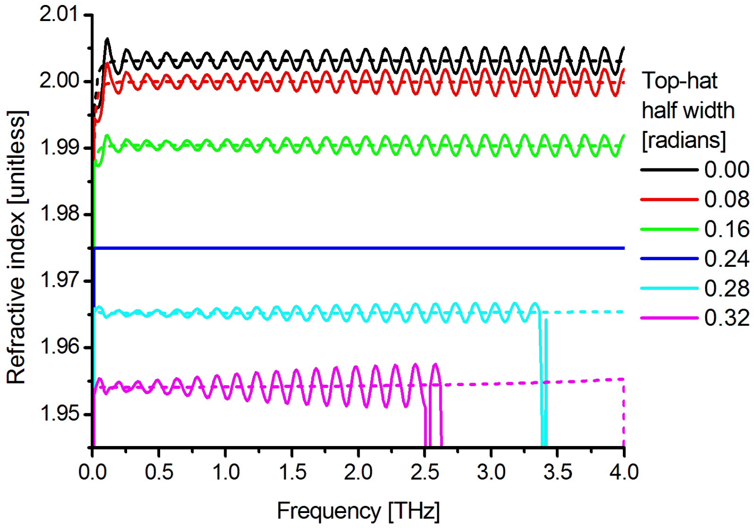

Figure 4.8: Refractive index for simulated data produced using a top-hat half width of 0.24 radians which was then extracted using the top-hat half widths 0.00, 0.08, 0.16, 0.24, 0.28 and 0.32 radians. The dashed lines show the change in refractive index due to the transmission component of the transfer function.

the Gaussian profile. The change in average optical path length is large enough, that the half widths 0.28 and 0.36 radians give failed extraction at high frequencies, which means the Newton-Raphson method was unable to fit the theoretical transfer function to the experimental transfer function with an accuracy of 10^{-7} within 100 iterations.

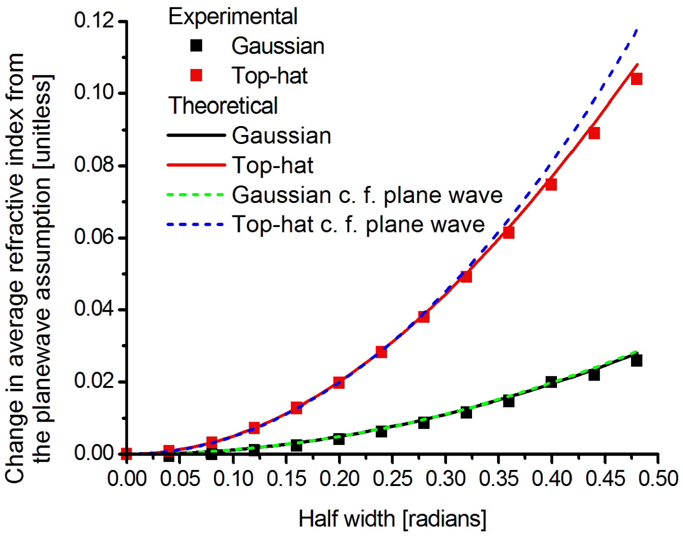

Figure 4.9: Change in the average refractive index from the plane wave assumption for different half widths of the Gaussian and top-hat profiles. The dashed lines show changes in the refractive index for converging beam extraction of data that are derived using the plane wave assumption. The solid lines show changes in the refractive index for converging beam extraction of data that are derived using the converging beam assumption with a half width of 0.24 radians.

The change in the average refractive index from the plane wave assumption for both the Gaussian and top-hot profiles is shown in fig. 4.9. The changes in refractive index for the top-hat profile were calculated using the same method as mentioned for the Gaussian profile in fig. 4.7, the dashed lines was derived from the average optical path length due to the their respective profile compared with an optical path length experience by plane wave, instead of a converging beam. For a given change in half width the top-hat profile produces larger changes in the refractive index than the Gaussian profile due to the larger average optical path length, the change in refractive index is dependent on the mismatch between the average optical path length of the original data and the average optical path length incorporated by the converging beam model. These findings highlight that the change in refractive index due to the converging beam compared with the plane wave assumption can be predicted by calculating the change in average optical path length which the THz electric field experiences.

The Gaussian and top-hat profiles represent the upper and lower limits of beam profiles which could occur in the THz-TDS setup. The Gaussian beam profile represents the scenario where the beam produced from a photoconductive antenna with Si lens is completely collected by the lens producing a Gaussian beam at the focus. The top-hat beam profile represents the scenario where the beam is not completely collected but is clipped at the edges, in practice the beam profile of a typical THz spectrometer will sit between these two scenarios [53]. Therefore by using this choice of profiles provides a good estimate of the range of error in refractive index for a converging beam setup when extracting the optical constants of a sample using a plane wave algorithm.

4.3.2 Extinction coefficient

The extinction coefficient for the Gaussian and top-hat profiles are shown in fig. 4.10 and fig. 4.11 respectively. Changing the half width from 0.24 radians produces a frequency dependent shift and Fresnel oscillations in both cases, however the magnitude of the shift and Fresnel oscillations on the top-hat profile are greater than the Gaussian profile due to the greater average optical path length.

The behaviour of the extinction coefficient due to a changing half width is similar to the change in extinction coefficient observed in section 3.2.1 for a changing length parameter. The determination of the extinction coefficient is dependent on the fit between the real part of the theoretical transfer function and amplitude of experimental transfer functions, however within the real part of the transfer function there is both the refractive index and extinction coefficient. This means that the extracted extinction coefficient is also dependent on the extracted refractive index so any frequency dependence observed on the refractive index can be imposed onto the extinction coefficient and vice versa.

The effect of the converging beam produces a frequency dependent curvature on both the refractive index and extinction coefficient. The curvature on the extinction coefficient appears larger than the curvature on the refractive index, this is due to the relative size of the extinction coefficient compared with the refractive index, they are in fact the same magnitude. The

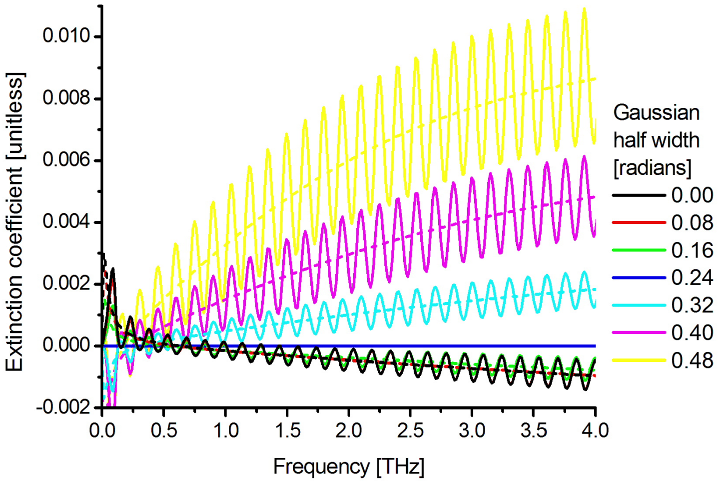

Figure 4.10: Extinction coefficient for simulated data produced using a Gaussian half width of 0.24 radians which was then extracted using Gaussian beam half widths ranging from 0.00 - 0.48 radians in steps of 0.08 radians. The dashed lines show the change in extinction coefficient due to the transmission component of the transfer function.

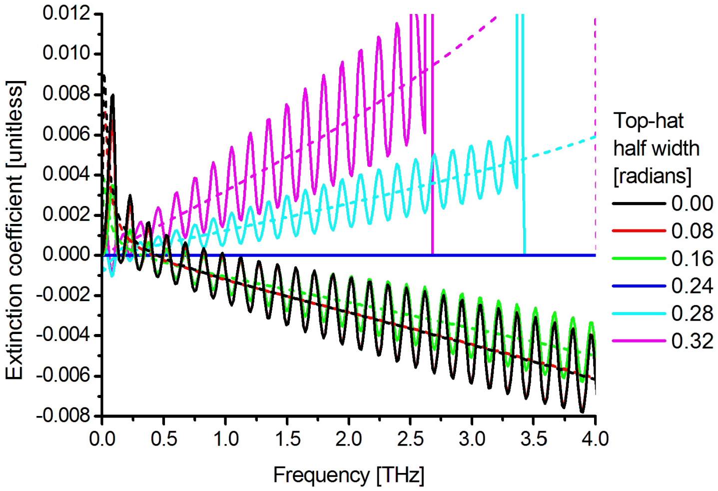

Figure 4.11: Extinction coefficient for simulated data produced using a top-hat half width of 0.24 radians which was then extracted using the top-hat beam half widths 0.00, 0.08, 0.16, 0.24, 0.28 and 0.32 radians. The dashed lines show the change in extinction coefficient due to the transmission component of the transfer function.

magnitude of the curvature with respect to different half widths is proportional to the mismatch between optical path lengths for the theoretical and experimental transfer function, when there is no mismatch the correct extinction coefficient is extracted. The amplitudes of the Fresnel oscillations are dependent on how far the extinction coefficient is shifted from the correct extinction coefficient.

4.3.3 Sample orientation

In section 3.2 it was shown that the optimum length parameters of the 567 μm, 1090 μm and 2054 μm fused silica samples were approximately 2% smaller than their respective measured thicknesses which suggested the presence of a systematic error in the THz time domain scans. In cases where the optimum length parameter is larger than the measured thickness of the sample other systematic errors which would produce the effect of a larger thickness can be considered. This includes the effect of the converging beam and also the orientation of the sample with respect to the propagation of the THz beam. A sample surface that experiences non-normal incidence of the THz beam will introduce a longer propagation length for the THz pulse through the sample and increase the apparent thickness in the THz time domain scans.

The effect that the orientation of the sample has on the extracted complex refractive index can be tested by modeling sample orientation into the theoretical transfer function. A plane wave THz beam which propagates through a sample off of normal incidence will experience different Fresnel reflections and transmission components to normal incidence which are dependent on both angle and polarisation. The plane wave transfer functions for this are the same as $F_{\parallel}$ (eq. 4.17) and $F_{\perp}$ (eq. 4.18) used to construct the converging beam transfer function except θ_1 is now the angle between the normal to the sample surface and the axis of propagation of the THz beam.

I have used the plane wave transfer function which models a sample at an angle perpendicular to the polarisation of the THz electric field to simulate a THz time domain scan of a sample at an angle. The incident plane wave THz beam is modeled to be at a angle of 1° with respect to the normal of the sample surface. The sample has a complex refractive index of $2.000 - 0.005i$ and a thickness of 500 μm. The simulated THz time domain data were then extracted with the same angle dependent plane wave transfer function using the angles 0°, 1°, 2° and 3°.

Figures. 4.12 and 4.13 show the refractive index and extinction coefficient respectively. The correct refractive index and extinction coefficient is determined when the correct angle of 1° is

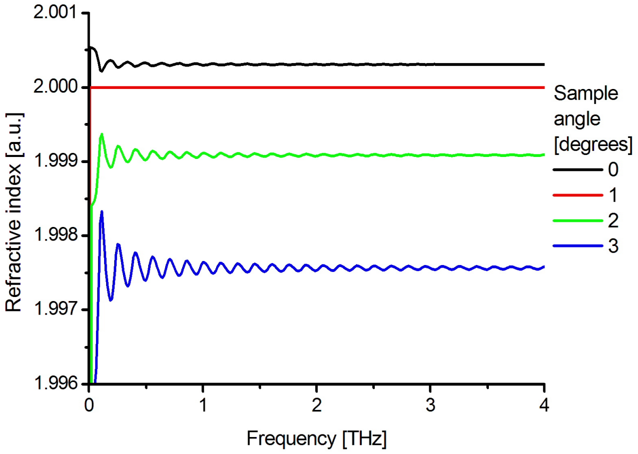

Figure 4.12: Refractive index of simulated data that was extracted with an angle dependent plane wave transfer function using the angles 0°, 1°, 2° and 3°. The simulated data was created with the same angle dependent plane wave transfer function at an angle of 1°, a complex refractive index of $2.000 - 0.005i$ and a thickness of 500 μm. The correct refractive index (red) is extracted using the 1° angle.

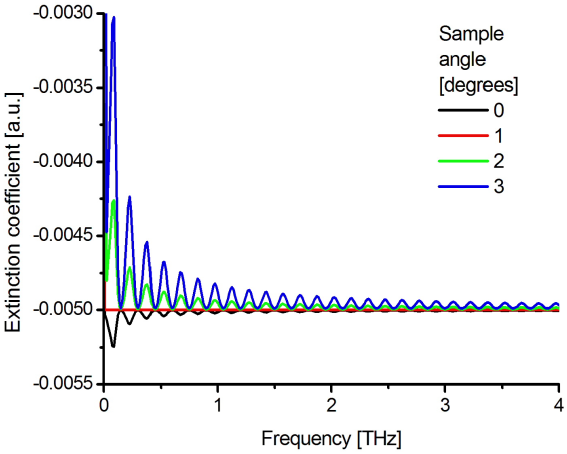

Figure 4.13: Extinction coefficient of simulated data that was extracted with an angle dependent plane wave transfer function using the angles 0°, 1°, 2° and 3°. The simulated data was created with the same angle dependent plane wave transfer function at an angle of 1°, a complex refractive index of $2.000 - 0.005i$ and a thickness of 500 μm. The correct extinction coefficient (red) is extracted using the 1° angle.

used in the extraction process. The behaviour of the refractive index and extinction coefficient when using the incorrect angle is similar to using the incorrect length parameter described in section 3.2. There is a shift in the refractive index and oscillations occur on both the refractive index and extinction coefficient. The complex refractive index that was extracted with an angle of 0° is essentially a plane wave extraction, the error in the refractive index and extinction coefficient is created by not accounting for the sample at an angle of 1°. It shows that sample orientation is crucial for highly accurate determination of the complex refractive index in the case where THz time domain scans are taken in the collimated section of the THz beam and the plane wave material parameter extraction method is used. The angle dependent material parameter extraction method which has been demonstrated here could in practise be used to remove the effects on the complex refractive due to sample misorientation. Future work to determine its effectiveness at removing the effects on the complex refractive would be to place a sample at an known angle in the collimated section of the THz beam and to then extract with the angle dependent transfer function.

4.4 Comparison between collimated and focused THz scans using real data

THz time domain scans of a quartz sample were taken with the sample placed in the collimated section and also in the focus of the THz beam by Dr. Axel Zeitler at the University of Cambridge. The collimated and focused THz beam scans are shown in fig. 4.14, the quartz sample had a thickness of 2 mm and diameter of 2 inches. A schematic of the THz spectrometer used is shown in fig. 4.15, the THz setup was pumped with a Titanium Sapphire laser with a central wavelength of 800 nm and pulse duration of 30 fs. The emitter was a LT-GaAs strip-line PCA with a 100 μm gap. Non-linear detection using a ZnTe crystal was used and the THz beam was collimated and focused using parabolic mirrors with a focal ratio of 1.5. A fast delay stage was used to take 2200 scans which are averaged to produce a scan with approximately 5000 time steps and a scan length of 54.3 ps.

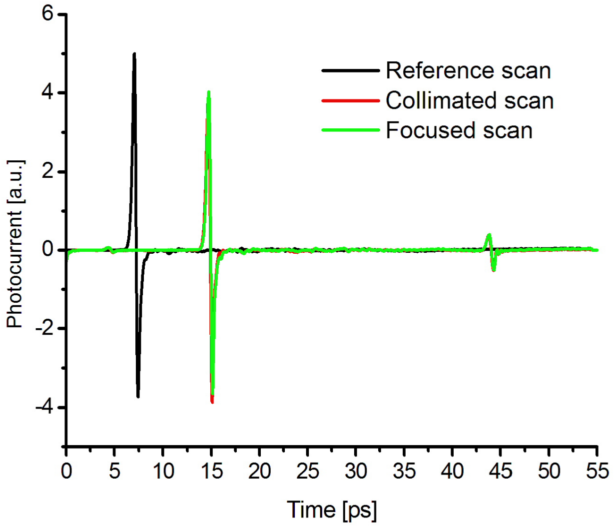

Figure 4.14: THz time domain scans of a 2 mm thick quartz sample place in a collimated section and focus of the THz beam, and also a reference scan. The focused scan is on top of the collimated scan.

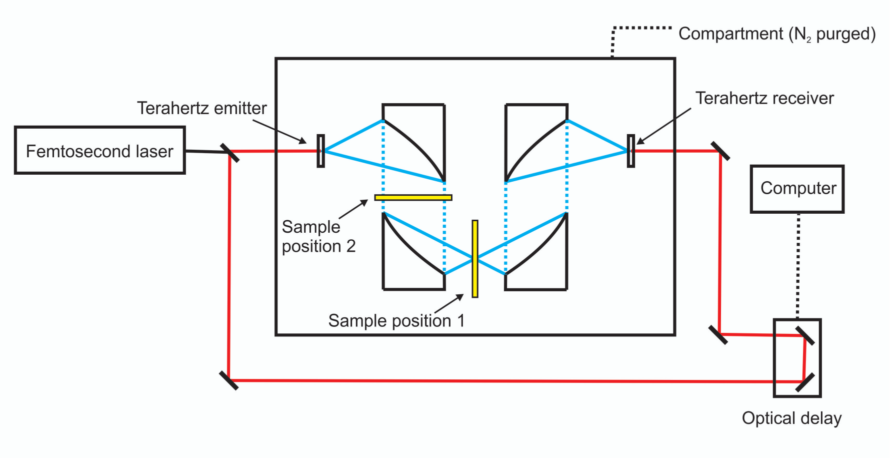

Figure 4.15: Schematic of the THz spectrometer used to take scans in the collimated and focused section of the THz beam.

4.4.1 Plane wave extraction

The complex refractive index for the quartz sample placed in the collimated and focused section of the THz beam were extracted using the plane wave algorithm with a length parameter of 2000 μm. The extraction was performed using the infinite reflection transfer function with the full time duration of the scan, the data were also truncated to remove the first reflection and then extracted using the zero reflection transfer function. The refractive index is shown in fig. 4.16, the original non-truncated extractions show large Fresnel oscillations whereas the truncated data reduces the amplitude of the oscillations giving a clearer comparison between refractive indices. The large oscillations are a result of the prepulse observed at 5 ps on the THz scans shown in fig. 4.15. The truncation does not remove the prepulse, hence oscillations are still present when extracting with the zero reflection transfer function.

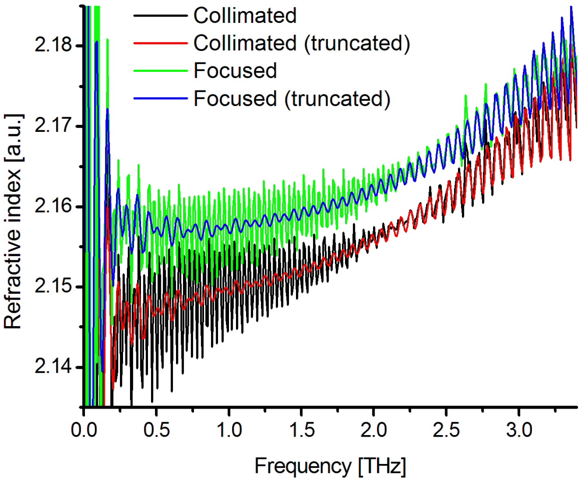

Figure 4.16: Refractive index of 2 mm quartz sample placed in the collimated and focused sections of the THz beam that was extracted using the plane wave algorithm. The extraction was performed using the full data length with the infinite reflection transfer function and truncated data with the zero reflection transfer function.

The refractive index of the focused scan is larger than refractive index of collimated scan, this is due to the focused THz beam. The focused THz beam has propagated through the sample a larger distance than the collimated beam, the plane wave algorithm does not account for this

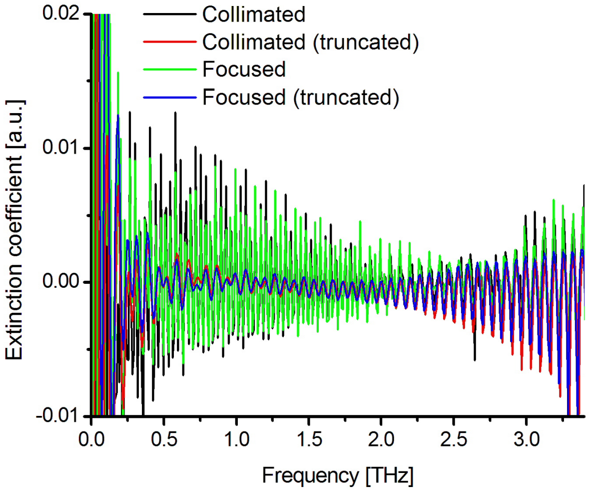

Figure 4.17: Extinction coefficient of 2 mm quartz sample placed in the collimated and focused sections of the THz beam that was extracted using the plane wave algorithm. The extraction was performed using the full data length with the infinite reflection transfer function and truncated data with the zero reflection transfer function.

and therefore underestimates the optical path length. The theoretical transfer function therefore over estimates the refractive index to maintain consistency with the phase of the experimental data. This error in the refractive index is the equivalent of the Gouy phase shift which was reported by Kuzel et. al. in [116] where they also describe a shift of the refractive index. The extinction coefficient is shown in fig. 4.17, it shows consistency between the different positions on the THz beam which suggests the absorption due to the quartz sample is small.

4.4.2 Converging beam extraction

The converging beam algorithm models the focused beam, and provided the correct beam profile is used, it can determine the correct refractive index for samples in a focused beam THz spectrometer. In this example the refractive index of the quartz is known because the sample was also placed in the collimated beam and extracted with the plane wave algorithm, therefore by assuming a Gaussian beam profile and changing the half width until it matches the known refractive index the beam profile of the setup can be estimated.

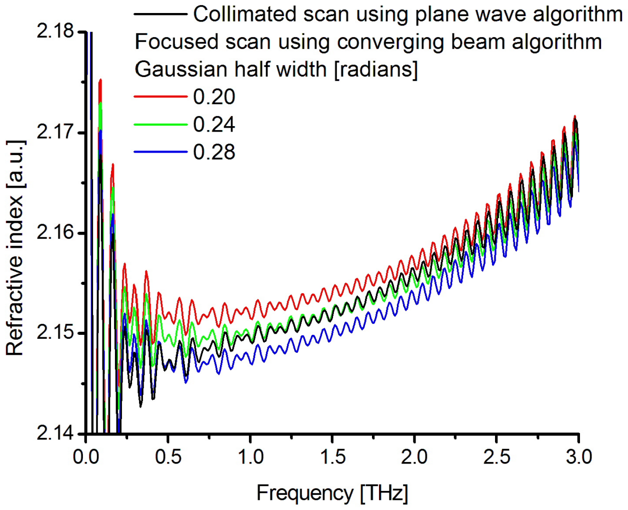

Figure 4.18: Refractive index comparison between the collimated beam scan extracted with the plane wave algorithm and the focused beam scan extracted using the converging beam algorithm with different Gaussian half widths.

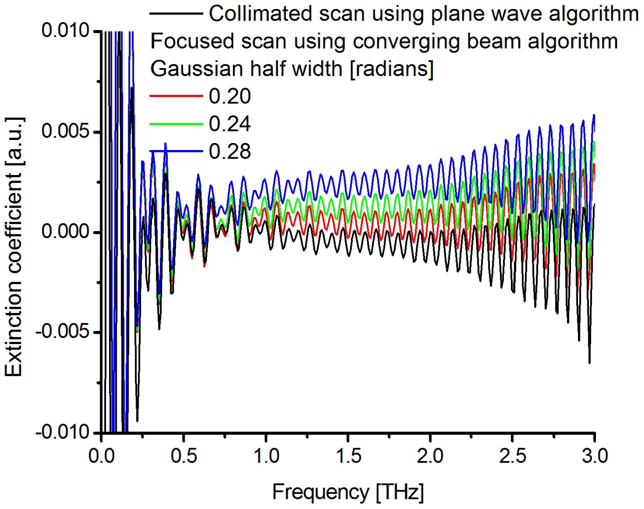

Figure 4.19: Extinction coefficient comparison between the collimated beam scan extracted with the plane wave algorithm and the focused beam scan extracted using the converging beam algorithm with different Gaussian half widths.

The refractive index and extinction coefficient for the focused scan extracted using the converging beam algorithm with a Gaussian profile is shown in figures 4.18 and 4.19 respectively. The collimated beam scan extracted with the plane wave algorithm is also shown for comparison. The extraction was made using the zero reflection transfer function and truncated data which removed the first reflection so that the change in complex refractive index is clear. The Gaussian half widths used were 0.20, 0.24 and 0.28 radians, the fit between the collimated and focused scans is frequency dependent. The refractive index with a half width of 0.28 shows the best fit for frequencies under 0.7 THz, the half width of 0.24 radians shows the best fit for the rest of the THz range. This suggests that under 0.7 THz the beam is more converging where the difference in optical path length between the plane wave and converging beam assumptions is greater. This supports the behaviour of the converging beam observed in the simulated data which suggested that the THz beam becomes less converging with frequency. This behaviour is also consistent with diffraction theory, which suggests that at higher frequencies the beam is less divergent and therefore closer to the plane wave assumption, which allows for a more accurate extraction in that region. The half width of 0.20 radians shows a poor fit at low frequencies but at high frequencies it converges towards the correct refractive index. The Gaussian half widths used for the extraction fall within 0.32 radians which is the maximum half width expected from parabolic mirrors with a focal ratio of 1.5, diffraction could also be the reason why the extraction favoured a half width of 0.24 radians. The extinction coefficient experiences a frequency dependent shift which is the same as that observed on simulated data in section 4.3.2, as the half width increases the changes in extinction coefficient increases with frequency in the positive direction.

4.4.3 Beam profiling

The construction of a converging beam material parameter extraction method in addition to THz time domain scans of a sample placed in the collimated and focused sections of the THz beam on the same apparatus enable and an elegant method to profile the angular spectrum of the converging beam. This done by fitting the refractive index of the focused THz time domain scans using the converging beam extraction to the refractive index extracted from the collimated THz time domain scan using the plane wave extraction by changing the Gaussian half width. Provided there are no experimental errors on the collimated THz timed domain scan it is assumed that the collimated THz time domain scan using the plane wave extraction is correct.

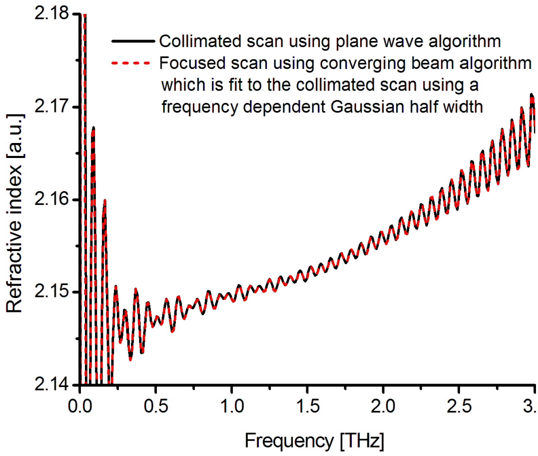

Figure 4.20: Refractive index (dashed red) of focused THz scan extracted using the converging beam extraction method with a Gaussian beam profile. The Gaussian half width is varied until the refractive index fits the refractive index (solid black) of the collimated THz scan using the plane extraction. The converging beam extraction enable a close fit between the collimated and focused refractive indices.

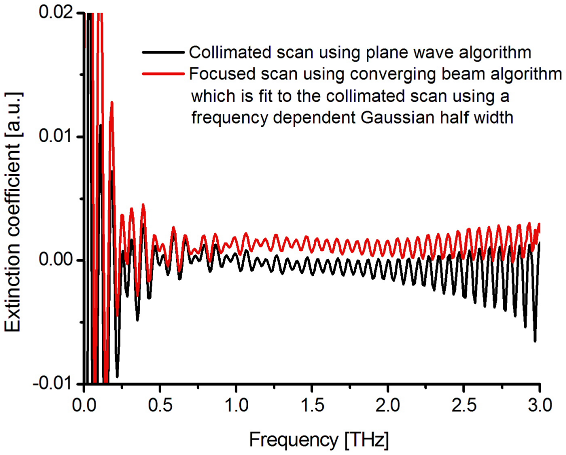

Figure 4.21: Extinction coefficient (red) of focused THz scan extracted using the converging beam extraction method with a Gaussian beam profile. The Gaussian half width is varied until the refractive index of focused THz scan extracted using the converging beam extraction method fits the refractive index (black) of the collimated THz scan using the plane extraction. There is a small mismatch between the collimated and focused extinction coefficients because the fit is between the refractive indices.

Figure 4.20 shows the fit between the refractive index of focused THz scan extracted using the converging beam extraction and the refractive index of the collimated THz scan using the plane extraction. The converging beam extraction using the Gaussian half width enables a very close fit between the refractive indices. Figure 4.21 shows the extinction coefficient of the collimated scan using the plane algorithm and also the extinction coefficient of the focused scan using the converging beam extraction which was fit to the refractive index of the collimated scan. The extinction coefficients show some mismatch, this is because it is the refractive indices of the scans which are fit to each other and not the extinction coefficients.

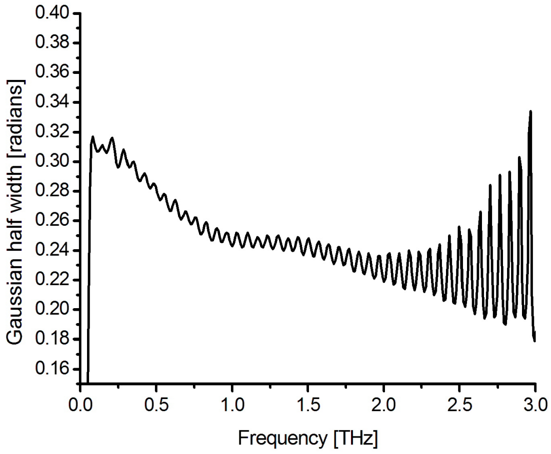

Figure 4.22: The Gaussian half width required to fit the refractive index of the focused scan using the converging beam algorithm to the refractive index of the collimated THz scan using the plane extraction. The Gaussian half width becomes smaller with frequency which suggests that the THz beam becomes less divergent at higher frequencies. The oscillations present on the beam profile are a result of the oscillations present on the complex refractive index.

The resultant Gaussian half width is shown in fig. 4.21, at low frequencies the Gaussian half width is at the maximum half width expected from parabolic mirrors with a focal ratio of 1.5 which is 0.32 radians. The half width becomes smaller with higher frequency which suggests that the THz beam becomes less divergent, this could be due to diffraction. There is a region between 1.0 - 1.5 THz where the half width is approximately 0.24 radians, this coincides with the favoured half width that was determined in the analysis of fig. 4.18. The analysis I demonstrate here is far more concise, I have demonstrated a method to determine the frequency dependent beam profile of a focused THz time domain spectrometer. Furthermore, this method has a distinct advantage in that it does not require any realignment of components in the THz time domain spectrometer. Theoretically this beam profiling method can be applied to any THz spectrometer with access to a collimated and focused section of the THz beam which is common in most THz time domain spectrometers that use the four parabolic setup as shown in fig. 4.15. This method does require samples large enough to be completely illuminated by the collimated section of the THz beam. The combination of a converging beam extraction method and the determination of the beam profile at the THz focus will enable a more accurate determination of the complex refractive index for materials where a THz focus is essential.

4.5 Conclusion

I have demonstrated a converging beam material parameter extraction method, which uses an arbitrary frequency dependent angular profile and takes into account an arbitrary number of internal reflections. Two different angular beam profiles were used, a Gaussian and a top-hat, the change in refractive index is strongly explained by the difference in average optical path length experienced by the THz electric field in the experimental data and Fresnel model. It was also shown that a converging beam introduces a frequency dependent profile onto the complex refractive index, this profile is shaped by the beam profile of the converging beam.

The converging beam algorithm was used to determine the refractive index of a quartz sample placed in a converging beam THz spectrometer that is dependent on the THz optics of the setup. The extracted refractive index using a Gaussian beam profile suggested that the angular spectrum of plane waves was limited to a half width 0.24 radians which was within the limit of 0.32 radians determined by the parabolic mirrors.

I have also demonstrated a elegant method to determine the frequency dependent beam profile of a focused THz time domain spectrometer which has a distinct advantage in that it does not require any realignment of components in the THz time domain spectrometer. The method requires a THz time domain scan of the sample placed in the collimated and focused section of the THz beam which is possible in most THz time domain spectrometers that use the four parabolic setup. The method works by fitting the refractive index of a focused THz time domain scans using the converging beam extraction to the refractive index extracted from the collimated THz time domain scan using the plane wave extraction by changing the Gaussian half width which is modeled by the converging beam extraction. The combination of a converging beam extraction method and the determination of the beam profile at the THz focus will enable a more accurate determination of the complex refractive index for materials where a THz focus is essential.

In the case of focused THz beam experiments, the ambiguity of possible experimental errors that produce similar effects on the complex refractive index make it difficult to determine the behaviour of the THz beam through changes in the complex refractive index alone. Therefore to progress the research of a converging beam extraction algorithm it is required that more experiments should be performed that include the characterisation of the THz beam profile [110, 111, 113, 118] in addition to performing scans where the sample is placed in the collimated and converging sections of the THz beam. Furthermore, other effects that occur on the THz beam profile which have been unaccounted for could also produce changes on the complex refractive index which are indistinguishable to those which have been described in this chapter which further advocates for beam profiling. These effects include the initial frequency dependent THz pattern produced from the silicon lens [119], frequency dependent diffraction effects which are produced from finite size THz optics and aberrations such as astigmatism and coma.

The theory from the model of the converging beam suggests that the difference between a change in complex refractive index between the plane wave and converging beam assumption is independent of sample thickness for samples with the same complex refractive index. This is because the change is dependent on the angular spectrum of the converging beam which will be the same for any thickness. Consider the propagation of a ray through a sample at an angle for different sample thicknesses, the ratio of the propagation lengths and hence angle for the off and on axis rays will be the same for any thickness. Future experiments to test if thicker samples experience a stronger effect of the converging beam would be to investigate samples with the same complex refractive index and different thicknesses in focused THz spectrometer.

Chapter 5

VECSEL pumped THz Time Domain Spectrometer

5.1 Introduction

In THz-TDS the Titanium Sapphire laser is the traditional pump laser for THz generation and detection because it is capable of ultrashort pulses with high average output power and direct bandgap excitation of LT-GaAs. However it is also bulky and expensive which limits the potential for a compact and cheap THz spectrometer. There are a number of cheaper and compact pump solutions such as solid state and fiber lasers which lase at 1 μm and so there has been interest into 1 μm THz generation and detection [46, 120, 121, 49]. Another alternative 1 μm pump laser are modelocked vertical external cavity surface emitting lasers (ML-VECSEL) which are compact, have multi-GHz repetition rates and could lead to a cost effective integrated THz spectrometer system.

VECSELs are optically pumped semiconductor disk lasers (SDL) that were first demonstrated by M. Kuznetsov et. al. [122] in 1997 which have since been mode-locked [123] using SEmiconductor Saturable Absorbing Mirrors (SESAM). In 2008 at the University of Southampton, Z. Mihoubi et. al. [124] demonstrated the first all-semiconductor room-temperature terahertz time domain spectrometer which produced THz radiation over the range 0.1 - 0.8 THz, pumped using a VECSEL. Recent developments in the VECSEL group at the University of Southampton have led to VECSELs with higher peak powers [125] than previously available which are more suitable for THz generation and detection. The work I am reporting here is the THz-TDS spectrometer performance from a VECSEL which at present, produces the highest peak powers that are available from a VECSEL within the VECSEL group at the University of Southampton.

In this chapter I begin by discussing VECSEL developments and the current VECSEL performance which are beneficial for VECSEL pumped THz-TDS systems and describe the theory of basic VECSEL operation and design. I then demonstrate VECSEL performance and the THz performance when it is used to pump a THz-TDS spectrometer. Finally I make comparisons of THz performance with the VECSEL, a Spectra-Physics Tsunami (Titanium Sapphire) laser at 800 nm and a High-Q-laser femtoTRAIN (Ytterbium glass solid state) laser at 1035 nm.

5.2 Introduction to VECSELs

5.2.1 VECSEL developments

VECSELs are optically pumped semiconductor disk lasers (SDL) that were first demonstrated by M. Kuznetsov et. al. [122] in 1997 using CW operation. In 2000 the first passively mode-locked VECSEL was demonstrated [123] using a SEmiconductor Saturable Absorbing Mirrors (SESAM) producing picosecond pulses at 1030 nm. In 2002 A. Garnache et. al. [126] reported on a sub-500 fs SESAM mode-locked VECSEL at 1040 nm utilising the optical Stark effect (OSE). Since that time the continuous development in the design and fabrication of the VECSEL has led to shorter pulses [127] with increasing average output power, at present the shortest pulse duration demonstrated is 60 fs [128] with an average output power of 35 mW. The combination of femtosecond pulses with hundreds of milliwatt average output powers has led to high peak power VECSELs, in 2010 K. G. Wilcox et. al. [125] demonstrated a VECSEL with 335 fs and peak pulse power of 315 W and recently in 2012 M. Scheller et. al. [129] demonstrated a VECSEL with 682 fs pulses and a peak pulse power of 3850 W. VECSELs with high peak power and femtosecond pulses are essential for a THz-TDS pump laser, the typical peak power of a pulse incident on a THz PCA from a Titanium Sapphire laser is above 1000 W.

VECSELs are multi-GHz repetition rate lasers due to the inherently short upper level life time of the semiconductor gain material. Although the higher repetition rates lead to lower peak powers which can be detrimental for THz generation and detection, the higher repetition rates also increase the sampling rate of the THz electric field which has been shown [130, 103] to improve the SNR of THz-TDS scans. Statistically the noise level of a THz scan will be proportional to its standard deviation which varies with the square of the number of samples, whereas the signal varies linearly with the number of samples. Recently repetition rates of 92 GHz [131] and 169 GHz [132] have been demonstrated using harmonic modelocking, also there have been demonstrations of tunable GHz repetition rate VECSELs [133, 134]. Tunable GHz repetition rate VECSELs will enable us to study the direct impact of sampling rate on the SNR of THz scans and enable high-speed asynchronous optical THz-TDS sampling (ASOPS) [135, 120].

One drawback of the ultrafast high peak power VECSELs described above is their operating wavelengths are above or near 1000 nm which is larger than 870 nm the bandgap wavelength of LT-GaAs PCA, THz generation is possible from below bandgap transitions caused by defect states, however, this generally produces a smaller THz signal than above bandgap generation [44]. LT-InGaAs PCA has a bandgap dependent on the indium concentration, which can be grown for 1000 nm excitation [46] however these antenna are more prone to electrical failure than the LT-GaAs. Alternatively an 832 nm passively mode-locked VECSEL [136] producing 15.3 ps pulses has been demonstrated, the pulse duration is too long for THz generation but developments to reduce the pulse duration of such a VECSEL would allow for above bandgap THz generation in LT-GaAs.

5.2.2 VECSEL basics

A double folded Z-cavity ML-VECSEL is shown in fig. 5.1, the laser cavity is formed between the output coupler, gain chip, turning mirror and SESAM. The gain chip and SESAM are grown onto a substrate using molecular beam epitaxy (MBE) or metal organic chemical vapour deposition (MOCVD). The gain chip contains an active gain region and is pumped using a fibre coupled diode laser. The quantum defect between the pump photon energy and bandgap of the active gain region produces heating within the gain chip due to non-radiative recombination. A heat sink with water cooling and a Peltier cooler is used to thermally manage the gain chip temperature. The substrate is typically 500 μm thick whereas the active gain region is less than a micron. The presence of the substrate limits the thermal impedance of the gain chip and the ability for the heat sink to extract heat from the active region as was the case for the VECSEL demonstrated in this chapter. VECSELs are however power scalable [137] due to the small active gain region which allows for efficient one dimensional heat flow provided the substrate is removed.

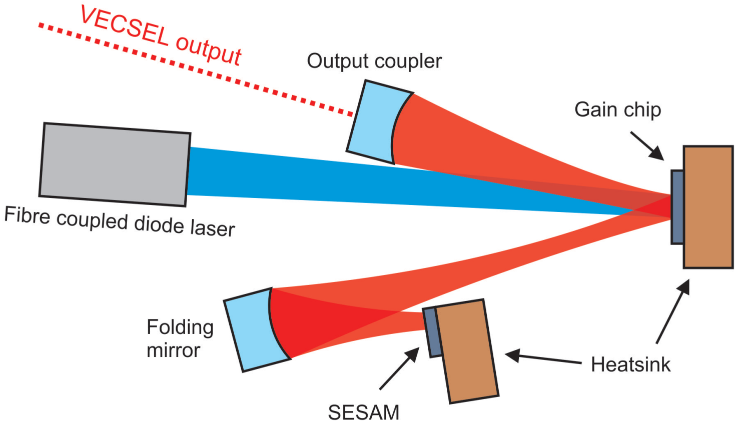

Figure 5.1: Z-cavity configuration of a VECSEL.

A schematic for a gain chip is shown in fig. 5.2, it contains distributed Bragg reflector (DBR), quantum wells (QWs) which create the active gain region, a spacer layer and capping layer. The schematic shows the design for gain chip V629 which was grown at the University of Cambridge using MBE from layers of the III-V group of semiconductors, AlAs, GaAs and InGaAs. The semiconductor bandgap of the QWs determines the emission wavelength of the VECSEL, for example the QWs in V629 were grown from $In_{20\%}Ga_{80\%}As$ where the concentration level of indium was set to 20% as this gave a QW peak emission wavelength of 1000 nm for which it was designed. There are however limitations in bandgap engineering for the emission wavelength of VECSELs due to strain caused by a mismatch of the lattice constant between adjacent semiconductor layers. Strain causes structure degradation at the layer interfaces in the form of defects that propagate along the crystal planes, these can be observed as dark line defects on the gain chip surface and reduces the VECSEL performance and lifetime. In the case of the semiconductors AlAs and GaAs, the lattice constants are well matched however there is some mismatch between the InGaAs QWs and the adjacent GaAs barriers. It is possible to reduce the strain between mismatched layers by using strain compensating layers that have some intermediate lattice constant. InP can be used as strain compensating layers for the InGaAs and GaAs interfaces, this was not possible in the MBE growth of V629 because no phosphorus source was available.

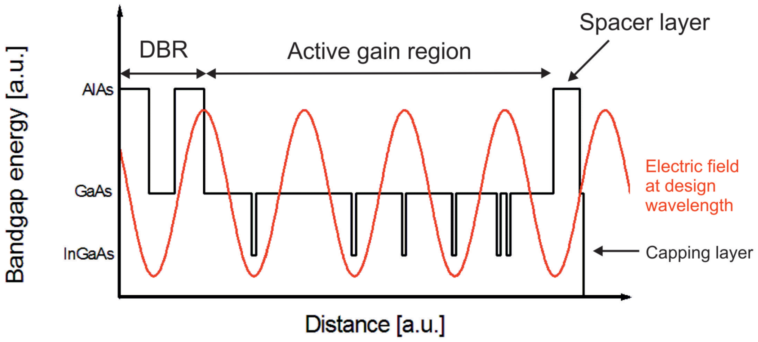

Figure 5.2: Schematic of a the VECSEL gain chip based on the gain structure V629.

A fibre coupled diode laser is used to pump the VECSEL, the majority of carrier production occurs within the bulk GaAs which sit between the QWs and produces the barriers of the QWs. This is because of the relative size of the barriers in comparison to the wells, for example in V629 the barriers are typically 130 nm thick whereas the QWs are only 8 nm thick. The carriers that are produced within the barriers diffuse to the QWs where they become confined, the carriers in the QWs interact with the electric field of the cavity mode and through stimulated emission produce more photons which allows for lasing.

The gain chip contains six QWs with specific placement within the active region, the wells are placed at the anti-nodes of the electric field standing wave which is supported by the active region microcavity and DBR. The QWs experience the greatest electric field at the anti-nodes, this maximises the coupling between the cavity photons and carriers in the QWs. The pump radiation absorption decays exponentially through the material which is why the number of wells differ at different anti-nodes, the anti-node at the start of the gain region contains two QWs to benefit from the greater absorption. The anti-nodes at the end of the gain region have a displaced QW to account for the lower absorption. The gain region is only $7/2\lambda$ in thickness where λ is the VECSEL design wavelength within the gain chip as this allows for six anti-nodes to fit the QWs in, for V629 this gives a gain region thickness of approximately 1 μm. The VECSEL design V629 has low gain due to the small gain region and antiresonant design which requires a low loss cavity to lase.

Increasing the number of QWs within the gain region does increase gain, but there are limitations due to the additional loss that each unpumped QW introduces above the inherent cavity loss. To reach lasing threshold the gain must be equal to the loss, and so more QWs require more carriers to reach threshold. Generating more carriers means pumping harder but this increases the active gain region temperature at threshold due to the limited heat removal. The increased temperature at threshold reduces the operating range of the VECSEL between threshold and thermal rollover.

The DBR is a series of high and low refractive indexed layers which are a quarter of a wavelength thick so that the reflected light at each interface constructively interferes enhancing the total reflectivity of the DBR. The DBR in V629 is made from 27.5 pairs of AlAs and GaAs layers. The spacer layer determines the resonance of the gain chip, anti-resonant designs have a node near the surface whereas resonant designs have an anti-node near the surface. Resonant designs have a much larger electric field inside the sample than anti-resonant designs and therefore more gain, however resonant designs have less gain bandwidth than anti-resonant designs due to gain filtering which make them less favourable for mode-locking. The capping layer is there to protect the previous AlAs layer from oxidisation.

5.2.3 The SESAM and modelocking

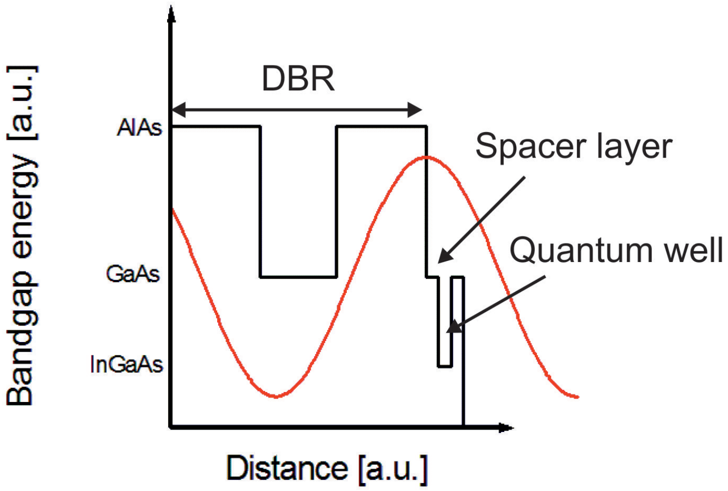

Figure 5.3: Schematic of a the SESAM based on the structure V628.

The schematic for the SESAM is shown in fig. 5.3, it contains a DBR and a single QW which is used to introduce a saturable loss mechanism within the cavity and produce passive modelocking. Mode-locking is the locking the cavity modes that exist within the laser with a phase relationship such that there is pulse formation. Photons within the cavity are absorbed by the SESAM until the SESAM is saturated causing the reflectivity of the SESAM to increase and the cavity loss to decrease. This produces a window of net gain in which a pulse can form, the SESAM recovers and process repeats.

There are two main types of saturable absorber regimes which I shall briefly describe as these determine the pulse shaping mechanism and ultimately pulse duration. These regimes are dependent on the relative saturation and recovery times of the SESAM and VECSEL gain. In the fast saturable absorber regime [138] the recovery time of the gain is shorter than the pulse duration, therefore the pulse is shaped by the time dependent saturation and recovery of the SESAM. In the slow saturable absorber regime [139] the recovery time of the gain is longer than the pulse duration, when the SESAM is saturated the gain also saturates. In this case the SESAM saturation shapes the front end of the pulse and the saturation of the gain shapes the tail end of the pulse.

The percentage change between saturated and unsaturated loss from the SESAM is called the modulation depth, a larger modulation depth will lead to stronger modelocking and shorter pulses provided there is gain. However for low gain lasers such as the VECSEL, a relatively low modulation depth, between 0.3% and 0.7% is needed. This is achieved by using a single QW, located near the electric field maximum at the surface of the DBR. The design, which does not contain a microcavity to enhance the modulation depth, has relatively low dispersion. The QW location, near the surface of the SESAM also enables a faster recovery time of the QW due to surface recombination states.

Femtosecond pulses can be generated in VECSELs using the optical Stark effect (OSE) as a fast saturable absorber mechanism [126, 140, 141]. The OSE produces a blue shift in the SESAM absorption due to the intense electric field of the optical pulse, if the electric field is on the long side of the SESAM absorption then the blue shift will reduce the absorption and hence loss of the optical pulse. The OSE is a near-instantaneous and intensity dependent effect, in the time domain the wings at the front and back end of the pulse do not experience the Stark shift because they have the lowest intensity. Therefore the wings experience more loss than the peak of the pulse, after each pass of the SESAM the wings become consecutively expunged from the main pulse shortening the pulse duration.

5.3 VECSEL pumped THz spectrometer

5.3.1 Preliminary performance

The VECSEL was constructed using the gain chip V629 and SESAM V628 in a 1 GHz Z-cavity configuration which was then coupled to a THz spectrometer. V629 and V628 were designed by Dr. Keith G. Wilcox with a design wavelength of 1 μm and were grown at the University of Cambridge using MBE. The VECSEL performance of V629 and V628 has previously been demonstrated by Wilcox [125], it produced 335 fs pulses with an average output power of 120 mW and a peak power of 315 W.

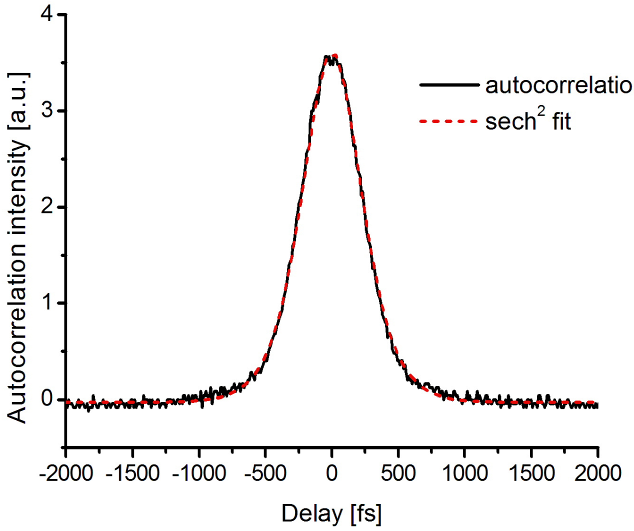

Figure 5.4: Autocorrelation of the VECSEL, the sech^2 FWHM of the pulse duration is 350 fs.

A schematic of the Z-cavity is shown in fig 5.1, a 50 mm focal length output coupler with 0.7% transmission was used at a distance of 50 mm from the gain chip. A folding mirror with focal length of 38 mm was used to focus the cavity mode onto the SESAM. The distance between the gain chip and folding mirror was 65 mm and the distance between the SESAM and folding mirror was 25 mm. The VECSEL was pumped using an 830 nm fibre coupled diode laser which was driven by an SDL 820 laser diode driver. The SESAM and gain chip were both mounted onto heat sinks with water cooling and temperature control. The centre wavelength of the QW absorption in the SESAM is temperature dependent, hence the SESAM temperature affects the strength of mode-locking and pulse duration.

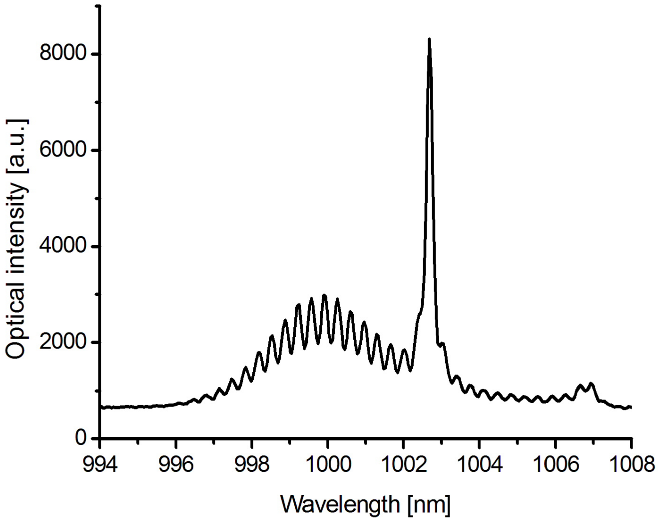

Figure 5.5: Optical spectrum of VECSEL. The optical spectrum contains etalon modulations and a CW component.

I successfully mode-locked the VECSEL with 350 fs pulses as shown by FWHM sech^2 fit on the autocorrelation in fig. 5.4. The VECSEL was pumped with 1.25 W and gave an output power of 30 mW, the spectrum is shown in fig. 5.5. The central wavelength of the spectrum is 1 μm and contains a CW component at 1003 nm, also modulations of the spectrum are present which is due to a secondary etalon produced from substrate reflections of either the gain or SESAM. It was not possible to use a sech^2 fit to determine the spectral width due to the CW component and modulations, however the approximate FWHM is 3.3 nm which gives 1.1 transform limited pulses. The VECSEL cavity supports both CW and modelocking laser operation. The CW component is an indication that some spectral components of the laser are not modelocked and is indicative of modelocking instability. The initial operation of the VECSEL is CW until the cavity is modelocked through optimisation of the VECSEL, optimisation takes into account, cavity alignment, SESAM temperature, gain temperature and incident pump power. If the modelocking is not stable then the VECSEL moves back into CW operation, initially this can be seen from the CW component on the spectrum as observed. The effect of the secondary etalon also produced multiple pulses within the laser cavity, this was observed intermittently on the autocorrelation as shown in fig. 5.6 by the smaller satellite pulses.

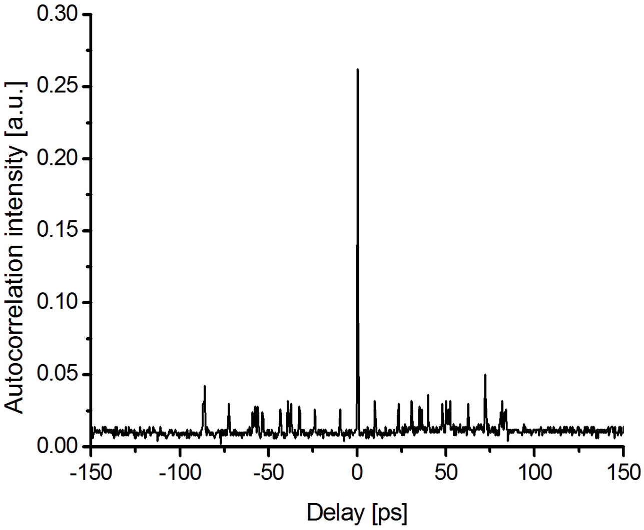

Figure 5.6: Autocorrelation showing multiple pulsing from the VECSEL.

The amount of multiple pulsing that occurred was dependent on the peak power of the main pulse, hence the SESAM temperature had a dominant effect. The temperature range explored for the SESAM was between 10°C and 40°C. At temperatures below 10°C the VECSEL stopped modelocking because the central resonance of the SESAM was so far from the VECSEL design wavelength that the modulation of depth of the SESAM was compromised. SESAM temperatures above 40°C significantly reduced the output power of the VECSEL. The SESAM temperature was at 40°C when the lowest pulse duration of 350 fs was observed with an output power of 30 mW. As the temperature of the SESAM was decreased to 10°C and the 350 fs pulse duration maintained, the output power increased but there was a significant increase in the multiple pulsing. When operating the SESAM at 10°C the multiple pulsing could be reduced by decreasing the SESAM fluence which also increased the pulse duration to 400 fs.

The behaviour of the multiple pulsing appears dependent on some threshold of peak power, as the VECSEL configuration tends towards single pulsed operation there is a reduction in either pulse duration or internal cavity power in order to keep the peak power below the multiple pulsing threshold. At the lower SESAM temperatures where the output power is greater it is far easier to exceed this threshold when producing 350 fs, at the higher temperatures it is easier to reduce the multiple pulsing but at the expense of output power.

To obtain the maximum THz signal the maximum peak power from the VECSEL is required to pump the THz spectrometer, multiple pulsing prevents this because it distributes cavity power away from the main pulse. In the fast saturable absorber regime VECSELs are susceptible to multiple pulsing because the upper state life time of the carriers in the gain is so small that the gain recovers before the main pulse returns. Therefore gain is always available which makes it possible for noise spikes to induce a second pulse within the cavity. Etalon effects within the cavity can reinforce this effect by producing periodic noise spikes which originate from the main pulse being reflected from the substrate. Removing the modulations present in the optical spectrum through careful alignment could possibly remove the multiple pulses, another solution is to angle polish the back of the gain chip or SESAM substrate so that the reflections do not couple back into the cavity.

Modelocking stability of the VECSEL was also an issue, the longest stability period achieved was 60 - 90 seconds. This stability period would limit the length of the THz scans possible because in the transition from stable to unstable modelocking there was a degradation of the output power and pulse duration until modelocking ceased. It's difficult to determine the origin of the modelocking instability, it could be due to a contribution of effects such as pump diode fluctuations, the multiple pulsing or thermal effects on the SESAM. A characteristic of the VECSEL which suggested that thermal effects on the SESAM were a source of modelocking instability was that after the VECSEL experienced modelocking instability the modelocking stability could be improved by repositioning where the laser cavity mode was incident on the SESAM.

A schematic of the THz spectrometer pumped by the VECSEL is shown in fig. 5.7. The aim was to measure some preliminary performance of the THz spectrometer and to then make further optimisations on the VECSEL and spectrometer. The spectrometer used two 50.8 mm diameter parabolic mirrors with focal lengths 50.8 mm to collimate and focus the THz beam, the optical delay was a motorised delay stage with a maximum delay of 140 ps. The emitter and receiver were LT-GaAs bow-tie antenna with a 6 μm gap, each with Si hyperhemispherical lenses mounted on top. Microscope objectives were used to focus the pump and probe beams

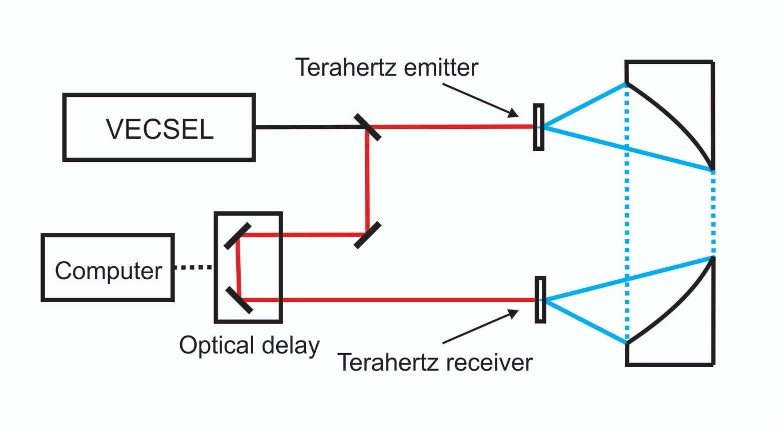

Figure 5.7: Schematic of the THz spectrometer that was pumped using a VECSEL.

onto the PCA. The initial alignment of the THz spectrometer was performed using a High-Q-laser femtoTRAIN (Ytterbium glass solid state) laser at 1035nm with a 140 fs pulse duration, the beam alignment was recorded using pin hole apertures which the VECSEL was then aligned to. The bias across the emitter was 10 V peak to peak which was frequency modulated at 24.9 kHz using a square wave. The femtoTRAIN laser produced a maximum output power of 270 mW of which 18 mW were incident on the emitter and 5 mW were incident on the receiver, this produced a photocurrent of 2 nA from the THz spectrometer. The average output power from the VECSEL was limited to 30 mW of which 15 mW were incident on the emitter and 1.5 mW incident on the receiver. The VECSEL produced a photocurrent of 100 pA from the THz spectrometer, the power on the receiver was a limiting factor on the THz photocurrent and it was difficult to maximise the incident power on the receiver due to the low output power from the VECSEL. Alignment and optimisation of the VECSEL to the THz spectrometer was a difficult task due to the modelocking instability and the lower power of the VECSEL, it was difficult to determine which gains in THz signal were due to optimisations in alignment of the VECSEL to the spectrometer and fluctuations in VECSEL stability.

The THz time domain scan using the VECSEL is shown in fig. 5.8, due to the stability of the VECSEL a scan of 250 data points which took 75 seconds to record was taken which gave a scan length of 33.2 ps. The amplitude of the THz pulse is 140 pA, the spectrum of the scan is shown in fig. 5.9. The bandwidth of the spectrum was 1.0 THz and with a dynamic range was 15 dB, in comparison the femtoTRAIN laser produced a bandwidth of 1.4 THz with a dynamic

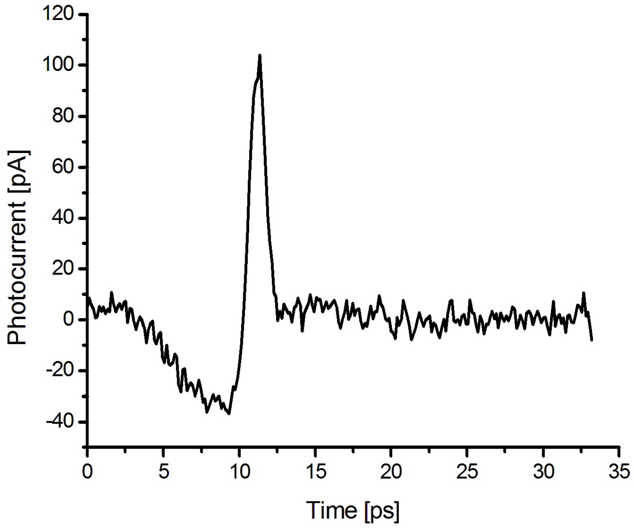

Figure 5.8: THz scan for the VECSEL pumped THz-TDS setup.

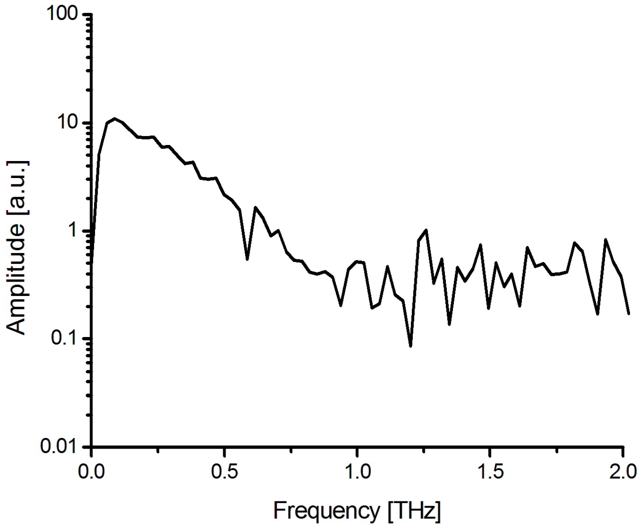

Figure 5.9: THz spectrum for the VECSEL pumped THz-TDS setup.

range of 34 dB. The initial results are comparable to the 0.1 - 0.8 THz of bandwidth reported by Z. Mihoubi [124] which used a 480 fs VECSEL, in my work the VECSEL performance was limited in modelocking instability which reduced scan length and multiple pulsing which reduced peak pulse power. Several other attempts were made to improve on this result using different alignment of the SESAM, during which the maximum photocurrent observed was 400 pA. The VECSEL was unable to sustain the conditions required for the 400 pA photocurrent, therefore further optimisations of the VECSEL and THz spectrometer were made which are discussed below.

5.3.2 Further optimisations

Several optimisations were made to THz spectrometer to improve the THz signal. The receiver was changed from a LT-GaAs 6 micron bow-tie antenna to a LT-InGaAs 5 micron gap bow-tie antenna, LT-InGaAs has a lower bandgap than LT-GaAs which is advantageous for 1 micron excitation because this enables more carrier generation and therefore a larger photocurrents. The LT-GaAs emitter was not changed to LT-InGaAs because THz generation requires a bias voltage which reduces the life time of the antenna and LT-GaAs is more robust than LT-InGaAs due to its higher electrical breakdown field. The microscope objective lenses used to focus the pump and probe beam onto the antenna were changed to anti-reflection coated aspheric lenses. The aspheric lenses enabled better transmission of the laser beams due to the anti-reflection coating and better mechanical alignment for focusing the beam onto the antenna.

Optimisations were also made to the VECSEL to increase modelocking stability and reduce multiple pulsing. A compartment was built around the VECSEL to minimise the air flow within the cavity mode to improve stability. A different part of the sample wafers V629 and V628 were used and the back of the SESAM substrate was angle polished to reduce multiple pulsing.

The optimisations to the VECSEL did not completely remove the multiple pulses but were successful in reducing them, the VECSEL modelocking stability increased to 150 seconds which allowed for double the scan length of 68 ps. The pump power was increased from 1.25 W to 1.37 W and the gain chip heat sink temperature was reduced from -20°C to -33°C. The VECSEL now gave enough output power to pump the emitter with 45 mW and the receiver with 12 mW, however the pulse duration increased to 390 fs which is shown in fig. 5.10 by the sech^2 fit. The corresponding spectrum is shown on fig. 5.11, the spectrum still shows modulations indicative of

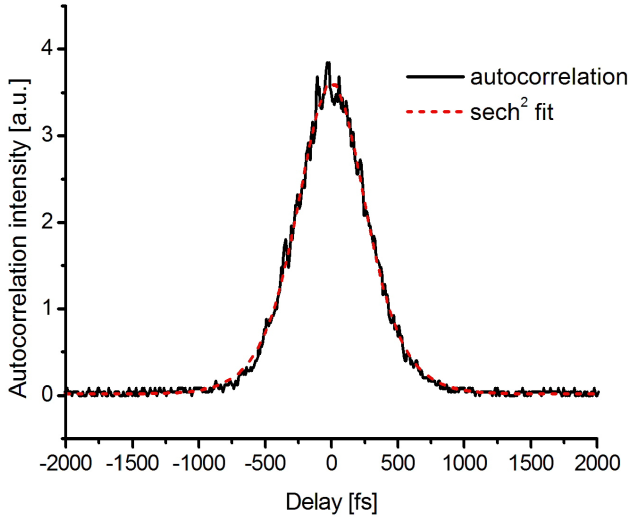

Figure 5.10: Autocorrelation of the VECSEL, the sech^2 FWHM of the pulse duration is 390 fs.

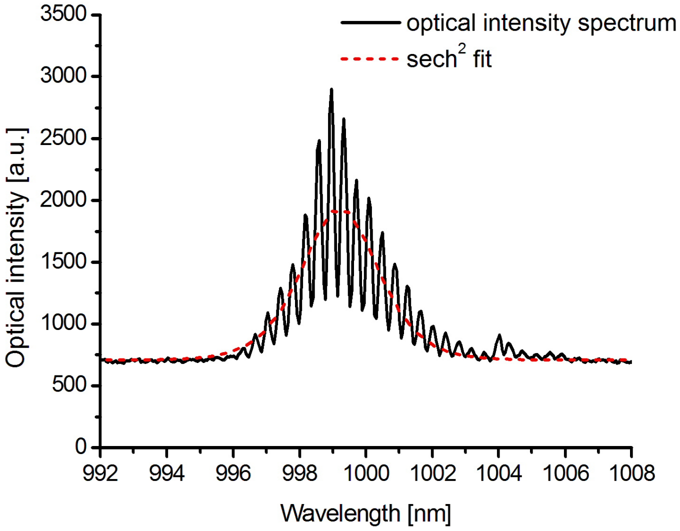

Figure 5.11: Optical spectrum of VECSEL with a sech^2 FWHM spectral width of 1.35 nm.

an internal cavity etalon and a reduction in the CW component in comparison to the preliminary spectrum in fig. 5.5. The spectral width was 2.7 nm which gives the transform limit for 390 fs sech^2 pulses. The bias voltage on the emitter was increased to 12 V with a modulation frequency of 31.5 kHz. The THz scan obtained using the VECSEL is shown in fig. 5.12 and the THz spectrum is shown in fig. 5.13. Despite the greater incident pump power on the antenna the photocurrent was only 30 pA which gave a THz bandwidth of 0.5 THz and dynamic range of 13 dB, however the longer scan time did improve the resolution of the THz spectrum. The THz performance was lower than the preliminary scan, the reason is due to the weaker focusing from aspheric lenses which limited the fluence incident on the antenna. Changing the aspheric lenses back to the microscope objectives was not possible due to time constraints.

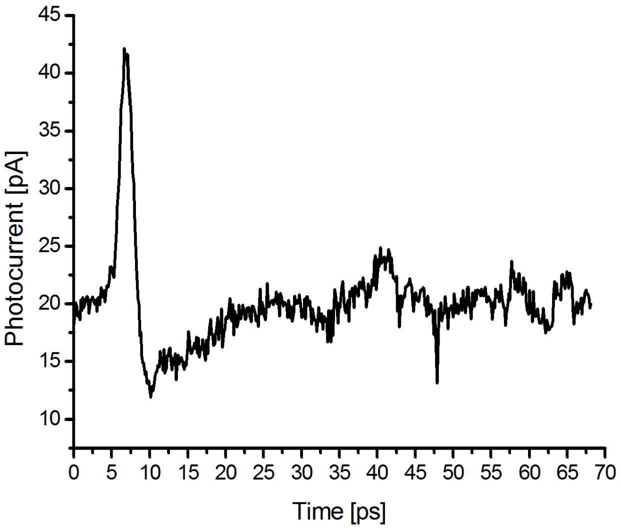

Figure 5.12: THz scan for the VECSEL pumped THz-TDS setup.

5.4 Comparison with other lasers

A High-Q-laser femtoTRAIN (Ytterbium glass solid state) and Spectra-Physics Tsunami (Titanium Sapphire) laser systems were also used to pump the THz-TDS setup with different incident pump powers so that comparisons with the VECSEL THz spectrometer performance could be made.

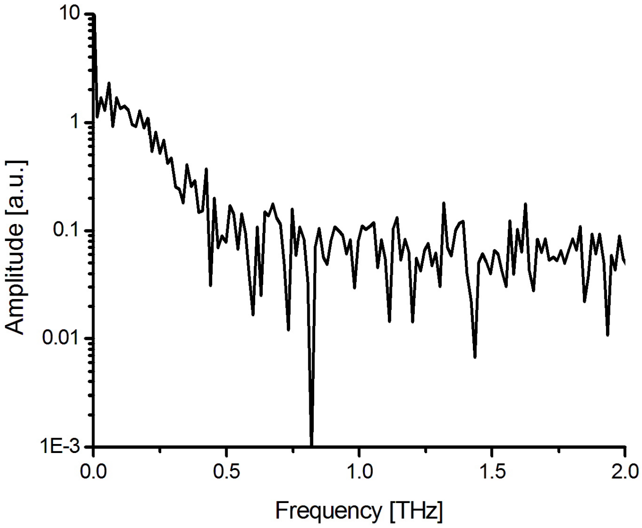

Figure 5.13: THz spectrum for the VECSEL pumped THz-TDS setup.

The femtoTRAIN operated with a central wavelength of 1035 nm and repetition rate of 64.43 MHz. The sech^2 FWHM pulse duration of the femtoTRAIN laser measured at the output coupler is approximately 140 fs, the pulse duration measured before the antenna objectives was 220 fs. Dispersion from the optical elements within the setup had broadened the pulse. The photon of the energy of the femtoTRAIN laser is 1.20 eV which is similar to VECSEL photon energy of 1.24 eV. Both the femtoTRAIN laser and VECSEL photon energies are below 1.42 eV the bandgap of the LT-GaAs emitter, the mechanism for carrier generation in the antenna and hence THz generation is indirect excitation of carriers through defect sites which occur due to the low temperature growth [44].

The output from the femtoTRAIN laser was also compressed using a photonic crystal fibre and dispersion compensation elements. The pulse durations produced at the output of the compressor were dependent on incident pump intensity and were between 30 and 70 fs. The autocorrelations of these compressed pulses displayed wings which suggested not all of the power was being coupled into the main pulse. The pulse duration of the compressed pulses measured before the antenna objectives increased to 90 and 130 fs due to dispersion, the autocorrelations also displayed more modulations.

The Tsunami laser operated with a central wavelength of 800 nm and repetition rate of 80 MHz. The pulse duration measured at the output was 50 fs and the pulse duration measured before the antenna objective was 100 fs. The Tsunami produced Gaussian shaped pulses and spectra. The Tsunami photon energy is 1.55 eV which is above the bandgap of the antenna, this allows for direct production of electron hole pairs within the antenna.

5.4.1 Laser spot size, fluence and peak intensity

The relative fluence incident on the emitter due to each laser was determined by measuring average power and the beam width just before the antenna. A knife edge was used to measure the intensity profile near the antenna, a Gaussian profile was then fit to the differential of the intensity profile to determine the beam width. The spot size incident on the antenna was calculated by assuming a diffraction limited spot size in the Fraunhofer regime using,

$$d = 2.44\lambda\frac{f}{2\omega} \tag{5.1}$$

where d is the spot size, λ is the wavelength, f is the focal length of the lens ($f = 4.5mm$) and ω is the beam width. The measured beam widths from the knife edge intensity profile and estimated spot sizes are shown in table 5.1. The estimated spot size of the VECSEL is not only the largest but is close to the antenna gap size of the emitter (6 μm) and larger than the receiver (5 μm). This limited the performance of the antenna and hence the THz spectrometer performance due to reduced current density.

Laser system	Beam width [mm]	Spot size [μm]
Tsunami	1.1	4.0
femtoTRAIN	2.8	3.2
femtoTRAIN compressed	1.3	4.4
VECSEL	1.0	5.5

Table 5.1: Beam widths of each laser and the relative spot size on the emitter.

The fluence incident on the antenna was calculated using,

$$F = \frac{P_{avg}}{\nu\pi d^2} \tag{5.2}$$

and the peak intensity incident on the antenna for a laser generating sech^2 pulses was calculated using,

$$I_{peak} = 0.88 \times \frac{P_{avg}}{\nu \tau \pi d^2} \tag{5.3}$$

where P_{avg} is the average power on the antenna, ν is the repetition rate, τ is the FWHM of the pulse duration and d is the spot size.

5.4.2 Results

For each laser the power incident on the receiver was set to 9 mW and the power incident on the emitter varied between 2 - 16 mW, the bias on the emitter was modulated at a frequency of 31.5 kHz with 8 V peak to peak. Each of the scans were taken with 512 data points except the Tsunami which was taken with 1024 data points. The THz time domain scans are shown in fig. 5.14 where 16 mW was incident on the emitter. The Tsunami laser produced a photocurrent amplitude of 9 nA whereas the femtoTRAIN laser produced 2 nA of photocurrent, the preliminary VECSEL results had a photocurrent of 110 pA and would not be visible on this scale. Interestingly, the compressed femtoTRAIN scans have a lower amplitude than the uncompressed scans, this is due to either the different spot sizes which lead to different fluences on the antenna or the pulse shape of the compressed pulse.

Fig. 5.15 shows the peak to peak amplitude of the THz pulse from the VECSEL, Tsunami, femtoTRAIN and compressed femtoTRAIN laser systems versus the fluence incident on the emitter. The Tsunami amplitudes are greater than the femtoTRAIN amplitudes due to the above bandgap excitation. The below bandgap amplitudes of the femtoTRAIN laser show a linear trend dependent on the incident fluence which is independent of pulse duration, this could be because the THz spectrometer bandwidth is limited by the 500 fs [43] carrier life time of the LT-InGaAs receiver. The VECSEL amplitude is also consistent with the femtoTRAIN results.

Fig. 5.16 shows the peak to peak amplitude of the THz pulse from the VECSEL, Tsunami, femtoTRAIN and compressed femtoTRAIN laser systems versus the peak intensity incident on the emitter. The peak intensity does take into account of the pulse duration, in comparison to fig. 5.16 there is no apparent trends with below band gap excitations except that as peak intensity increases so does photocurrent amplitude.

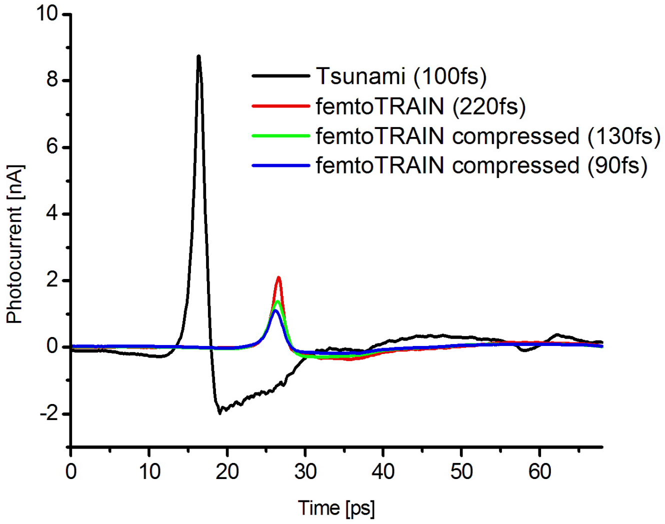

Figure 5.14: THz time domain scans using the Tsunami, femtoTRAIN and compressed femtoTRAIN laser.

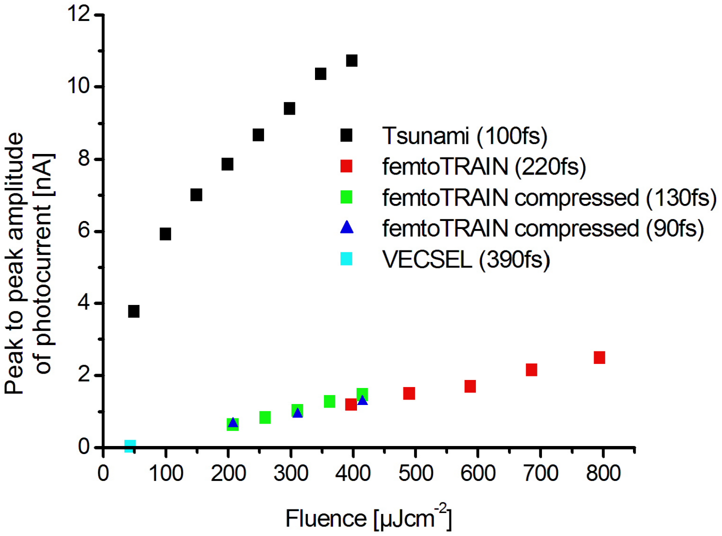

Figure 5.15: The peak to peak amplitude of the THz pulse from the VECSEL, Tsunami, femtoTRAIN and compressed femtoTRAIN laser systems versus fluence incident on the emitter.

Fig. 5.17 shows the THz spectrum of each scan including the previous VECSEL spectra, it shows the Tsunami with greatest amplitude however the noise floor is also much greater in comparison to the femtoTRAIN spectra. The uncompressed femtoTRAIN spectra shows greater bandwidth than the compressed femtoTRAIN spectra, this could due to the combination of greater fluence on the antenna and cleaner pulse shape.

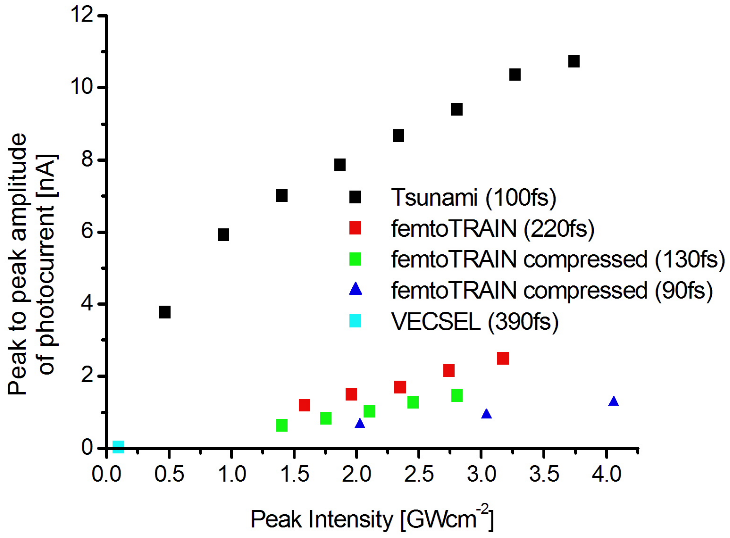

Figure 5.16: The peak to peak amplitude of the THz signal from various laser systems with different peak intensities incident on the photoconductive emitter.

Laser system	Bandwidth [THz]	Dynamic range [dB]
Tsunami (100fs)	1.5	25
femtoTRAIN (220fs)	1.4	34
femtoTRAIN compressed (130fs)	1.1	33
femtoTRAIN compressed (90fs)	1.1	32
VECSEL (390fs)	0.5	13
preliminary VECSEL (350fs)	0.9	15

Table 5.2: Beam widths of each laser and the relative spot size on the emitter.

Table 5.2 shows the different bandwidths and dynamic ranges calculated for each scan, the

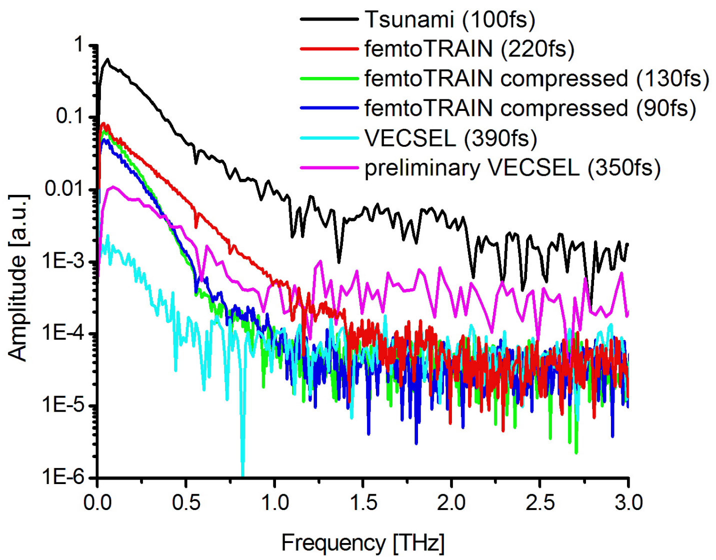

Figure 5.17: The peak to peak amplitude of the THz signal from various laser systems with different peak intensities incident on the photoconductive emitter.

table shows that the femtoTRAIN spectra have greater dynamic range than the Tsunami spectra. The bandwidth of the Tsunami spectra is limited to 1.5 THz due to the high noise floor which is reflected by the low dynamic range. On the other hand the bandwidth of the femtoTRAIN spectra are limited by the low photocurrent due to the below bandgap excitation, however the below bandgap excitation has produced spectra with less noise and more dynamic range. The preliminary VECSEL scan reaches 0.9 THz despite having only 15 dB of dynamic range and comparison between above and below bandgap excitation has highlighted the potential performance that an optimised VECSEL pumped THz spectrometer will have, particularly if the antenna response is not limited by pulse duration.

5.5 Conclusion

I studied a THz-TDS spectrometer using a mode-locked a 1 μm VECSEL with 1.1 transform limited 350 fs sech^2 pulses. The VECSEL pumped THz spectrometer produced a THz bandwidth of 1.0 THz which is similar to performance demonstrated [124] using 500 fs VECSEL. The THz bandwidth was limited due to the multiple pulsing within the VECSEL cavity which reduced the individual pulse peak power and the limited VECSEL output power which did not allow for optimum power incident on the THz antenna.

Optimisations were made to the increase the VECSEL output power which enabled sufficient incident power the THz antenna and the THz receiver was changed to LT-InGaAs which has a closer bandgap to 1 μm than the LT-GaAs receiver. The back of the SESAM substrate was angle polished to remove stray reflections which could contribute to the multiple pulsing. Improvement in the THz performance from these optimisations were not realised due to the limited fluence on the THz antenna from the replacement focusing optics. Comparisons made with a 1035 μm Ytterbium glass solid state and 800 nm Titanium Sapphire laser show that below bandgap excitation of photoconductive antenna based THz spectrometers produce THz spectra with less noise and more dynamic range than above bandgap excitation. This results in comparable THz bandwidth between the two forms of excitation which highlights the potential performance that an optimised VECSEL pumped THz spectrometer can achieve.

Further work is required to optimise the VECSEL-THz setup to achieve results similar to the Ytterbium glass solid state laser which include optimising the fluence incident on the THz antenna and investigating VECSEL instability which has a series of effects on the VECSEL. These include multiple pulsing, degradation of output power and pulse duration with time, these effects are dependent on the amount of time the VECSEL cavity mode is incident on one particular SESAM position. The assumption is these instabilities arise from some type of non-saturable loss due to a heating process a which occurs within the SESAM, the process is not fully understood but is being investigated by the VECSEL group at the University of Southampton. Provided that these limitations can be overcome future work would be to build a tunable repetition rate VECSEL [133, 134] to measure the direct impact of sampling rate on the SNR [130, 103] of THz scans.

Chapter 6

Conclusions

6.1 Material parameter extraction

The work presented in this thesis is mainly aimed at developing a material parameter extraction method to accurately determine the optical constants of materials using THz-TDS. I have demonstrated the principles of material parameter extraction from which an extraction algorithm was produced. The extraction method used the Fresnel model to determine the propagation of a plane wave THz electric field through a single layered homogeneous material at normal incidence with no scattering loss. The theoretical transfer function was constructed from the Fresnel model and an equivalent experimental transfer function from the THz time domain scans. The Newton-Raphson method was used to fit the model to the experimental data, I demonstrated that it is important to use phase unwrapping so that the theoretical transfer function is at to the correct phase which ensures that the correct refractive index and extinction coefficient are extracted.

I have demonstrated various techniques which optimised the theoretical transfer function for material parameter extraction, which include finding the optimum length parameter required to reduce the Fresnel oscillations present on the complex refractive index. I also extracted the complex refractive index for different numbers of reflections in the theoretical transfer function compared with the experimental data. From the comparison it was concluded that as long as the number of reflections in the theoretical transfer function is equal to or larger than the number of reflections in the experimental data then the theoretical transfer function will be sufficient for the extraction. Extraction with the infinite reflection transfer function is the optimum transfer function for THz time domain scans that includes one or more reflections and the zero reflection transfer function is the optimum transfer function if no reflections are present.

I demonstrated a noise suppression algorithm which was applied to experimental data, it revealed spectral features where the SNR is low which would otherwise be hidden using standard material parameter extraction methods which effectively increased the useful bandwidth of the THz-TDS system. The noise suppression algorithm modelled random spectrometer noise, to improve this technique optimisation of the noise model is required. To optimise the noise model noise characterisation experiments for the THz spectrometer are needed.

I also approximated the theoretical transfer function to analytically determine how deficiencies in the transfer function with experimental data change the complex refractive index. The deficiencies investigated were the time offset between sample data and reference data, incorrect phase extrapolation to zero frequency, gain changes between sample and reference, incorrect sampling interval specified, incorrect sample thickness, sample misorienation with respect to the terahertz beam and sampling interval different in sample and reference data. The principle changes observed on the complex refractive index from these deficiencies was a shift or amplitude oscillations in either refractive index or extinction coefficient. The combination of these deficiencies are difficult to distinguish from each other. The inclusion of the material parameter extraction optimisation techniques to the plane wave extraction method allow for plane wave material parameter extraction methods which are similar to the state of the art in the field.

Samples placed at the THz focus are commonly investigated using the plane wave assumption for material parameter extraction. I have demonstrated a converging beam material parameter extraction method, which uses an arbitrary frequency dependent angular profile and takes into account an arbitrary number of internal reflections. Two different angular beam profiles were used, a Gaussian and a top-hat, the change in refractive index is strongly explained by the difference in average optical path length experienced by the THz electric field in the experimental data and Fresnel model. It was shown that a converging beam introduces a frequency dependent profile onto the complex refractive index, this profile is shaped by the beam profile of the converging beam. The converging beam algorithm was used to determine the refractive index of a quartz sample placed in a converging beam THz spectrometer that is dependent on the THz optics of the setup. The extracted refractive index using a Gaussian beam profile suggested that the angular spectrum of plane waves was limited to a half width 0.24 radians which was within the limit of 0.32 radians determined by the parabolic mirrors.

I have also demonstrated a elegant method to determine the frequency dependent beam profile of a focused THz time domain spectrometer which does not require any realignment of components in the THz time domain spectrometer. The method can be used in any THz time domain spectrometers that use the four parabolic setup and has access to the collimated and focused sections of the THz beam. The method requires a THz time domain scan of the sample placed in the collimated and focused section of the THz beam. The method works by fitting the refractive index of a focused THz time domain scans using the converging beam extraction to the refractive index extracted from the collimated THz time domain scan using the plane wave extraction by changing the Gaussian half width which is modeled by the converging beam extraction. The combination of a converging beam extraction method and the determination of the beam profile at the THz focus will enable a more accurate determination of the complex refractive index for materials where a THz focus is essential. Since, I can simulate a system which is closer to experiment by taking into account converging beam of arbitrary angular profiles and also, samples at an angle, in theory my algorithms have an advantage in relation to the state of the art in the field.

In the case of focused THz beam experiments, the ambiguity of possible experimental errors that produce similar effects on the complex refractive index make it difficult to determine the behaviour of the THz beam through changes in the complex refractive index alone. Therefore to progress the research of a converging beam extraction algorithm it is required that more experiments should be performed that include the characterisation of the THz beam profile [110, 111, 113, 118] in addition to performing scans where the sample is placed in the collimated and converging sections of the THz beam. Furthermore, other effects that occur on the THz beam profile which have been unaccounted for could also produce changes on the complex refractive index which are indistinguishable to those which have been described in this chapter which further advocates for beam profiling. These effects include the initial frequency dependent THz pattern produced from the silicon lens [119], frequency dependent diffraction effects which are produced from finite size THz optics and aberrations such as astigmatism and coma.

6.2 VECSEL pumped THz-time domain spectrometer

I successfully investigated a THz-TDS spectrometer using a mode-locked 1 μm VECSEL with 1.1 transform limited 350 fs sech^2 pulses. The VECSEL pumped THz spectrometer produced a THz bandwidth of 1.0 THz which is similar to performance demonstrated [124] using 500 fs VECSEL. The THz bandwidth was limited due to the multiple pulsing within the VECSEL cavity which reduced the individual pulse peak power and the limited VECSEL output power which did not allow for optimum power incident on the THz antenna.

Optimisations were made to increase the VECSEL output power which enabled sufficient incident power the THz antenna and the THz receiver was changed to LT-InGaAs which has a closer bandgap to 1 μm than the LT-GaAs receiver. The back of the SESAM substrate was angle polished to remove stray reflections which could contribute to the multiple pulsing. Improvement in the THz performance from these optimisations were not realised due to the limited fluence on the THz antenna from the replacement focusing optics. Comparisons made with a 1035 μm Ytterbium glass solid state and 800 nm Titanium Sapphire laser show that below bandgap excitation of photoconductive antenna based THz spectrometers produce THz spectra with less noise and more dynamic range than above bandgap excitation. This results in comparable THz bandwidth between the two forms of excitation which highlights the potential performance that an optimised VECSEL pumped THz spectrometer can achieve particularly if the optical pulse duration does not limit the response of the antenna.

Further work is required to optimise the VECSEL-THz setup to achieve results similar to the Ytterbium glass solid state laser which include optimising the fluence incident on the THz antenna and investigating VECSEL instability which has a series of effects on the VECSEL. These include multiple pulsing and degradation of output power and pulse duration with time, these effects are dependent on the amount of time the VECSEL cavity mode is incident on one particular SESAM position. The assumption is these instabilities arise from some type of non-saturable loss due to a heating process which occurs within the SESAM, the process is not fully understood but is being investigated by the VECSEL group at the University of Southampton. Future work would be to build tunable repetition rate VECSEL [133, 134] to measure the direct impact of sampling rate on the SNR [130] of THz scans.

Appendix A

Conference and journal publications produced during this thesis

A. L. Chung, Z. Mihoubi, G. J. Daniell, A. H. Quarterman, K. G. Wilcox, H. E. Beere, D. A. Ritchie, A. C. Tropper, V. Apostolopoulos. Material parameter extraction in THz-TDS using a converging beam transfer function. *In 35th International Conference on Infrared, Millimeter and Terahertz Waves*, 2010.

A. H. Quarterman, K. G. Wilcox, A. Perevedentsev, V. Apostolopoulos, Z. Mihoubi, A. L. Chung, H. E. Beere, I. Farrer, D. A. Ritchie, A. C. Tropper. 169 GHz repetition rate passively harmonically mode-locked VECSEL emitting 265 fs pulses. *Proc. of SPIE*, 7919, 2011.

D. McBryde, M. E. Barnes, G. J. Daniell, A. L. Chung, Z. Mihoubi, A. H. Quarterman, K. G. Wilcox, A. C. Tropper, and V. Apostolopoulos. Simulation of metallic nanostructures for emission of THz radiation using the lateral photo-Dember effect. *In 36th International Conference on Infrared, Millimeter and Terahertz Waves*, 2011.

M. E. Barnes, D. McBryde, G. J. Daniell, G. Whitworth, A. L. Chung, A. H. Quarterman, K. G. Wilcox, A. Brewer, H. E. Beere, D. A. Ritchie, and V. Apostolopoulos. Terahertz emission by diffusion of carriers and metal-mask dipole inhibition of radiation. *Optics Express*, 20(8):8898-8906, 2012.

Bibliography

[1] J. C. Wiltse. History of Millimeter and Submillimeter Waves. *Microwave Theory and Techniques, IEEE Transactions on*, 32(9):1118–1127, 1984.

[2] T. G. Phillips and J. Keene. Submillimeter Astronomy. *Proceedings of the IEEE*, 80(11):1662–1678, 1992.

[3] B. Carli, F. Mencaraglia, and A. Bonetti. Submillimeter high-resolution FT spectrometer for atmospheric studies. *Applied Optics*, 23(15):2594–2603, 1984.

[4] Y. Yang, A. Shutler, and D. R. Grischkowsky. Measurement of the transmission of the atmosphere from 0.2 to 2 THz. *Optics Express*, 19(9):8830–8838, 2011.

[5] W. Aenchbacher, M. Naftaly, and R. Dudley. Line strengths and self-broadening of pure rotational lines of nitrous oxide measured by terahertz time-domain spectroscopy. *J. Opt. Soc. Am. B*, 27(9):1717–1721, 2010.

[6] N. Nagai, R. Kumazawa, and R. Fukasawa. Direct evidence of inter-molecular vibrations by THz spectroscopy. *Chemical Physics Letters*, 413(4-6):495500, 2005.

[7] B. Ferguson and X.-C. Zhang. Materials for terahertz science and technology. *Nature Materials*, 1:26–33, 2002.

[8] P. H. Siegel. Terahertz Technology. *Microwave Theory and Techniques, IEEE Transactions on*, 50(3):910–928, 2002.

[9] M. Tonouchi. Cutting-edge terahertz technology. *Nature Photonics*, 1:97–105, 2007.

[10] G. P. Williams. Filling the THz gap - high power sources and applications. *Reports on Progress in Physics*, 69(2):301–326, 2006.

[11] D. H. Auston, K. P. Cheung, and P. R. Smith. Picosecond photoconducting Hertzian dipoles. *Applied Physics Letters*, 45(3):284–286, 1984.

[12] P. R. Smith, D. H. Auston, and M. C. Nuss. Subpicosecond photoconducting dipole antennas. *Quantum Electronics, IEEE Journal of*, 24(2):255–260, 1988.

[13] S. Kono, M. Tani, P. Gu, and K. Sakai. Detection of up to 20 THz with a low-temperature-grown GaAs photoconductive antenna gated with 15 fs light pulses. *Applied Physics Letters*, 77(25):4104–4106, 2000.

[14] H. Shimosato, M. Ashida, T. Itoh, S. Saito, and K. Sakai. Ultrabroadband Detection of Terahertz Radiation from 0.1 to 100 THz with Photoconductive Antenna. *Springer Series in Optical Sciences*, 132:317–323, 2007.

[15] J. B. Baxter and C. A. Schmuttenmaer. Conductivity of ZnO Nanowires, Nanoparticles, and Thin Films Using Time-Resolved Terahertz Spectroscopy. *J. Phys. Chem. B*, 110(50):25229–25239, 2006.

[16] J. T. Kindt and C. A. Schmuttenmaer. Theory for determination of the low-frequency time-dependent response function in liquids using time-resolved terahertz pulse spectroscopy. *J. Chem. Phys.*, 110(17):8589–8596, 1999.

[17] M. C. Beard, G. M. Turner, and C. A. Schmuttenmaer*. Theory for determination of the low-frequency time-dependent response function in liquids using time-resolved terahertz pulse spectroscopy. *J. Phys. Chem. B*, 106(29):7146–7159, 2002.

[18] Q.-L. Zhou, Y. Shi, T. Li, B. Jin, D. Zhao and C. Zhang. Carrier dynamics and terahertz photoconductivity of doped silicon measured by femtosecond pump-terahertz probe spectroscopy. *Sci China Ser G-Phys Mech Astron*, 52(12):1944–1948, 2009.

[19] Q.-L. Zhou, Y. Shi, B. Jin, and C. Zhang. Ultrafast carrier dynamics and terahertz conductivity of photoexcited GaAs under electric field. *Applied Physics Letters*, 93(10):102103, 2008.

[20] S. Funk, G. Acuna, M. Handloser, and R. Kersting. Probing the momentum relaxation time of charge carriers in ultrathin layers with terahertz radiation. *Optics Express*, 17(20):17450–17456, 2009.

[21] H. P. Porte, P. U. Jepsen, N. Daghestani, E. U. Rafailov, and D. Turchinovich. Ultrafast release and capture of carriers in InGaAs/GaAs quantum dots observed by time-resolved terahertz spectroscopy. *Applied Physics Letters*, 94(26):262104, 2009.

[22] A. D. Jameson, J. L. Tomaino, YS. Lee, J. P. Prineas, J. T. Steiner, M. Kira, and S. W. Koch. Transient optical response of quantum well excitons to intense narrowband terahertz pulses. *Applied Physics Letters*, 95(20):201107, 2009.

[23] M. C. Beard , G. M. Turner , and C. A. Schmuttenmaer. Size-Dependent Photoconductivity in CdSe Nanoparticles as Measured by Time-Resolved Terahertz Spectroscopy. *Nano Letters*, 2(9):983–987, 2002.

[24] S. J. Kim, B. Born, M. Havenith, and M. Gruebelel. Real-Time Detection of Protein-Water Dynamics upon Protein Folding by Terahertz Absorption Spectroscopy. *Angewandte Chemie International Edition*, 47(34):6486–6489, 2008.

[25] T. Nagashima, J. Nishitani, and K. Kozuki. Electron spin response studied by THz time domain spectroscopy. *In 2009 Conference on Lasers and Electro-Optics and The Pacific Rim Conference on Lasers and Electro-Optics*, 2009.

[26] B. B. Hu and M. C. Nuss. Imaging with terahertz waves. *OPTICS LETTERS*, 20(16):1716–1718, 1995.

[27] W. L. Chan, J. Deibel and D. M. Mittleman. Imaging with terahertz radiation. *Reports on Progress in Physics*, 70(8):1325–1379, 2007.

[28] B. Fischer, M. Hoffmann, H. Helm, G. Modjesch, and P. U. Jepsen. Chemical recognition in terahertz time-domain spectroscopy and imaging. *Semiconductor Science and Technology*, 20(7):s246–s253, 2005.

[29] L. Hoa, R. Müllerd, K. C. Gordon, P. Kleinebudde, M. Pepper, T. Rades, Y. Shen, P. F. Taday, J. A. Zeitler. Terahertz pulsed imaging as an analytical tool for sustained-release tablet film coating. *European Journal of Pharmaceutics and Biopharmaceutics*, 71(1):117–123, 2009.

[30] R. M. Woodward, V. P. Wallace, D. D. Arnone, E. H. Linfield, and M. Pepper. Terahertz Pulsed Imaging of Skin Cancer in the Time and Frequency Domain. *Journal of Biological Physics*, 29(2-3):257–259, 2003.

[31] J. F. Federici, B. Schulkin, F. Huang, D. Gary, R. Barat, F. Oliveira, and D. Zimdars. THz imaging and sensing for security applicationsexplosives, weapons and drugs. *Semiconductor Science and Technology*, 20(7):s266–s280, 2005.

[32] X.-C. Zhang, Y. Jin, and X. F. Ma. Coherent measurement of THz optical rectification from electro-optic crystals. *Applied Physics Letters*, 61(23):2764–2766, 1992.

[33] L. Xu, X.-C. Zhang, and D. H. Auston. Terahertz beam generation by femtosecond optical pulses in electro-optic materials. *Applied Physics Letters*, 61(15):1784–1786, 1992.

[34] Y. C. Shen, P. C. Upadhya, E. H. Linfield, H. E. Beere, and A. G. Davies. Ultrabroadband terahertz radiation from low-temperature-grown GaAs photoconductive emitters. *Applied Physics Letters*, 83(15):3117–3119, 2003.

[35] S. Kono, M. Tani and K. Sakai. Coherent detection of mid-infrared radiation up to 60 THz with an LT-GaAs photoconductive antenna. *Optoelectronics, IEE Proceedings*, 149(3):105–109, 2002.

[36] S. Kono, M. Tani, and K. Sakai. Ultrabroadband photoconductive detection: Comparison with free-space electro-optic sampling. *Applied Physics Letters*, 79(7):898–900, 2001.

[37] K. Sakai. *Terahertz Optoelectronics*, chapter 1, page 9. Springer, 2005.

[38] L. Duvillaret, F. Garet, J.-F. Roux, and J.-L. Coutaz. Analytical Modeling and Optimization of Terahertz Time-Domain Spectroscopy Experiments Using Photoswitches as Antennas. *Selected Topics in Quantum Electronics, IEEE Journal of*, 7(4):615–623, 2001.

[39] M. C. Beard, G. M. Turner, and C. A. Schmuttenmaer. Subpicosecond carrier dynamics in low-temperature grown GaAs as measured by time-resolved terahertz spectroscopy. *Journal of Applied Physics*, 90(12):5915–5923, 2001.

[40] X. Liu, A. Prasad, W. M. Chen, A. Kurpiewski, A. Stoschek, Z. Liliental-Weber, and E. R. Weber. Mechanism responsible for the semi-insulating properties of low-temperature-grown GaAs. *Applied Physics Letters*, 65(23):3002–3004, 1994.

[41] M. C. Beard, G. M. Turner, and C. A. Schmuttenmaer. Transient photoconductivity in GaAs as measured by time-resolved terahertz spectroscopy. *Physical Review B*, 62(23):1576415777, 2000.

[42] X. Zheng, Y. Xu, R. Sobolewski, R. Adam, M. Mikulics, M. Siegel, and P. Kordoš. Femtosecond response of a free-standing LT-GaAs photoconductive switch. *Applied Optics*, 42(9):1726–1731, 2003.

[43] C. Baker, I. S. Gregory, W. R. Tribe, I. V. Bradley, M. J. Evans, E. H. Linfield, and M. Missous. Highly resistive annealed low-temperature-grown InGaAs with sub-500 fs carrier lifetimes. *Applied Physics Letters*, 85(21):4965–4967, 2004.

[44] S. U. Dankowski, D. Streb, M. Ruff, P. Kiesel, M. Kneissl, B. Knüpfer, G. H. Döhler, U. D. Keil, C. B. Sørenson, and A. K. Verma. Above band gap absorption spectra of the arsenic antisite defect in low temperature grown GaAs and AlGaAs. *Applied Physics Letters*, 68(1):37–39, 1996.

[45] M. Tani, K.-S. Lee, and X.-C. Zhang. Detection of terahertz radiation with low-temperature-grown GaAs-based photoconductive antenna using 1.55 μm probe. *Applied Physics Letters*, 77(9):1396–1398, 2000.

[46] C. Baker, I. S. Gregory, W. R. Tribe, I. V. Bradley, M. J. Evans, M. Withers, P. F. Taday, V. P. Wallace, E. H. Linfield, A. G. Davies, and M. Missous. Terahertz pulsed imaging with 1.06 μm laser excitation. *Applied Physics Letters*, 83(20):4113–4115, 2003.

[47] M. E. Barnes, D. McBryde, G. J. Daniell, G. Whitworth, A. L. Chung, A. H. Quarterman, K. G. Wilcox, A. Brewer, H. E. Beere, D. A. Ritchie, and V. Apostolopoulos. Terahertz emission by diffusion of carriers and metal-mask dipole inhibition of radiation. *Optics Express*, 20(8):8898–8906, 2012.

[48] G. Klatt, F. Hilser, W. Qiao, M. Beck, R. Gebs, A. Bartels, K. Huska, U. Lemmer, G. Bastian, M. B. Johnston, M. Fischer, J. Faist, and T. Dekorsy. Terahertz emission from lateral photo-Dember currents. *Optics Express*, 18(5):4939–4947, 2010.

[49] G. Klatt, B. Surrer, D. Stephan, O. Schubert, M. Fischer, J. Faist, A. Leitenstorfer, R. Huber, and T. Dekorsy. Photo-Dember terahertz emitter excited with an Er:fiber laser. *Applied Physics Letters*, 98(2):021114, 2011.

[50] D. McBryde, M. E. Barnes, G. J. Daniell, A. L. Chung, Z. Mihoubi, A. H. Quarterman, K. G. Wilcox, A. C. Tropper, and V. Apostolopoulos. Simulation of metallic nanostructures for emission of THz radiation using the lateral photo-Dember effect. *In 36th International Conference on Infrared, Millimeter and Terahertz Waves*, 2011.

[51] S. L. Dexheimer. *Terahertz Spectroscopy: Principles and Applications*, chapter 2, pages 44–48. CRC Press, 2007.

[52] A. Manabe, A. Mitsuishi, and H. Yoshinaga. Infrared Lattice Reflection Spectra of II-VI Compounds. *Japanese Journal of Applied Physics*, 6(5):593–600, 1967.

[53] P. U. Jepsen, R. Jacobsen, and S. Keiding. Generation and detection of terahertz pulses from biased semiconductor antennas. *J. Opt. Soc. Am. B*, 13(11):2424–2436, 1996.

[54] S. E. Ralph and D. R. Grischkowsky. Trap-enhanced electric field in semi-insulators: The role of electrical and optical carrier injection. *Applied Physics Letters*, 59(16):1972–1974, 1991.

[55] M. Tani, S. Matsuura, K. Sakai and S. Nakashima. Emission characteristics of photoconductive antennas based on low-temperature-grown GaAs and semi-insulating GaAs. *Applied Optics*, 36(30):7853–7859, 1997.

[56] P. Maraghechi and A. Y. Elezzabi. Enhanced THz radiation emission from plasmonic complementary Sierpinski fractal emitters. *Optics Express*, 18(26):27336–27345, 2010.

[57] J. M. Diao, F. Yang, Z. P. Nie, J. Ouyang, and P. Yang. Separated Fractal Antennas For Improved Emission Performance Of Terahertz Radiations. *Journal of Electromagnetic Waves and Applications*, 26(8-9):1158–1167, 2012.

[58] R. Singh, C. Rockstuhl, C. Menzel, T. P. Meyrath, M. He, H. Giessen, F. Lederer, and W. Zhang. Spiral-type terahertz antennas and the manifestation of the Mushiake principle. *Optics Express*, 17(12):9971–9980, 2009.

[59] C. Kübler, R. Huber, S. Tübel, and A. Leitenstorfer. Ultrabroadband detection of multi-terahertz field transients with GaSe electro-optic sensors: Approaching the near infrared. *Applied Physics Letters*, 85(16):3360, 2004.

[60] G. Scalari, C. Walther, M. Fischer, R. Terazzi, H. Beere, D. Ritchie, and J. Faist. THz and sub-THz quantum cascade lasers. *Laser and Photonics Reviews*, 3(1-2):4566, 2009.

[61] B. S. Williams, S. Kumar, H. Callebaut, Q. Hu, and J. L. Reno. Terahertz quantum-cascade laser at $\lambda \approx 100$ μm using metal waveguide for mode confinement. *Applied Physics Letters*, 83(11), 2003.

[62] Q. Y. Lu, N. Bandyopadhyay, S. Slivken, Y. Bai, and M. Razeghi. Room temperature single-mode terahertz sources based on intracavity difference-frequency generation in quantum cascade lasers. *Applied Physics Letters*, 99(13):131106, 2011.

[63] J. Zhang, H. Deng, X. Lin, D. Dai, Q. Sun, S. Lu, T. Yu, H. Zhao, H. Yang, and Z. Dai. Tunable few-cycle coherent terahertz radiation with watt-level power from relativistic femtosecond electron beam. *Nuclear Instruments and Methods in Physics Research A*, 693:2325, 2012.

[64] G. L. Carr, M. C. Martin, W. R. McKinney, K. Jordan, G. R. Neil, and G. P. Williams. High-power terahertz radiation from relativistic electrons. *Nature*, 420(6912):153–156, 2002.

[65] M. Y. Glyavin, A. G. Luchinin, and G. Y. Golubiatnikov. Generation of 1.5-kW, 1-THz Coherent Radiation from a Gyrotron with a Pulsed Magnetic Field. *Physical Review Letters*, 100(1):015101, 2008.

[66] F. Amira, C. Mitchella, N. Farringtonb, and M. Missousa. Advanced Gunn diode as high power terahertz source for a millimetre wave high power multiplier. *Proc. of SPIE*, 7485:74850I, 2009.

[67] W. Knap, M. Dyakonov, D. Coquillat, F. Teppe, N. Dyakonova, J. usakowski, K. Karpierz, M. Sakowicz, G. Valusis, D. Seliuta, I. Kasalynas, A. El Fatimy, Y. Meziani, and T. Otsuji. Field Effect Transistors for Terahertz Detection: Physics and First Imaging Applications. *Journal of Infrared, Millimeter and Terahertz waves*, 30(12):1319–1337, 2012.

[68] T. Watanabe, K. Akagawa, Y. Tanimoto, D. Coquillat, W. Knap, and T. Otsuji. Terahertz Imaging with InP High-electron-mobility Transistors. *Proc. of SPIE*, 8023:80230, 2010.

[69] L. Vicarelli, M. S. Vitiello, D. Coquillat, A. Lombardo, A. C. Ferrari, W. Knap, M. Polini, V. Pellegrini, and A. Tredicucci. Graphene field effect transistors as room-temperature Terahertz detectors. *Nature Materials*, 11(10):865–871, 2012.

[70] R. Kaneko, I. Kawayama, H. Murakami, and M. Tonouchi. Detection of Pulsed Terahertz Waves Using High-Temperature Superconductor Josephson Junction. *Applied Physics Express*, 3(4):042701, 2010.

[71] A. Irie, D. Oikawa, and G. Oya. Generation and detection of THz radiation using intrinsic Josephson junctions. *Physics Procedia*, 36:199204, 2012.

[72] A. D. Semenov, H. Richter, H.-W. Hübers, B. Günther, A. Smirnov, K. S. Ilin, M. Siegel, and J. P. Karamarkovic. Terahertz Performance of Integrated Lens Antennas With a Hot-Electron Bolometer. *Microwave Theory and Techniques, IEEE Transactions on*, 55(2):239–247, 2007.

[73] J. Yang, S. Ruan, M. Zhang, and W. Zhang. Real-time continuous-wave imaging with a 1.63THz OPTL and a pyroelectric camera. *Optoelectronics Letters*, 4(4):295–298, 2008.

[74] E. Öjefors, A. Lisauskas, D. Glaab, H. G. Roskos, and U. R. Pfeiffer. Terahertz Imaging Detectors in CMOS Technology. *Journal of Infrared, Millimeter, and Terahertz Waves*, 30(12):1269–1280, 2009.

[75] B. N. Behnken, G. Karunasiri, D. R. Chamberlin, P. R. Robrish, and J. Faist. Real-time imaging using a 2.8 THz quantum cascade laser and uncooled infrared microbolometer camera. *Optics Letters*, 33(5):440–442, 2008.

[76] F. Huang, B. Schulkin, H. Altan, J. F. Federici, D. Gary, R. Barat, D. Zimdars, M. Chen, and D. B. Tanner. Terahertz study of 1,3,5-trinitro-s-triazine by time-domain and Fourier transform infrared spectroscopy. *Applied Physics Letters*, 85(23):55355537, 2004.

[77] L. Duvillaret, F. Garet, and J.-L. Coutaz. A Reliable Method for Extraction of Material Parameters in Terahertz Time-Domain Spectroscopy. *Selected Topics in Quantum Electronics, IEEE Journal of*, 2(3):739–746, 1996.

[78] M. Naftaly and R. E. Miles. Terahertz time-domain spectroscopy: A new tool for the study of glasses in the far infrared. *Journal of Non-Crystalline Solids*, 351(40-42):3341–3346, 2005.

[79] D. R. Grischkowsky, S. Keiding, M. van Exter, and Ch. Fattinger. Far-infrared time-domain spectroscopy with terahertz beams of dielectrics and semiconductors. *J. Opt. Soc. Am. B*, 7(10):20062015, 1990.

[80] G. Ma, D. Li, H. Ma, J. Shen, C. Wu, J. Ge, S. Hu, and N. Dai. Carrier concentration dependence of terahertz transmission on conducting ZnO films. *Applied Physics Letters*, 93(21):211101, 2008.

[81] N. Vieweg, C. Jansen, M. K. Shakfa, M. Scheller, N. Krumbholz, R. Wilk, M. Mikulics, and M. Koch. Molecular properties of liquid crystals in the terahertz frequency range. *Optics Express*, 18(6):6097–6107, 2010.

[82] J. T. Kindt and C. A. Schmuttenmaer. Far-Infrared Dielectric Properties of Polar Liquids Probed by Femtosecond Terahertz Pulse Spectroscopy. *J. Phys. Chem.*, 100(24):10373–10379, 1996.

[83] X. Lia, Z. Hong, J. He, and Y. Chen. Precisely optical material parameter determination by time domain waveform rebuilding with THz time-domain spectroscopy. *Optics Communications*, 283(23):4701–4706, 2010.

[84] I. Pupeza, R. Wilk, and M. Koch. Highly accurate optical material parameter determination with THz time-domain spectroscopy. *Optics Express*, 15(7):4335–4350, 2007.

[85] T. D. Dorney, R. G. Baraniuk, and D. M. Mittleman. Material parameter estimation with terahertz time-domain spectroscopy. *J. Opt. Soc. Am. A*, 18(7):1562–1571, 2001.

[86] E. Hecht. *Optics*, chapter 4, pages 114–115. Addison Wesley, 2002.

[87] R. Wilk, I. Pupeza, R. Cernat, and M. Koch. Highly Accurate THz Time-Domain Spectroscopy of Multilayer Structures. *Selected Topics in Quantum Electronics, IEEE Journal of*, 14(2):392–398, 2008.

[88] M. Scheller, C. Jansen, and M. Koch. Analyzing sub-100-μm samples with transmission terahertz time domain spectroscopy. *Optics Communications*, 282(7):13041306, 2009.

[89] D. Zhou, E. P. J. Parrott, D. J. Paul, and J. A. Zeitler. Determination of complex refractive index of thin metal films from terahertz time-domain spectroscopy. *J. Appl. Phys.*, 104(5):053110, 2008.

[90] M. Krüger, S. Funkner, E. Bründermann, and M. Havenith. Uncertainty and Ambiguity in Terahertz Parameter Extraction and Data Analysis. *Journal of Infrared, Millimeter and Terahertz Waves*, 32(5):699–715, 2010.

[91] W. Withayachumnankul, B. M. Fischer, H. Lin, and D. Abbott. Uncertainty in terahertz time-domain spectroscopy measurement. *J. Opt. Soc. Am. B*, 25(6):1059–1072, 2008.

[92] M. Kaushik, B. W.-H. Ng, B. M. Fischer, and D. Abbott. Terahertz scattering by granular composite materials: An effective medium theory. *Applied Physics Letters*, 100(1):011107, 2012.

[93] P. Mousavi, F. Haran, D. Jez, F. Santosa, and J. S. Dodge. Simultaneous composition and thickness measurement of paper using terahertz time-domain spectroscopy. *Applied Optics*, 48(33):6541–6546, 2009.

[94] P. Silfsten, V. Kontturi, T. Ervasti, J. Ketolainen, and KE. Peiponen. KramersKronig analysis on the real refractive index of porous media in the terahertz spectral range. *Optics Letters*, 36(5):778–780, 2011.

[95] B. D. O. Anderson and J. B. Moore. *Optimal Filtering*. Dover Publications Inc., 1979.

[96] A. F. Gyles. A time-domain transfer function model of Wagner's Law: the case of the United Kingdom economy. *Applied Economics*, 23(2):327–330, 1991.

[97] R. Zhang, J. H. Zuckerman, C. A. Giller, and B. D. Levine. Transfer function analysis of dynamic cerebral autoregulation in humans. *Am. J. Physiol.*, 274(1):H233–H241, 1998.

[98] M. Naftaly, R. A. Dudley, J. R. Fletcher, F. Bernard, C. Thomson, and Z. Tian. Frequency calibration of terahertz time-domain spectrometers. *J. Opt. Soc. Am. B*, 26(7):13571362, 2009.

[99] E. Castro-Camus, J. Lloyd-Hughes, M. Fraser, H. H. Tan, C. Jagadish, and M. B. Johnston. Polarization sensitive terahertz time domain spectroscopy. *In 2006 Conference on Lasers and Electro-Optics*, 2006.

[100] L. Duvillaret, F. Garet, and J.-L. Coutaz. Highly precise determination of optical constants and sample thickness in terahertz time-domain spectroscopy. *Applied Optics*, 38(2):409415, 1999.

[101] Y. Liang, W. Fan, and B. Xue. Terahertz TDS signal de-noising using wavelet shrinkage. *Chinese Optics Letters*, 9(1):1684–1691, 2011.

[102] L. Duvillaret, F. Garet, and J.-L. Coutaz. Influence of noise on the characterization of materials by terahertz time-domain spectroscopy. *J. Opt. Soc. Am. B*, 17(3):452–461, 2000.

[103] M. van Exter and D. R. Grischkowsky. Characterization of an Optoelectronic Terahertz Beam System. *Microwave Theory and Techniques, IEEE Transactions on*, 38(11):s10504, 1990.

[104] B. Ferguson and D. Abbott. De-noising techniques for terahertz responses of biological samples. *Microelectronics Journal*, 32(12):943–953, 2001.

[105] M. Takeda, S. R. Tripathi, M. Aoki, K. Hirano, H. Ohtake, T. Hirosumi, and N. Hiromoto. Origin of intensity errors in THz-TDS measurements: Relation between beam deflection of the fs-laser and the THz-intensity fluctuations. *In 36th International Conference on Infrared, Millimeter and Terahertz Waves*, 2011.

[106] M. van Exter, Ch. Fattinger, and D. R. Grischkowsky. Terahertz time-domain spectroscopy of water vapor. *Optics Letters*, 14(20):1128–1130, 1989.

[107] A. Danylov. THz Laboratory Measurements of Atmospheric Absorption Between 6% and 52% Relative Humidity. *Submillimeter-Wave Technology Laboratory, University of Massachusetts Lowell*, 2006.

[108] P. U. Jepsen, D. G. Cooke, M. Koch. Terahertz spectroscopy and imaging - Modern techniques and applications. *Laser and Photonics Reviews*, 5(1):124–166, 2010.

[109] W. Withayachumnankul, G. M. Png, Y. Xiaoxia, S. Atakaramians, I. Jones, L. Hungyen, Y. U. Seam, J. Balakrishnan, B. W.-H. Ng, B. Ferguson, S. P. Mickan, B. M. Fischer, D. Abbott. T-ray sensing and imaging. *Proceedings of the IEEE*, 95(8):1528–1558, 2007.

[110] A. Bitzer, H. Helm, and M. Walther. Beam-profiling and wavefront-sensing of THz pulses at the focus of a substrate-lens. *Selected Topics in Quantum Electronics, IEEE Journal of*, 14(2):476–481, 2008.

[111] A. Bitzer, M. Walther, A. Kern, S. Gorenflo, and H. Helm. Examination of the spatial and temporal field distributions of single-cycle terahertz pulses at a beam focus. *Applied Physics Letters*, 90(7):071112, 2007.

[112] M. T. Reiten, S. A. Harmon, and R. A. Cheville. Terahertz beam propagation measured through three-dimensional amplitude profile determination. *J. Opt. Soc. Am. B*, 20(10):2215–2225, 2003.

[113] Z. Jiang and X.-C. Zhan. 2D measurement and spatio-temporal coupling of few-cycle THz pulses. *Optics Express*, 5(11):243–8, 1999.

[114] J. W. Bowen, G. C. Walker, S. Hadjiloucas, and E. Berry. The consequences of diffractively spreading beams in ultrafast THz spectroscopy. *Conference Digest of the 2004 Joint 29th International Conference on Infrared and Millimeter Waves and 12th International Conference on Terahertz Electronics*, pages 551–552, 2004.

[115] M. R. Stringer, M. Naftaly, N. Marakgos, R. E. Miles, E. Linfield, A. G. Davies. An investigation of beam focussing perturbations in THz spectroscopy measurements. *The Joint 30th International Conference on Infrared and Millimeter Waves and 13th International Conference on Terahertz Electronics*, pages 421–422, 2005.

[116] P. Kŭzel, H. Němec, F. Kadlec, and C. Kadlec. Gouy shift correction for highly accurate refractive index retrieval in time-domain terahertz spectroscopy. *Optics Express*, 18(15):15338–15348, 2010.

[117] J. A. Stratton. *Electromagnetic theory*, chapter 7, page 415. International series in pure and applied mathematic, McGraw-Hill, New York ; London, 1941.

[118] Y. Kitoh, M. Yamashita, T. Nagashima, and M. Hangyo. Terahertz Beam Profiler Using Optical Transmission Modulation in Silicon. *Japanese Journal of Applied Physics*, 40(10):1113–1115, 2001.

[119] J. van Rudd and D. M. Mittleman. The Influence of Substrate Lens Design in Terahertz Time-Domain Spectroscopy. *J. Opt. Soc. Am. B*, 19(2):319–329, 2002.

[120] R. Gebs, P. Klopp, G. Klatt, T. Dekorsy, U. Griebner, and A. Bartels. Time-domain terahertz spectroscopy based on asynchronous optical sampling with femtosecond semiconductor disk lasers. *Electronic Letters*, 46(1):75–77, 2010.

[121] G. Matthäus, B. Ortaç, J. Limpert, S. Nolte, R. Hohmuth, M. Voitsch, W. Richter, B. Pradarutti, and A. Tünnermann. Intracavity terahertz generation inside a high-energy ultrafast soliton fiber laser. *Applied Physics Letters*, 93(26):261105, 2008.

[122] M. Kuznetsov, F. Hakimi, R. Sprague, and A. Mooradian. High-Power (¿0.5-W CW) Diode-Pumped Vertical-External-Cavity Surface-Emitting Semiconductor Lasers with Circular TEM_{00} Beams. *Photonics Technology Letters, IEEE*, 9(8):1063–1065, 1997.

[123] S. Hoogland, S. Dhanjal, A. C. Tropper, J. S. Roberts, R. Häring, R. Paschotta, F. Morier-Genoud, and U. Keller. Passively Mode-Locked Diode-Pumped Surface-Emitting Semiconductor Laser. *Photonics Technology Letters, IEEE*, 12(9):1135–1137, 2000.

[124] Z. Mihoubi, K. G. Wilcox, S. Elsmere, A. Quarterman, R. Rungsawang, I. Farrer, H. E. Beere, D. A. Ritchie, A. C. Tropper, and V. Apostolopoulos. All-semiconductor room-temperature terahertz time domain spectrometer. *Optics Letters*, 33(18):2125–2127, 2008.

[125] K. G. Wilcox, A. H. Quarterman, H. Beere, D. A. Ritchie, and A. C. Tropper. High Peak Power Femtosecond Pulse Passively Mode-Locked Vertical-External-Cavity Surface-Emitting Laser. *Photonics Technology Letters, IEEE*, 22(14):1021–1023, 2010.

[126] P. Klopp, U. Griebner, M. Zorn, A. Klehr, A. Liero, M. Weyers, and G. Erbert. Mode-locked InGaAs-AlGaAs disk laser generating sub-200-fs pulses, pulse picking and amplification by a tapered diode amplifier. *Optics Express*, 17(13):10820–10834, 2009.

[127] A. Garnache, S. Hoogland, A. C. Tropper, I. Sagnes, G. Saint-Girons, and J. S. Roberts. Sub-500-fs soliton-like pulse in a passively mode-locked broadband surface-emitting laser with 100 mW average power. *Applied Physics Letters*, 80(21):3892–3894, 2002.

[128] A. H. Quarterman, K. G. Wilcox, V. Apostolopoulos, Z. Mihoubi, S. P. Elsmere, I. Farrer, D. A. Ritchie, and A. C. Tropper. A passively mode-locked external-cavity semiconductor laser emitting 60-fs pulses. *Nature Photonics*, 3(12):729 – 731, 2009.

[129] M. Scheller, T.-L. Wang, B. Kunert, W. Stolz, S.W. Koch, and J. V. Moloney. Passively modelocked VECSEL emitting 682 fs pulses with 5.1 W of average output power. *Electronics Letters*, 48(10):588–589, 2012.

[130] G. Mouret, W. Chen, D. Boucher, R. Bocquet, P. Mounaix, D. Théron, D. Lippens. High-power terahertz radiation from a high-repetition-rate large-aperture photoconducting antenna. *Microwave and Optical Technology Letters*, 17(1):23–27, 1998.

[131] P. Klopp, U. Griebner, M. Zorn, and M. Weyers. Pulse repetition rate up to 92 GHz or pulse duration shorter than 110 fs from a mode-locked semiconductor disk laser. *Applied Physics Letters*, 98(7):071103, 2011.

[132] A. H. Quarterman, K. G. Wilcox, A. Perevedentsev, V. Apostolopoulos, Z. Mihoubi, A. L. Chung, H. E. Beere, I. Farrer, D. A. Ritchie, A. C. Tropper. 169 GHz repetition rate passively harmonically mode-locked VECSEL emitting 265 fs pulses. *Proc. of SPIE*, 7919, 2011.

[133] O. D. Sieber, V. J. Wittwer, M. Mangold, M. Hoffmann, M. Golling, T. Südmeyer, and U. Keller. Femtosecond VECSEL with tunable multigigahertz repetition rate. *Optics Express*, 19(23):23538–23543, 2011.

[134] K. G. Wilcox. Frequency-tuneable ultrashort pulse VECSEL sources. *Proc. of SPIE*, 8242, 2012.

[135] A. Bartels, R. Cerna, C. Kistner, A. Thoma, F. Hudert, C. Janke, and T. Dekorsy. Ultrafast time-domain spectroscopy based on high-speed asynchronous optical sampling. *Review of Scientific Instruments*, 78(3):035107, 2007.

[136] K. G. Wilcox, Z. Mihoubi, S. Elsmere, A. Quarterman, H. D. Foreman, S. Hashimoto, T. Südmeyer, U. Keller and, A. C. Tropper. Passively modelocked 832 nm vertical-external-cavity surface-emitting semiconductor laser producing 15.3 ps pulses at 1.9 GHz repetition rate. *Electronics Letters*, 44(25):1469–1470, 2008.

[137] A. C. Tropper and S. Hoogland. Extended cavity surface-emitting semiconductor lasers. *Progress in Quantum Electronics*, 30(1):1–43, 2006.

[138] H. A. Haus. Theory of mode locking with a fast saturable absorber. *Journal of Applied Physics*, 46(7):3049–3058, 1975.

[139] H. A. Haus. Theory of Mode Locking with a Slow Saturable Absorber. *Quantum Electronics, IEEE Journal of*, 11(9):736–746, 1975.

[140] S. Hoogland, A. Garnache, I. Sagnes, J. S. Roberts and A. C. Tropper. 10-GHz Train of Sub-500-fs Optical Soliton-Like Pulses From a Surface-Emitting Semiconductor Laser. *Photonics Technology Letters, IEEE*, 17(2):267–269, 2005.

[141] K. G. Wilcox, Z. Mihoubi, G. J. Daniell, S. Elsmere, A. Quarterman, I. Farrer, D. A. Ritchie, and A. C. Tropper. Ultrafast optical Stark mode-locked semiconductor laser. *Optics Letters*, 33(23):2797–2799, 2008.